Check for updates

Recent progress in understanding the role of graphene oxide, TiO$_2$ and graphene oxide–TiO$_2$ nanocomposites as multidisciplinary photocatalysts in energy and environmental applications

Ayush Badoni,[a] Sahil Thakur,[a] Narayanasamy Vijayan, [iD][bc] Hendrik Christoffel Swart, [iD][d] Mikhael Bechelany, [iD][eh] Zhengsen Chen,[f] Shuhui Sun, [iD][f] Qiran Cai, [iD][g] Ying Chen [iD][g] and Jai Prakash [iD] *[a]

The rapid industrial advancement globally has led to critical energy shortages and environmental pollution, prompting researchers to develop simple and efficient solutions. Emerging 2D nanomaterials as sole photocatalysts and their heterostructures with traditional photocatalysts not only have boosted photocatalytic efficiency but also provided multifunctionality to their potential applications. The present review details the recent developments in graphene oxide (GO) nanomaterials and their heterostructures with metal oxide photocatalysts (particularly GO/TiO$_2$, which is the most studied nanocomposite photocatalyst system) for their potential multidisciplinary photocatalysis applications in the fields of energy and environment. Particularly, the focus is on understanding the role of GO as an emerging sole and multidisciplinary photocatalyst as well as its role in boosting the photocatalytic efficiency of traditional metal oxide photocatalysts. This review explores the fundamental photocatalytic mechanisms of GO and the synthesis of GO/TiO$_2$ nanocomposites, with emphasis on their multifunctional photocatalytic applications in topics of current interest, including photocatalytic H$_2$ production, CO$_2$ photoreduction, and photodegradation of nano-/micro-plastics and other pollutants of emerging concern (*i.e.*, pesticides, pharmaceutical, personal care products, and pathogens/viruses), which have rarely been reviewed in the past few years. In addition, their structural and morphological (0–3D) investigations, their surface chemistry, the stability/recyclability of their nanostructures and their potential use of direct/natural sunlight for sustainable development along with their computational aspects and toxicity towards human health and the environment have been highlighted. Finally, various challenges, in view of GO emerging as a sole promising photocatalyst and its nanocomposites, are discussed, along with their potential to provide sustainable solutions to energy shortage, clean energy and environmental pollution.

[a] Department of Chemistry, National Institute of Technology Hamirpur, Hamirpur-177005, H.P., India. E-mail: jaip@nith.ac.in
[b] CSIR – National Physical Laboratory, Dr K.S. Krishnan Marg, New Delhi – 110012, India
[c] Academy of Scientific and Innovative Research (AcSIR), Ghaziabad-201002, India
[d] Department of Physics, University of the Free State, Bloemfontein, ZA9300, South Africa
[e] Institut Européen des Membranes, IEM, UMR-5635, University Montpellier, ENSCM, CNRS, Place Eugene Bataillon, 34095 Montpellier, France
[f] Institut National de la Recherche Scientifique (INRS)-Centre Énergie Matériaux et Télécommunications, Varennes, Quebec J3X 1P7, Canada
[g] Institute for Frontier Materials, Deakin University, Waurn Ponds, Victoria 3216, Australia
[h] Functional Materials Group, Gulf University for Science and Technology, Mubarak Al-Abdullah, 32093, Kuwait

1. Introduction

Water, an indispensable natural asset, has sustained countless civilizations and still supports countless lives. Its significance lies in its role in preserving the ecological balance of Earth and the well-being of its inhabitants. Among the available water sources, 97% is saline, leaving only a precious 3% as drinkable water.[1] However, the demand for clean water is escalating owing to the burgeoning population, wasteful practices, erratic weather patterns, insufficient precipitation, and, notably, water pollution, which is increasingly causing water scarcity. Consequently, combating water pollution has become a paramount global concern. Among the myriad of pollutants, the discharge from industrial activities contains a plethora of organic

compounds, with dyes and plastics emerging as significant contaminants.[2] Dyes present in wastewater have long been a source of environmental degradation. Many manufacturing entities utilize dyes in their processes, with estimates suggesting that 10% to 15% of applied dyes are lost in effluent during the dyeing process. Annually, millions of tons of dyes are produced, with half of this volume applied in the textile sector.[3] Similarly, plastics are widely used in industry and agriculture owing to their affordability, lightweight nature, high strength, and excellent durability.[4] Plastics have considerably substituted many other materials and have become an integral part of daily life.[5] However, their durability and resistance to degradation have led to their substantial accumulation in the environment, especially in the marine ecosystem. Poor management of plastic waste and its ensuing pollution have raised concerns about its effects on wildlife, ecosystems, and human health. Microplastics (MPs), a subset of plastics, have emerged as a concerning micropollutant owing to their widespread presence in aquatic environment and the concern they pose to conventional recycling and wastewater treatment processes.[6] Hence, the degradation of dye and MP contaminants in wastewater can contribute to satisfying the clean water demand.

Concerns about energy and the environment have been addressed most attractively by photocatalysis, which converts solar light directly into chemical energy.[7,8] Photocatalysis utilizes clean solar energy to realize chemical reactions (through photogenerated electrons and holes) without generating extra carbon emissions.[9–12] Thus, it holds great promise in the future net-zero emission blueprint. To date, numerous research projects have been undertaken to limit air, water, and soil pollution by better understanding the basic principles of photocatalysis and increasing the photocatalytic efficiencies of different materials. Significant advancement has been made in the last several decades in the discovery of new semiconductor photocatalytic materials, comprehension of their underlying mechanisms, enhancement of their photocatalytic efficiencies, and identification of their possible applications. Pollutant degradation,[13] CO_2 photoreduction,[14] water splitting,[15] H_2 generation,[16] and bacterial disinfection[17] are some examples of these applications. However, although an extensive number of outstanding materials has been investigated, their performance is still far below the criteria for practical applications due to their low photocatalytic efficiency and poor stability.[18]

Regarding eco-friendliness, affordability, and good optical characteristics that can be tuned for a variety of uses, titanium dioxide (TiO_2) is one of the most significant metal oxide semiconductor photocatalysts.[19,20] In addition, it is biocompatible and less hazardous, making it suitable for interdisciplinary research uses. TiO_2 boasts a wide array of applications, ranging from its use in paint to food coloring, cosmetics, and tattoo pigments. Its reliability and unique photo-physical and photochemical characteristics render it indispensable in diverse fields, including solar energy cells,

solar fuels, and wastewater purification.[21] However, the main obstacles in the feasible application of TiO_2 in photocatalysis are its high recombination rate of photogenerated carriers and inadequate photoconversion efficiency. Thus, to decrease the recombination of carriers, it is crucial to enhance the sunlight response and photogenerated electron–hole pair separation abilities of TiO_2.[22] In this case, one of most common approaches is to use two-dimensional (2D) materials to alter the surface of TiO_2, which offers a simple method for increasing its photoactivity.

2D nanomaterials, consisting of single or a few atoms in thickness, are a novel family of materials with intriguing applications in electrical, energy storage, sensing, and catalysis. The optimized inherent features or even developing behaviors of 2D nanomaterials are attributed to their strong, extremely anisotropic quantum confinement effect and surface effect. Compared to their bulk equivalents, ultrathin 2D materials show significant advantages for photocatalysis due to their unique atomic structure.[23] Graphene oxide (GO) stands out as a remarkable candidate due to its 2D structure and remarkable properties, including exceptional thermal conductivity, superior mechanical strength, and high electron mobility. These qualities contribute to its versatility in enhancing the photocatalytic activity of semiconductor oxides.[24] Additionally, the high electron mobility of GO serves as a reservoir, mitigating electron–hole pair recombination.[25] Moreover, GO offers a large Brunauer–Emmett–Teller (BET) surface area, providing an advantageous framework for anchoring TiO_2 nanoparticles (NPs) and improving their pollutant adsorption capacity.[26] Fig. 1(a) depicts the different routes for the synthesis of GO/TiO_2 nanocomposites and their different applications in environmental remediation and clean energy production. Fig. 1(b) shows a pie chart indicating the percentage of publications related to GO/TiO_2 nanocomposites in various applications.

GO-based metal oxide nanocomposites have garnered significant attention in recent years owing to their potential in photocatalytic applications, which is highly reflected in the substantial number of publications in this field. Our recent literature survey showed that over the past 10 years, research on GO/TiO_2 photocatalysis has gradually increased, although there has been a slight decline in the last two years, as shown in Fig. 1(c). However, a tremendous amount of research focused on GO-based metal oxide photocatalysis, with GO/TiO_2 being the primary focus, followed by GO/ZnO nanocomposites, as shown in Fig. 1(d). Based on the literature on GO and TiO_2, these nanocomposite materials are efficient multifunctional nanomaterials and promising candidates for addressing energy and environmental pollution issues. Notably, publications on photodegradation are more prevalent, demonstrating the potential of nanocomposites in pollutant degradation and water treatment. Research on H_2 production has not been extensively explored in the last decade, with most studies focusing on CO_2 reduction and antibacterial applications. These high levels of interest indicate that GO/TiO_2
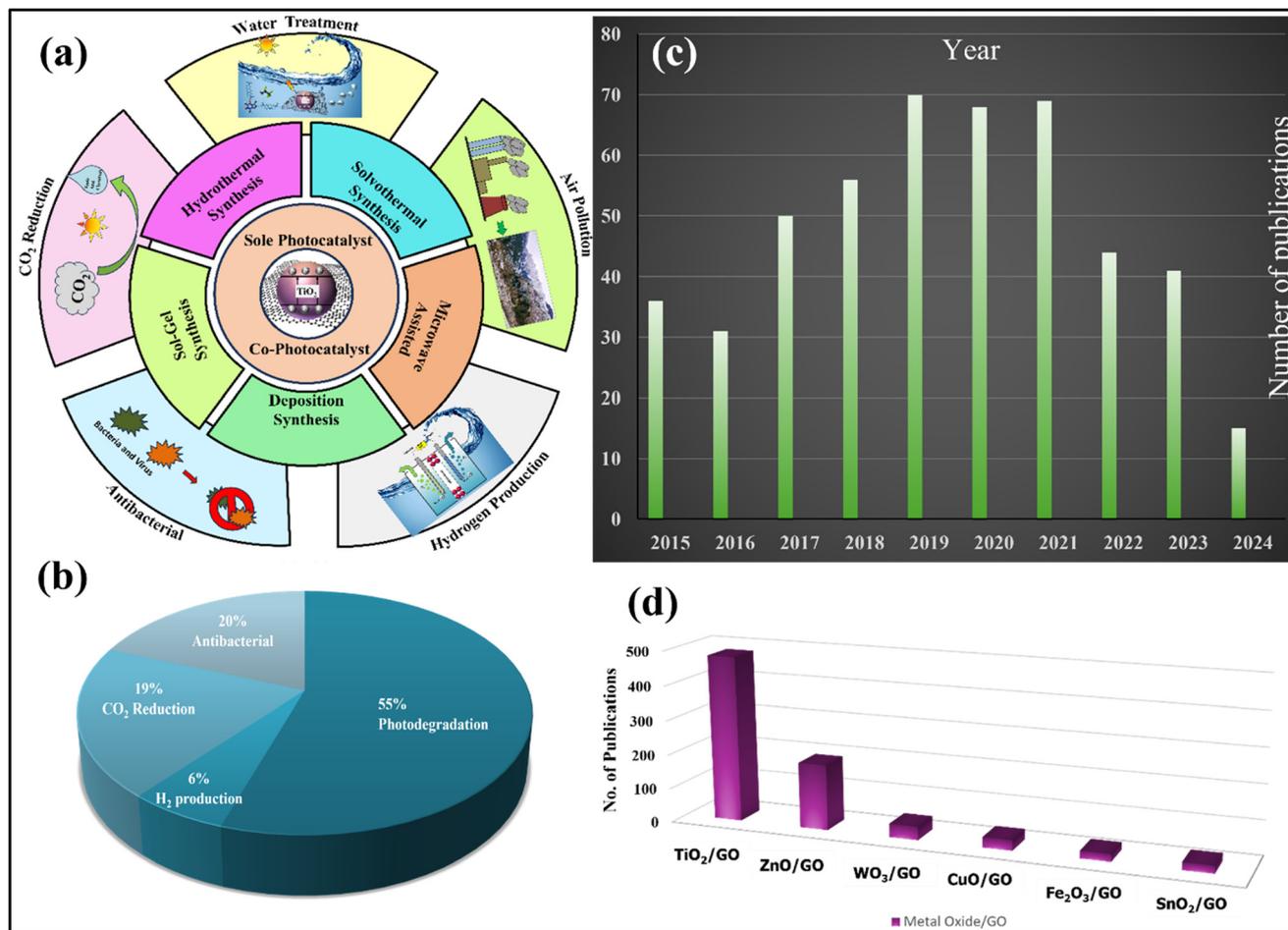
This journal is © The Royal Society of Chemistry 2025

Catal. Sci. Technol., 2025, **15**, 1702–1770 | **1703**

Fig. 1 (a) Schematic of synthesis method and multifunctional applications of GO/TiO$_2$ nanocomposite. (b) TiO$_2$/GO-based papers for different applications published during 2015–2024 (data: Web of Science database). (c) Number of publications (2015–2024) containing keywords TiO$_2$, GO, and photocatalyst in their title. (d) Number of publications on GO-based metal oxides (TiO$_2$, ZnO, WO$_3$, CuO, Fe$_2$O$_3$, and SnO$_2$) during 2015–2024 (data: Web of Science database).

photocatalysts are emerging nanocomposites with versatile potential for sustainable clean energy production and environmental remediation.

In the past five years, the spotlight has largely been on graphene-based semiconductor nanocomposites across various applications.[27–31] However, there has been limited exploration of GO/TiO$_2$ nanocomposites, particularly in the realms of water treatment and energy solutions. This presents a fascinating opportunity for innovation and research in these crucial areas. For example, Campos-Delgado et al.[32] provided a comprehensive review of ternary nanocomposites featuring synthesized or commercial TiO$_2$ combined with GO, specifically for the photodegradation of dyes. These GO/TiO$_2$ composites, often enhanced with metals, semiconductors, and magnetic nanomaterials, demonstrated remarkable dye degradation performances and reusability compared to the standard TiO$_2$. Kong et al.[33] reviewed GO/TiO$_2$ and GO/TiO$_2$-based nanocomposites for the removal of dyes, heavy metals, and oil from wastewater. Their work also included a concise overview of the origins and impacts of pollutants, as well as the roles of GO and TiO$_2$ as photocatalysts. Additionally, their

review discussed the synthesis methods and key findings related to GO/TiO$_2$ nanocomposites in the context of wastewater treatment and pollutant removal. Likewise, Padmanabhan et al.[29] provided a summary of graphene–TiO$_2$ photocatalysts for environmental applications. They offered insights into the fundamental mechanisms and interfacial charge-transfer dynamics within TiO$_2$/graphene nanocomposites. Through a thorough literature survey, they highlighted the importance of these photocatalytic hybrids in environmental remediation, showcasing their key applications such as air and water purification, self-cleaning surfaces, H$_2$ production, and CO$_2$ reduction into valuable fuels. Despite the extensive focus on graphene-based semiconductor nanocomposites over the past five years, there remains a significant gap in research specifically targeting GO/TiO$_2$ nanocomposites for water treatment and energy production, together with a focus on the stability and toxicity posed by nanocomposites. This presents a compelling opportunity for innovation in these critical areas. Recent reviews, such as that by Campos-Delgado, Kong, and Padmanabhan,[29,32,33] have begun to shed light on the efficacy

1704 | Catal. Sci. Technol., 2025, **15**, 1702–1770

This journal is © The Royal Society of Chemistry 2025

of GO/TiO$_2$ composites for pollutant removal and photocatalytic applications. However, a comprehensive review synthesizing these findings and exploring the full potential of GO/TiO$_2$ in environmental remediation and energy generation is essential to guide future research and development efforts.

In the recent past, there has been great progress in synthesizing GO/rGO with tunable characteristics, particularly focused on their semiconducting properties for their standalone photocatalytic activities in various applications.[34,35] This review further provides the comprehensive details of GO as a co-catalyst and sole photocatalyst in various photocatalytic activities and how it is useful in enhancing the photocatalytic properties of TiO$_2$. In addition, there has been progress in understanding role of GO as a co-catalyst and photocatalyst when applied in TiO$_2$-based nanocomposites for different photocatalytic applications, synergistically boosting the photocatalytic efficiency of TiO$_2$ in energy and environmental sectors of current interest including photocatalytic H$_2$ production, CO$_2$ photoreduction, and photodegradation of nano-micro/plastics and other pollutants of emerging concern (*i.e.*, pesticides, pharmaceutical, personal care products, and pathogens/viruses), which have rarely been reviewed in past years. The recent progress in synthesizing GO/TiO$_2$ hybrid nanocomposites with emphasis on various parameters to optimize their composition and optical and surface properties is reviewed and discussed in detail, with emphasis on their advantages and drawbacks. Various other aspects such as the synthesis of highly crystalline GO/TiO$_2$ nanocomposites and role of structural and morphological (0–3D TiO$_2$ nanostructures) properties on photocatalytic efficiencies of the resulting nanocomposites have also been discussed in comparison with nanocomposites with other metal oxide photocatalysts. Together with all these aspects, a great deal of research has been focused on the utilization of natural direct sunlight in photocatalytic applications for real practical applications and structural/morphological stability of materials, their recyclability and long-term applications, which have also been discussed in detail in this review and not found in any recent reviews. Eventually, an analysis on the toxic effects of GO, TiO$_2$ and GO/TiO$_2$ nanocomposites on human health and the environment is presented, together with a discussion on the various challenges in using these photocatalyst nanomaterials for sustainable applications in the field of energy and environmental. Unlike previous reviews, this article presents a comprehensive comparison of GO and TiO$_2$ photocatalysts, shedding light on their synergistic effects when combined to form nanocomposites. Additionally, we provide new insights into the applications of GO/TiO$_2$ composites, particularly in emerging areas such as the degradation of MPs, pesticides, and pharmaceutical pollutants, which have been less explored in the prior literature. This review also focuses on the recent progress in enhancing the photocatalytic performance of these materials by optimizing their synthesis, surface properties, and

structural characteristics. Moreover, we delve into the computational aspects, toxicity concerns and practical challenges in utilizing these nanocomposites for sustainable energy production and environmental remediation, highlighting aspects that have often been overlooked in earlier reviews.

2. TiO$_2$: fundamental principle and photocatalytic properties

Degrading organic pollutants in the air and water is an efficient utilization of heterogeneous photocatalysis.[36] In 1972, Japanese chemist Akira Fujishima made a groundbreaking discovery, *i.e.*, the photocatalytic properties of nanosized TiO$_2$ under ultraviolet (UV) irradiation.[37] This discovery paved the way for numerous applications of TiO$_2$ as a photocatalyst, particularly in energy production by splitting water into H$_2$ and oxygen (O$_2$). The H$_2$ as-produced found utility as a fuel source. By 1995, TiO$_2$-coated glass exposed to sunlight revolutionized the development of self-cleaning glass and anti-fogging coatings.[38,39] Furthermore, nanosized TiO$_2$ materials have been found incorporated in exterior construction materials, such as paints, aimed at reducing airborne pollutants such as nitrogen oxide.[40] TiO$_2$ is a semiconductor with a broad band gap of 3.0–3.2 eV and can be stimulated by UV light. Among the myriad of semiconductor photocatalysts, researchers have identified TiO$_2$ as a superior photoactive material owing to its several advantageous characteristics, including high activity, excellent stability, and non-toxicity. TiO$_2$ occurs in three distinct forms, with its anatase structure being particularly well-suited for photocatalytic applications.[41,42] Photocatalysis operates as a surface phenomenon, wherein organic pollutants, biomolecules, and microorganisms are oxidized, reduced, or degraded into environmentally benign CO$_2$ and H$_2$O in the presence of a photocatalyst.[43] In a typical aqueous medium, during the photocatalysis of organic pollutant degradation, when subjected to UV light with energy equal to or exceeding the band gap of TiO$_2$, its electrons are excited from its valence band (VB) to its conduction band (CB). The resultant photoinduced charge carriers, which are comprised of electrons and holes, possess highly reducing and oxidizing properties. These carriers migrate to the surface of TiO$_2$, where they interact with ambient O$_2$ and H$_2$O molecules. Holes oxidize water molecules to form highly reactive hydroxyl radicals (·OH), while electrons reduce O$_2$ molecules to superoxide radical anions (·O$_2^-$), which are subsequently reduced to ·OH. These highly reactive species, termed reactive oxygen species (ROS), react with harmful organic pollutants on the surface TiO$_2$, leading to their degradation into CO$_2$ and H$_2$. Fig. 2(a) depicts the general mechanism of the TiO$_2$ photocatalyst. The photogenerated holes in the VB of TiO$_2$ exhibit potent oxidation capabilities for decomposing organic substances, while the photogenerated electrons in its CB facilitate reduction processes for organic matter decomposition.[19,43–45] Efforts in photocatalysis have been
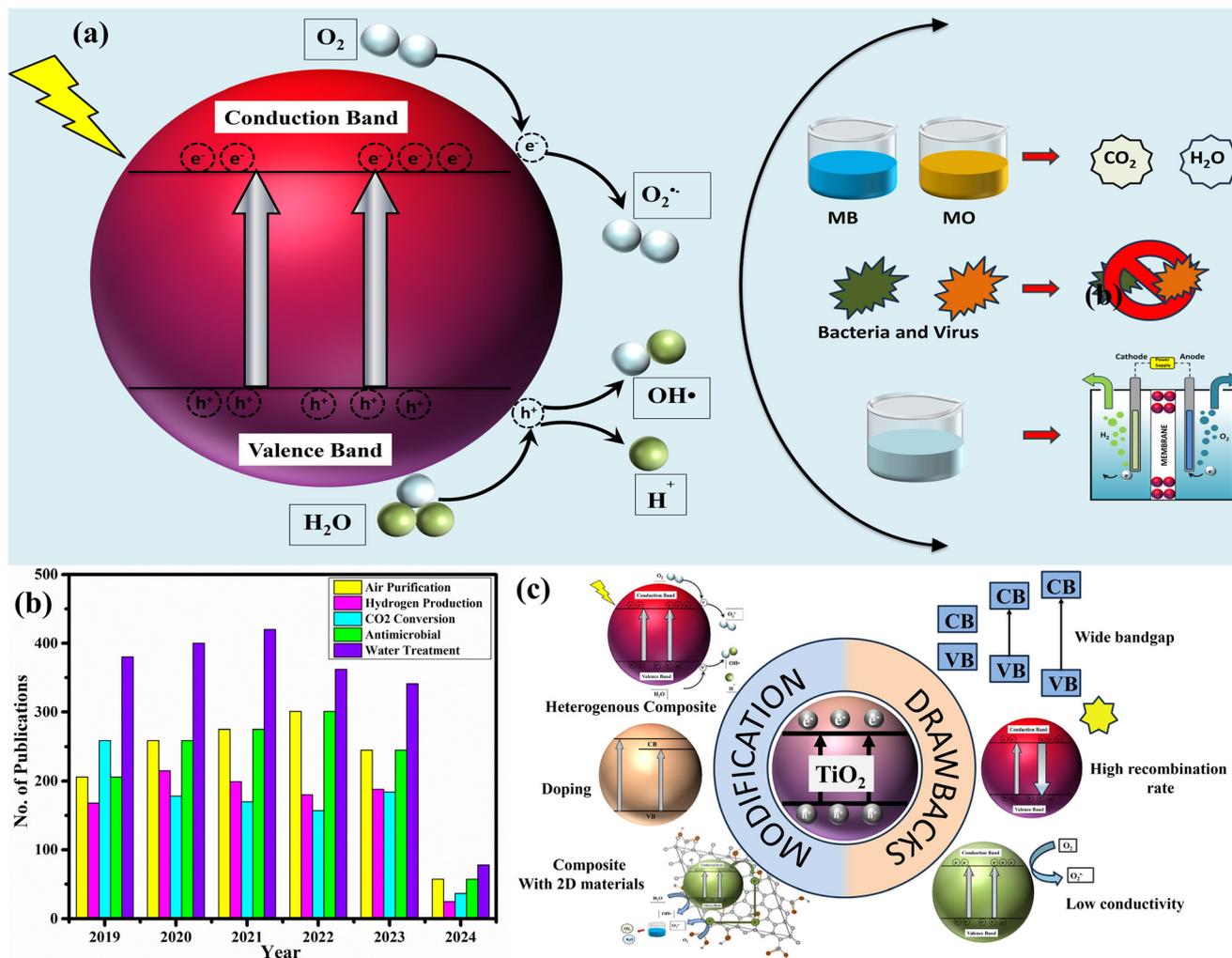
This journal is © The Royal Society of Chemistry 2025

Catal. Sci. Technol., 2025, **15**, 1702–1770 | **1705**

Fig. 2 (a) General photocatalytic mechanism of TiO_2. (b) Number of publications related to TiO_2 in environmental applications in the last 5 years (Web of Science). (c) Drawbacks and possible modifications of TiO_2 as a photocatalyst.

extended to wastewater treatment, with attempts made to mineralize contaminants into CO_2 and H_2O, thereby addressing environmental concerns.[46,47] Fig. 2(b) shows the number of publications in multifunctional applications of TiO_2 in environmental remediation and clean energy production. Fig. 2(c) illustrates both the limitations of TiO_2 as a photocatalyst and highlights potential strategies for overcoming its challenges to enhance its performance.

One of the earliest reported research studies on the photocatalytic degradation of organic molecules using pure TiO_2 was conducted by Kato *et al.*,[48] focusing on the oxidation of tetralin (1,2,3,4-tetrahydronaphthalene). This was followed by McLintock and group,[49] who studied the oxidation of ethylene and propylene using TiO_2 in the same year. Since these pioneering studies, the potential of TiO_2 in the photo-oxidation of organic compounds has been extensively explored over the past several decades. The photodegradation of certain dyes has been proven to be highly effective in the presence of TiO_2. For instance, Singh *et al.*[50] synthesized highly crystalline TiO_2 particles supported

by eggshells using the solvothermal method to effectively decompose MB and rhodamine 6G dyes. The solvothermal synthesis method and the eggshell support improved the effectiveness of the catalyst due to its increased surface area and synergistic effects. Consequently, the optimal performance was achieved when the support and catalyst were used in equal amounts. TiO_2 has also been reported to degrade methyl orange (MO) and Congo red (CR) dyes in the presence of solar radiation, which contains nearly 5% UV light. The degradation efficiency strongly depended on the concentration of TiO_2 used. The optimal concentration of 500 mg L^{-1} was found for the removal of CR, while 1500 mg L^{-1} was optimal for MO. In both cases, total color removal was observed, demonstrating the potential for industry-scale applications.[51] In another study, Houas *et al.*[52] conducted a seminal study, analyzing the formation of intermediates and potential degradation pathways of methylene blue (MB) under UV light irradiation with TiO_2, as illustrated in Fig. 3(a). Their results demonstrated the breakdown of the organic molecule into smaller species. Similarly, Dariani

1706 | *Catal. Sci. Technol.*, 2025, **15**, 1702–1770

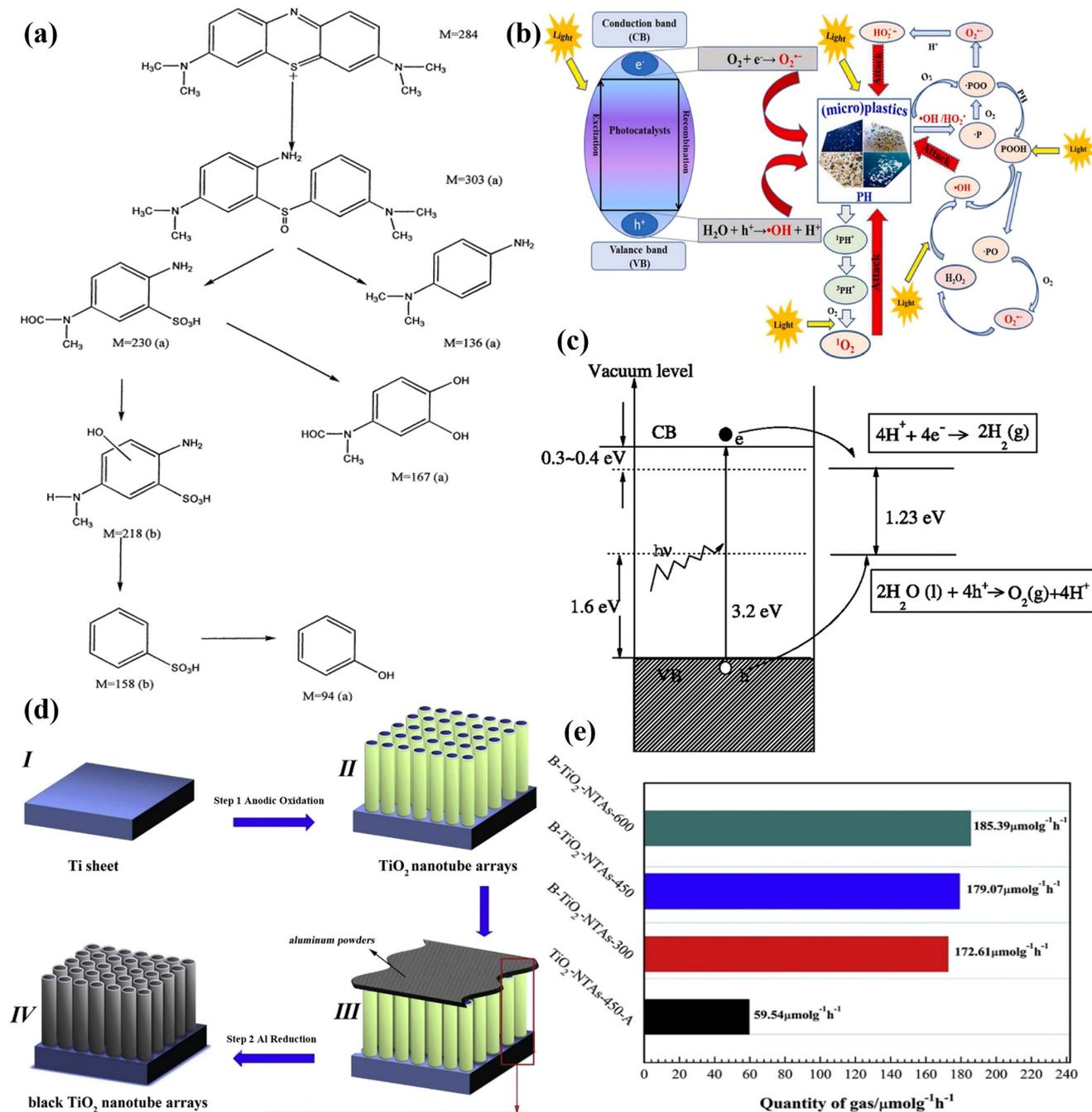This journal is © The Royal Society of Chemistry 2025

Fig. 3 (a) Analysis of intermediates and potential degradation pathways of MB degradation by TiO_2 under UV light irradiation. Reproduced with permission from ref. 52. Copyright (2001), Elsevier. (b) Schematic mechanism of photocatalytic degradation of MPs. Reproduced with permission from ref. 54. Copyright (2022), Elsevier. (c) Band edge positions of TiO_2 relative to the standard redox potentials for H_2 evolution and water oxidation, illustrating its suitability for photocatalytic water splitting. Reproduced with permission from ref. 55. Copyright (2009), the American Physical Society. (d) Synthesis of black TiO_2 nanotube array. (e) CO_2 conversion productivity using black TiO_2 nanotube array. Reproduced with permission from ref. 56. Copyright (2020), Elsevier.

et al.[53] successfully degraded MB using TiO_2 NPs, achieving complete degradation within a few hours. The performance significantly improved when TiO_2 was used at the micro- and nano-scales.

Aromatic oxidation is a key process in the removal of various pharmaceutical pollutants from water, most of which are based on aromatic ring structures. The pharmaceutical compounds

that can be oxidized by TiO_2-produced ·OH radicals include analgesics such as diclofenac[57] and sulfamethoxazole,[58] antibiotics such as amoxicillin[59] and moxifloxacin,[60] and antiepileptics such as carbamazepine.[61] Wu et al.[62] were the first to demonstrate that TiO_2 can degrade the antibiotic tetracycline under both visible and UV light. They conducted a detailed analysis of the intermediate products formed during

This journal is © The Royal Society of Chemistry 2025

Catal. Sci. Technol., 2025, 15, 1702–1770 | 1707

this degradation process using HPLC-MS and suggested the full degradation of tetracycline into CO_2, H_2O, and other small inorganic molecules, a process likely facilitated by the generated $^{\bullet}O_2^-$ radicals and h^+. Their study revealed that the intermediate products generated under visible light differ from that produced under UV light. Under visible light, the $^{\bullet}O_2^-$ produced by TiO_2 initially targets the hydroxyl and methyl groups of tetracycline, leading to the loss of the *N*-dimethyl group and subsequent ring-opening reactions. Under UV light, tetracycline degradation occurs *via* two pathways simultaneously, resulting in a greater variety of intermediate products. Pathway I mirrors the reaction under visible light, while pathway II involves deamination and an esterification process with h^+. Notably, the intermediate products in pathway II were only detected within the first half hour of irradiation and disappeared with longer UV exposure. It was also observed that TiO_2 showed almost the same efficiency even after 4 cycles, showcasing its high reusability characteristic. In another study, Eskandarian et al.[63] successfully removed four highly common pharmaceuticals from water, diclofenac, ibuprofen, sulfamethoxazole, and acetaminophen, using Degussa P25, a nanocrystalline structure comprised of a mixture of rutile and anatase TiO_2. Light-emitting diodes (LEDs) were used as the radiation source and proved more effective with lower wavelength light. Microcystin-LR, a known water toxin, was also degraded by a similar photocatalytic reaction. Similarly, in the study by Mukherjee et al.,[64] TiO_2 was reported as a potent agent for removing aspirin, achieving high effectiveness even under solar irradiation. The photocatalytic degradation resulted in the formation of organic acids, with acetic acid being the most prevalent.

Similar to dyes and pharmaceuticals, conventional wastewater treatment methods are unable to fully eliminate pesticides and microbes, posing the risk of toxic substances accumulating in various organisms throughout the environment.[65] The primary reason for removing pesticide residues from water is their extremely high biological toxicity to aquatic organisms. Even when not lethal, pesticides can significantly reduce the speed and activity of aquatic organisms.[66] Furthermore, many pesticides are non-biodegradable, leading to their accumulation in organisms throughout the food chain. In this case, TiO_2 has proven to be highly effective in degrading pesticides and eliminating microbes. Farner Budarz et al.[67] successfully degraded chlorpyrifos, a phosphate-based pesticide, using photocatalysis with TiO_2 NPs. Nearly 80% pesticide was degraded within one day under UV light. Similarly, Cruz et al.[68] reported the efficient treatment of a stream containing a mixture of four pesticides, diuron, alachlor, isoproturon, and atrazine. Although the catalyst was effective in both pure and regular water, the presence of additional pollutants in regular water significantly reduced the efficiency of TiO_2. This decrease was attributed to the inhibition of radical formation, which is crucial for accelerating the catalytic reaction. Vela et al.[69] used TiO_2 P25 as a photocatalytic removal agent for pesticides. In their study, six commonly found pesticides and insecticides,

malathion, fenitrothion, quinalphos, vinclozolin, dimethoate, and fenarimol, were removed using TiO_2 P25 under solar light. TiO_2 P25 also demonstrated high effectiveness in removing diazinon from water, with over 99% degradation achieved at an optimal pH of 6, as reported by Kalantary et al.[70] The reaction efficiency was primarily influenced by the amount of UV light supplied to the catalyst and the reaction time. Additionally, the concentration of TiO_2 and aeration were shown to positively affect the catalysis process. TiO_2 has also demonstrated significant antimicrobial activity and can be used as a disinfecting agent in water. In 1988, Matsunaga et al.[71] found that TiO_2 powder catalysts killed 99% of *E. coli* bacteria within 0.27 h when exposed to UV radiation (1800 $\mu E\ m^{-2}\ s^{-1}$). Joost et al.[72] applied TiO_2 NPs in the form of a thin film, which proved highly effective in the photocatalytic removal of *E. coli* from water. The cells were rapidly and efficiently inactivated due to the expansion of the cell membrane when adsorbed by TiO_2 and exposed to light. The loss of protoplasm has been suggested as a possible consequence of the membrane expansion, alongside cell distortion, with the rapid degradation of acids also contributing to the membrane expansion.

The photocatalytic degradation of MPs is a complex process that occurs under various conditions.[73] TiO_2 is widely used to remove MPs from wastewater due to its efficiency in initiating photochemical reactions when exposed to UV light. The underlying mechanism for the degradation of MPs *via* TiO_2 is shown in Fig. 3(b). Upon UV exposure, TiO_2 generates electron–hole pairs, which in turn produce reactive species such as $O_2^{\bullet-}$ and $^{\bullet}H$ radicals.[74,75] These radicals play a crucial role in the photocatalytic degradation of MPs by attacking and breaking down the adjacent polymer chains. The degradation process extends to the polymer matrix through the diffusion of ROS. During this process, ·OH radicals specifically target the C–H bonds in polymer molecules, where the H atom, after donating an electron, combines with ·OH to form water. This reaction leaves behind a carbon atom with an unpaired electron, converting the remaining MP molecules into carbon-centered free radicals. Once these radicals are introduced into the polymer chain, they react continuously with various ROS, leading to chain scission and the formation of hydroxyl derivatives, as well as carboxyl and carbonyl intermediates.[54] Domínguez-Jaimes et al.[76] synthesized TiO_2 for the photodegradation of polystyrene (PS) NPs using anodization, resulting in three different photocatalyst structures. TiO_2/T exhibited a nanotube-like structure, TiO_2/B was highly compact with no apparent pores or defined morphology, and TiO_2/M had a multilayer structure, with the lower layer featuring a nanotubular morphology and the upper layer displaying nanograss structures. The photocatalytic degradation results revealed that TiO_2/M achieved the highest polystyrene elimination percentage (23.50% ± 1.02%), followed by TiO_2/T (19.70% ± 0.58%) and TiO_2/B (16.20% ± 0.53%). The superior efficiency of TiO_2/M was attributed to its optimal transfer and separation of photogenerated charge carriers. Kaewkam et al.[77] investigated the UV-assisted TiO_2 photocatalytic degradation of

1708 | *Catal. Sci. Technol.*, 2025, **15**, 1702–1770

This journal is © The Royal Society of Chemistry 2025

virgin LDPE films by TiO_2, focusing on the effects of UV-A (longer wavelength at 352 nm) and UV-C (shorter wavelength at 254 nm). The results demonstrated that combining UV radiation with TiO_2 photocatalysis significantly accelerated the degradation of virgin LDPE films, outperforming the use of either UV radiation or TiO_2 alone. TiO_2 synthesized at 450 °C, which consisted of both anatase and rutile phases, was found to be more photo-catalytically active under UV-A than TiO_2 synthesized at 900 °C, which was composed solely of the rutile phase. Additionally, TiO_2 (rutile) excited by UV-C proved to be much more effective for the photodegradation of LDPE than TiO_2 (anatase + rutile) under UV-C. The results demonstrated that LDPE films degraded most efficiently when exposed to TiO_2 (rutile) along with UV-C light, achieving a weight loss of 17.30% and a carbonyl index of 4.0754. This study also highlighted that UV-C radiation induced faster degradation of LDPE films compared to UV-A radiation due to its higher energy, which more effectively breaks the C-H bonds in LDPE.

Similarly, Lee et al.[78] conducted a study on the photocatalytic degradation of polyamide 66 (PA66) microfibers using various doses of TiO_2. They found that with 100 mg of TiO_2 per liter under UV-C irradiation, the degradation efficiency was maximized, with PA66 microfibers losing 97% of their mass within 48 h. This process also resulted in a relatively low production of by-products, with the chemical oxygen demand (COD) levels remaining below 10 mg L^{-1}. This study suggests that photocatalysis using TiO_2 and UV-C can be an effective approach for treating microfibers in wastewater treatment plants. Nabi et al.[79] investigated the photocatalytic degradation of PS and polyethylene (PE) MPs using TiO_2 films under UV irradiation, focusing on the impact of the PS sphere size and the method for the preparation of the catalyst. They synthesized three types of TiO_2 films (derived from TiO_2 P25) with varying physicochemical properties by altering the synthesis solvent including water (WT), ethanol (ET), and Triton X-100 (TXT). The catalytic performance of these TiO_2 films in degrading PS MPs was evaluated under 12 h of UV light. The degradation efficiencies were 98.4% for the TXT film, 91.04% for the ET film, and 69.25% for the WT film. The superior performance of the TXT-TiO_2 film was attributed to its lower bandgap energy and efficient charge separation, which were examined in detail. This efficient charge separation enables TXT to produce a greater number of electron–hole pairs under light irradiation and prolongs the duration of charge separation, leading to enhanced photocatalytic activity for PS removal.

TiO_2 also has been widely utilized in the fields of H_2 production and CO_2 reduction due to its excellent photocatalytic properties. For a spontaneous PEC water-splitting process, the hydrogen and oxygen redox reactions must fall within the range defined by the valence band maximum (VBM) and conduction band minimum (CBM). This requires the band edges to straddle the water redox potential levels. TiO_2 meets this criterion, as shown in Fig. 3(c), with its CBM positioned slightly above the hydrogen evolution potential and its VBM well below the water

oxidation potential. TiO_2 photocatalytic water-splitting technology shows great potential for cost-effective and eco-friendly solar hydrogen production, playing a crucial role in advancing the hydrogen economy of the future. The early work on TiO_2 photoelectrochemical hydrogen production was reported by Fujishima and Honda.[37] Yu et al.[80] used P25 for H_2 generation in an ethanol and water mixture under wavelengths less than 300 nm, achieving a generation rate of 13.7 mm h^{-1} g^{-1}. To enhance this rate, Janek and co-workers[81] prepared newly porous TiO_2 through a sol–gel method with templates, resulting in a tenfold efficiency improvement over crystalline TiO_2 NPs. Converting CO_2 from fossil fuel combustion into hydrocarbon fuels is an effective way to address the greenhouse effect and energy crisis. In recent decades, many semiconductor materials have been extensively studied for CO_2 photoreduction.[82] Among them, TiO_2 nanomaterials have received significant attention over the past two decades due to their low cost, non-toxicity, and good chemical stability.[83] Huang et al.[82] synthesized TiO_2 nanotubes (TNT) and nanorods (TNR) via a one-step hydrothermal method. The photocatalytic activities of these catalysts for CO_2 reduction were investigated under 9 h of irradiation from a 300 W Xe arc lamp equipped with a UV 420 nm bandpass filter. The maximum yields of CH_4 were 19.16 μmol g_{cat}^{-1} for TNT and 12.71 μmol g_{cat}^{-1} for TNR. The enhanced photocatalytic activity of TiO_2 nanotubes and nanorods was attributed to the presence of oxygen vacancies and defects formed during the calcination process, as well as their special structures, which accelerate electron transfer. The superior activity of TNT compared to TNR may be due to its unique hollow tubular structure and larger surface area. Similarly, Di et al.[84] synthesized porous TiO_2 microspheres using a microwave-assisted solvothermal method, followed by heat treatment in air. The hierarchical TiO_2 possessed a large specific surface area, providing numerous active sites for CO_2 adsorption and conversion. These TiO_2 nanostructures exhibited significant photocatalytic activity for CO_2 reduction to methane and methanol. The synthesized TiO_2 demonstrated superior photocatalytic CO_2 reduction efficiency compared to anatase TiO_2 and P25. Gao et al.[56] synthesized black TiO_2 nanotube arrays (B-TiO_2 NTAs) through the aluminothermic reduction of anodized TiO_2 nanotube arrays (TiO_2 NTAs), as shown in Fig. 3(d). They found that the oxygen partial pressure at the micro-region of the TiO_2 NTA surface was crucial for the formation of black TiO_2 NTAs. The oxygen vacancies in the B-TiO_2 NTAs introduced new defect energy levels within the TiO_2 band gap, which reduced its band gap and expanded its visible light absorption. Additionally, these oxygen vacancies served as catalytic sites, accelerating surface reactions for the photocatalytic reduction of CO_2 to CO. B-TiO_2 NTAs annealed at 600 °C demonstrated an exceptional photocatalytic performance in CO_2 reduction to CO, achieving a yield of 185.39 μmol g^{-1} h^{-1} under visible light, as shown in Fig. 3(e). This outstanding performance was attributed to the oxygen vacancy self-doping, which significantly enhanced three key

This journal is © The Royal Society of Chemistry 2025

Catal. Sci. Technol., 2025, 15, 1702–1770 | 1709

factors including photoinduced charge generation, charge separation and transport, and interfacial reactions.

However, because only 3–5% of the sunlight is UV-visible, the utilization of TiO_2 is restricted. When considering the TiO_2 photocatalysis process, a few disadvantages emerges. (1) Due to its wide bandgap (3.2 eV), only photons with sufficient energy can excite electrons from the VB to the CB of TiO_2, limiting the ability of this material to effectively harness sunlight. (2) In contrast to charge transfer, which takes a significantly longer period, carrier recombination occurs inevitably when excited electrons and holes combine. As a result, there is a significant suppression of the photoexcitation effect.[85,86] Thus, the inherent disadvantages of photocatalysts can be addressed by employing heterojunction photocatalysis. Heterojunctions create an interface between two distinct semiconductor materials, each with different energy band structures. Upon illumination by an appropriate light source, electron–hole pairs are generated on the surface of both semiconductors A and B. In a heterojunction, these two semiconductors work in tandem to reduce the recombination losses. The formation of heterojunctions in photocatalytic materials is a strategic approach to optimize their performance by leveraging the complementary properties of different semiconductors.[87] Therefore, the selection of the heterojunction counterpart of titania is a very important factor. The total absorption efficiency of visible light absorption is increased by the heterostructure formation.[88,89] This enhances the total photocatalytic efficiency and leads to the greater separation of charges. Semiconductors play a key role in the formation of heterojunctions in the field of photocatalysis. Efficiency and charge migration are determined by the band alignment of the band edges and total charge flow across the heterojunction.[90] A growing number of researchers is interested in 2D materials due to their better physical and chemical qualities, affordability, and adaptability in preparation techniques.[91–93] These 2D materials work exceptionally well for photocatalysis applications owing to their huge surface area, appropriate bandgap, overall stability, and high charge mobility. When coupled with TiO_2, the reaction is supported and has active sites due to the large specific surface area, and the increased utilization of sunlight also results in the formation of energy level matching, inhibiting recombination.[94,95] For instance, Ramesh et al.[96] found that rGO/TiO_2 demonstrated a superior performance, surpassing rGO/ZnO and rGO/WO_3 in the photocatalytic degradation of MB and bisphenol A (BPA). The rGO/TiO_2 catalyst achieved photodegradation efficiencies of 87.5% for MB and 98.5% for BPA, whereas the rGO/ZnO and rGO/WO_3 catalysts showed efficiencies of only 78.3% and 67.8%, respectively. In rGO/TiO_2, the rGO sheets serve as excellent electron acceptors, facilitating the rapid transfer of photo-induced electrons from the CB of TiO_2 nanotubes to their surfaces. This process reduces charge carrier recombination, thereby enhancing the photocatalytic performance of rGO/TiO_2.

3. Graphene oxide nanostructures: semiconducting properties and roles in photocatalysis

Graphene has become a 'star' material since it was discovered by Geim and Novoselov in 2004, and since then the manufacture and uses of this rigorous 2D material have rapidly received extensive interest.[97,98] Graphene consists of a 2D hexagonal lattice of carbon atoms, with each atom covalently bonded to its neighbors, forming an sp^2-hybridized structure.[99–101] The presence of π bonds and delocalized electrons contributes to the excellent conductivity of graphene. However, because of its hydrophobic sp^2 domain, graphene is not ideal for use in photocatalytic processes. Alternatively, GO is a single layer of graphite oxide, which can be produced by breaking down graphite oxide into layered sheets through methods such as sonication or mechanical stirring.[102–104] The lattice structure of GO and presence of different oxygen-containing groups (mainly epoxy and hydroxyl groups) give it many intriguing properties. Firstly, the functional groups on the surface of GO serve as efficient anchoring sites for binding various active species. Additionally, GO offers adjustable electronic properties. GO is an insulator due to its high percentage of sp^3 hybridized carbon atoms bonded with oxygen-containing groups, resulting in a sheet resistance of around 1012 Ω sq^{-1} or higher.[105] However, when GO is reduced, the sheet resistance of rGO can decrease significantly, potentially transforming the material into a semiconductor or even a graphene-like semimetal.[106,107] Research has shown that the band gap of GO can be modified by controlling its distribution, arrangement, and proportion of the epoxy and hydroxyl groups.[107] Fig. 4(a) depicts the chemical structures and electronic band diagrams of graphene, GO and rGO.

The VBM and CBM of graphene are formed by its bonding π and antibonding π* orbitals, respectively, which intersect at the Brillouin zone corners, making pristine graphene a zero-bandgap semiconductor.[113–115] The close C–C bond length leads to a significant overlap of the electron bands, causing the electrons and holes in graphene to behave like massless charges. In contrast, GO contains covalently bonded oxygen functional groups, and these C–O bonds disrupt the extended sp^2 conjugated network, transforming the zero-bandgap graphene into a semiconductor.[116,117] The CBM of GO is comprised of an antibonding π*-orbital, while its VBM is composed of an O 2p orbital, rather than π-orbital.[118,119] As the carbon-to-oxygen (C/O) ratio increases, the band gap of GO decreases from 3.5 to 1 eV. GO, and with its oxygen-containing functional groups, it acts as a p-type semiconductor, and thus can be converted from a p-type to n-type semiconductor by replacing its oxygen-containing groups with nitrogen-rich groups.[120] When light of an appropriate frequency interacts with a solution containing GO nanosheets and organic molecules, the π–π* excitation of the electrons in its conjugated sp^2 domains generates
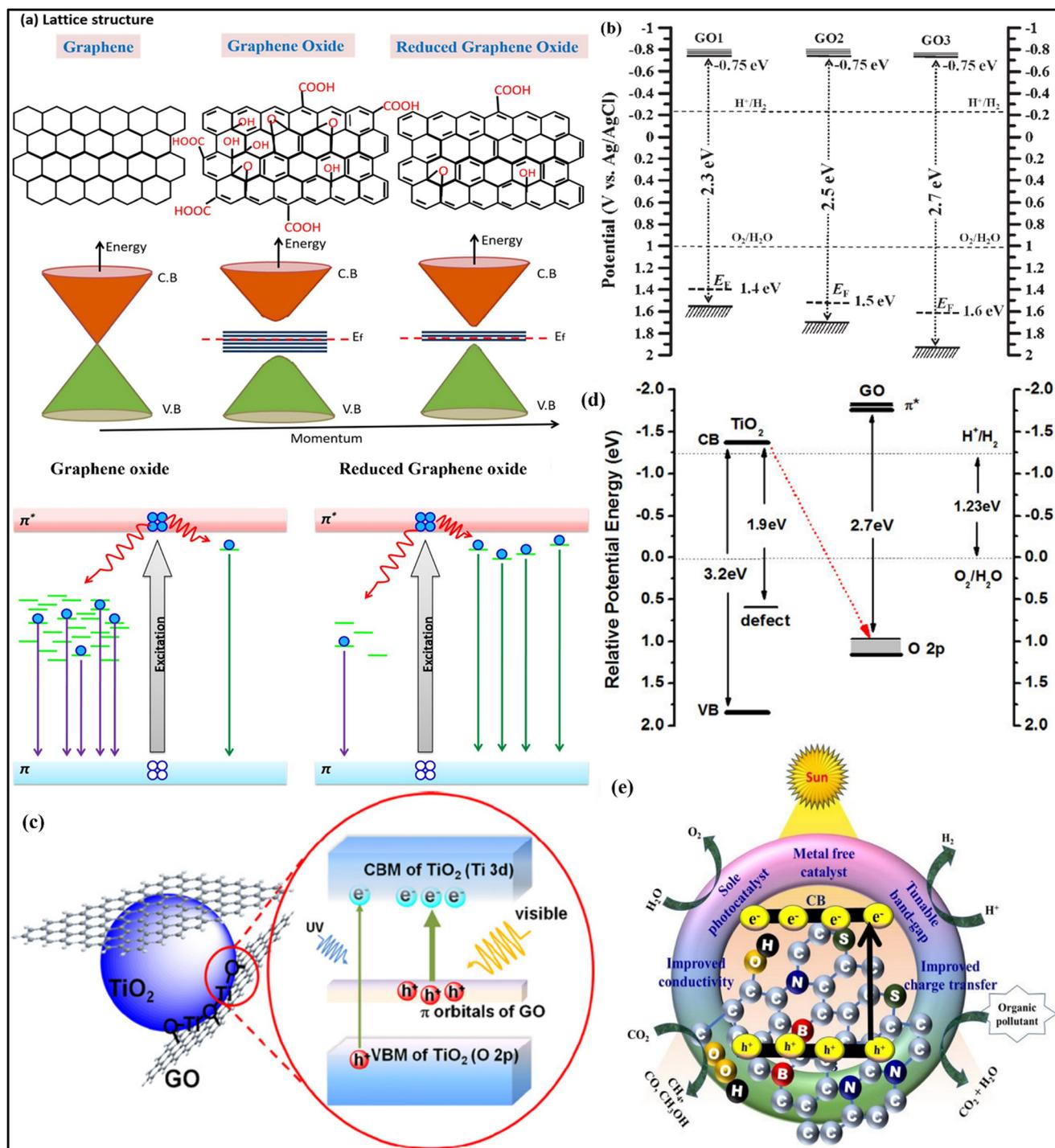
1710 | *Catal. Sci. Technol.*, 2025, **15**, 1702–1770

This journal is © The Royal Society of Chemistry 2025

Fig. 4 (a) Chemical and electronic band diagrams of graphene, GO, and rGO, along with the electronic transitions observed in GO and rGO.[108] Copyright (2018), Springer Nature. (b) Schematic energy level diagrams of GO specimens compared to the redox potentials for water reduction and oxidation. Reprinted (adapted) with permission from ref. 109. Copyright (2011), the American Chemical Society. (c) Reduction of the bandgap and extension of the light absorption range of TiO_2 through the formation of Ti–O–C bonds between surface Ti atoms of TiO_2 and the unpaired π-electrons of GO. Reproduced with permission from ref. 110. Copyright (2013), Elsevier. (d) Schematic of the energy levels of TiO_2 and the localized sp^2 domains of GO.[111] Copyright (2012), the Optical Society of America. (e) Multifunctional photocatalytic applications of GO.[112] Copyright (2022), the Royal Society of Chemistry.

photoexcited electrons and holes.[121] When oxygen and water molecules react with the photogenerated electrons and holes, ROS are formed. These ROS ultimately break down dyes and other organic pollutants, leading to the release of CO_2 and H_2O. According to Yeh et al.,[109] the band gap of GO increases with an increase in its oxygen content, as shown in Fig. 4(b).

This journal is © The Royal Society of Chemistry 2025

Catal. Sci. Technol., 2025, **15**, 1702–1770 | **1711**

Electrochemical analysis, combined with the Mott–Schottky equation, revealed that the conduction and VB edge levels of GO with an optimal oxidation level are well-suited for both water reduction and oxidation. In this case, although its CB edge shows minimal variation with changes in its oxidation, the VB edge of GO primarily determines its bandgap width.

In addition to its electrical and semiconducting properties, GO also enhances photocatalysis through its surface adsorption characteristics.[122–124] Due to its 2D structure, abundant oxygenated functional groups, and high specific surface area, GO is an ideal support material to boost the adsorption capacity of composite photocatalysts.[125] The interactions between adsorbates and GO vary depending on the reaction system and can include physical, electrostatic, and chemical interactions. Besides the physical adsorption of the target reactants on the surface of GO, its oxygen-containing functional groups enable interactions with a wide range of molecules and metal ions. Furthermore, the aromatic regions of GO can engage in π–π stacking interactions with organic pollutants containing aromatic structures, further improving the adsorption of reaction substrates.[126] This enhanced adsorption capacity facilitates the concentration of target substrates from the solution on the photocatalyst surface, enabling more effective interactions with active species, and thereby increasing the efficiency of photoredox reactions.[123,127]

Hence, in recent years, significant research has been dedicated to GO-based photocatalyst nanomaterials, positioning them as a promising class of emerging photocatalysts. GO, a chemically oxidized form of graphene, exhibits notable structural modifications due to the incorporation of oxygen-based functional groups, such as carboxylic (–COOH), hydroxyl (–OH), and epoxy groups. These polar groups not only enhance the hydrophilicity of GO but also facilitate strong interactions with water molecules, enabling its better dispersion in aqueous environments. However, unlike graphene, GO is less conductive, primarily due to the disruption of its sp^2 network by sp^3 C–O bonds, which introduce structural disorder. However, this structural arrangement contributes to the dispersibility of GO, given that its sp^3 domains with hydrophilic oxygen-containing functional groups complement its hydrophobic π-conjugated sp^2 regions. The electronic structure of GO also undergoes a transformation, where its VB origin shifts from the π-orbital of graphene to the oxygen 2p orbital, while its CB edge remains as the π* orbital. This unique band structure, coupled with its adjustable bandgap in the range of 2.2 to 4 eV, makes GO a versatile semiconductor capable of absorbing light across the UV to visible spectrum. By carefully controlling its oxidation level, the photocatalytic properties of GO can be optimized, making it a highly adaptable material for various applications including adsorbents and photocatalysis.

However, despite its inherent photocatalytic properties, GO is more commonly utilized as a support material for other photocatalysts, such as TiO_2 and ZnO. Its primary role is to enhance their photocatalytic efficiency by reducing the recombination rate of electron–hole pairs and facilitating electron transport. As illustrated in Fig. 4(c), GO can also extend the light absorption range of TiO_2 by forming Ti–O–C bonds through interactions with the unpaired π-electrons on its surface. This integration significantly improves the photocatalytic performance of GO–TiO_2 composites under visible-light irradiation.[128] Bao et al.[111] plotted a schematic diagram of the energy levels of TiO_2 and the localized sp^2 domains of GO with respect to the water reduction and oxidation potentials, as shown in Fig. 4(d). They identified an indirect optical transition (IOT), represented by red dots, in a hybrid spherical structure composed of alternating TiO_2 and GO nanosheets through photoluminescence (PL) spectra and time-resolved measurements. In the GO/TiO_2 composite, this IOT was attributed to the hole transfer from TiO_2 to the localized sp^2 domains of GO. This discovery shed new light on the interactions between the sp^2 domains of GO and other semiconductor materials, an aspect that has been largely overlooked in the literature. From a technical perspective, precise control of the band alignment of individual components in GO-based composites can lead to tunable fluorescence properties. Moreover, it enables efficient carrier injection and collection, making these materials highly advantageous for applications in optical and electronic devices. This insight opens new pathways for optimizing GO-semiconductor hybrid materials for advanced optoelectronic technologies.

Research has demonstrated that GO can be further enhanced through doping to boost its photocatalytic activity for various applications, as illustrated in Fig. 4(e).[129] Therefore, investigating both GO and rGO is essential for gaining a deeper understanding of the underlying mechanism for the photocatalytic performance of GO.

3.1. GO as a sole photocatalyst

GO has become the focus as a photocatalyst due to its distinct optical properties and adjustable band gap, opening the door to various photocatalytic applications.[130] Studies have explored its potential as a sole photocatalyst, showing promise as a future key material in this field.[12,131] In particular, GO and its reduced form, i.e., rGO, have demonstrated impressive performances in the photodegradation of organic environmental pollutants, highlighting their suitability as standalone photocatalysts.[132] The oxide form of graphene contains functional groups such as hydroxyl and carboxyl groups, which enhance its interaction with other molecules. Moreover, the ability of GO to absorb a broad spectrum of light, including visible light, contributes to its versatility as a photocatalyst.[133] Yeh et al.[116] demonstrated that the VB maximum of GO can be lowered by increasing the oxidation degree of graphite during the synthesis of GO. This adjustment led to the widening of the band gap of GO as its degree of oxidation increased. Other studies indicated that the band gap structure of GO is closely connected to the presence of oxygen-containing functional
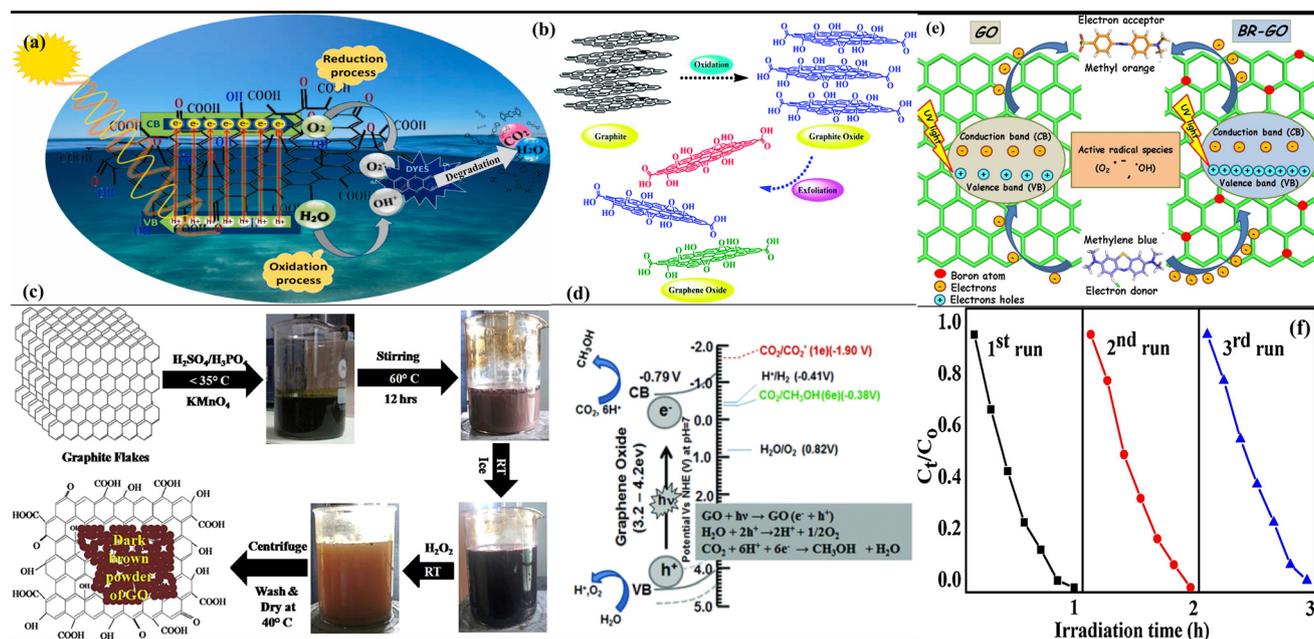
1712 | Catal. Sci. Technol., 2025, 15, 1702–1770

This journal is © The Royal Society of Chemistry 2025

Fig. 5 (a) Mechanism of photocatalytic degradation of organic pollutant by sole GO. Reproduced with permission from ref. 135. Copyright (2024), Elsevier. (b) Schematic of oxidation of graphite into GO.[136] Copyright (2020), the Royal Society of Chemistry. (c) Experimental step for the synthesis of GO nanosheets. Reproduced with permission from ref. 137. Copyright (2016), Elsevier. (d) Schematic of CO_2 reduction on GO.[138] Copyright (2013), the Royal Society of Chemistry. (e) Photodegradation mechanism of MB under direct sunlight in presence of boron-doped GO as a photocatalyst. (f) Stability of boron-doped GO for the degradation of MB. Reproduced with permission from ref. 137 and 139. Copyright (2018), Elsevier.

groups.[134] Fig. 5(a) depicts the mechanism of GO as a sole photocatalyst for pollutant degradation in wastewater and Fig. 5(b) shows the oxidant intercalation oxidation and sheet peeling of graphite into GO.

GO exhibits photocatalytic activity under light irradiation, allowing it to degrade organic pollutants through the production of ROS. Recently, Shabil Sha et al.[140] synthesized rGO for the photocatalytic degradation of indigo carmine (IC) and neutral red (NR) dyes. rGO exhibited an excellent photocatalytic performance, almost completely degrading both pollutants. The optimal results were achieved at pH 10, where rGO managed to degrade over 90% of the dyes even after repeating the reaction up to five times, demonstrating its high stability and reusability. The photocatalytic degradation behavior of aromatic micropollutants (AMPs) is complex and varies, largely due to the properties of different substituents on the benzene ring. Thus, to address this challenge, Wang et al.[141] prepared GO to degrade AMPs under a 35 W xenon lamp. GO successfully degraded AMPs within 60 min, with its photodegradation efficiency varying across different AMPs. Its efficiency reached as high as 91.68% for methyl 3-aminobenzoate but was lower at 31.28% for methyl 4-hydroxybenzoate. It was inferred that the molecular structure characteristics of AMPs significantly influence the efficiency of their photooxidation in the photo-GO system. The Hammett correlation analysis indicated that AMPs with electron-donating groups are easier to degrade, suggesting that the electronic nature of their substituents plays a crucial role in determining the photodegradation efficiency.

Sandhu et al.[35] synthesized GO using an improved Hummers method to assess its photocatalytic degradation of contaminants of emerging concern (CEC). The experimental results demonstrated that GO nanostructures exhibit higher photocatalytic activity when exposed to sunlight compared to UV radiation. This enhancement in the photocatalytic properties of GO is attributed to the presence of oxygen-containing functional groups and other imperfections introduced during the oxidation of pure graphite powder. These functional groups play a crucial role by delaying the electron–hole recombination rate and providing active sites for photocatalytic reactions. This leads to improved photocatalytic efficiency, making GO a promising material for degrading contaminants when utilized as a photocatalyst. In a similar study, Kumar and coworkers[137] prepared GO with precise control of its thickness and molecular structure, as shown in Fig. 5(c). The presence of oxygen-containing functional groups on GO nanosheets introduced through chemical treatment imparted remarkable optical properties to the material. To investigate the photocatalytic degradation of MB dye using GO nanosheets as a photocatalyst, their sunlight-driven photocatalytic activity was tested. When GO was added to the dye solution, the degradation rate of MB dye was rapid, with a photodegradation efficiency of approximately 60%. The proposed mechanism indicated that when light interacts with the solution containing dye and GO as the photocatalyst, photoexcited e^- and h^+ are generated via π–π^* excitation in the π-conjugated sp^2 domains of GO. Subsequently, these photogenerated e^- and h^+ react with O_2 and H_2O molecules to produce ROS. Ultimately, these ROS

This journal is © The Royal Society of Chemistry 2025

Catal. Sci. Technol., 2025, **15**, 1702–1770 | **1713**

degrade dye molecules into CO_2 and H_2O, effectively breaking down the dye.

Govindan et al.[34] synthesized single-layer GO nanosheets and explored their application in the photodegradation of MO. The prepared nanosheets exhibited a band gap in the range of 3.19 to 4.4 eV, resulting in 91% degradation of the dye under UV light irradiation. Similarly, Singh et al.[142] investigated the photocatalytic degradation of CR dye under UV light. Their results demonstrated the complete degradation of CR dye in the presence of GO catalyst within just 100 min, following first-order kinetics. In another study, Abd-Elnaiem et al.[143] synthesized a porous GO sample using an improved Hummers method. The prepared GO sample exhibited semiconducting properties with an appropriate band gap and lower electron–hole recombination rate. The photocatalytic degradation efficiency of the prepared GO was studied with MB dye, showing that 88.3% of MB dye was degraded by the GO sample under simulated UV-visible irradiation.

Siong et al.[144] prepared rGO at various reduction temperatures through a solvothermal approach. At pH 11, rGO exhibited remarkable photocatalytic efficacy, almost eliminating 98.57% of MB when exposed to a 60 W m^{-2} UV-C light source. The MB photodegradation activity of rGO remained consistent, with no significant decrease observed after five successive cycles. In a separate study,[132] the photoactivity of GO and rGO for MB dye photodegradation was investigated using photoelectrochemical (PEC) measurements. rGO was prepared using an optimized autoclave. The deoxygenation of GO resulted in a reduction in its bandgap energy from 3.75 eV to 3.10 eV in rGO, consequently introducing defects. Similarly, Wong et al.[145] reported the photocatalytic degradation of Reactive Black 5 dye molecules by synthesizing rGO from GO, achieving improved photoactivity and highlighting the potential of rGO as an effective photocatalyst.

Several studies indicate that GO is not always an efficient photocatalyst for dye degradation. Thus, to address this limitation and enhance its catalytic efficiency, doping GO with metals and non-metals has emerged as a promising strategy. This approach can improve both the charge transfer characteristics and overall photocatalytic performance of GO.[146–148] For instance, Singh et al.[139] doped rGO with boron to enhance the degradation of organic pollutants, such as MO and MB. The doping process increased the band gap of GO from 2.8 to 3.00 eV in boron-doped GO. The photocatalytic degradation of 98% of MO in 160 min and 99% of MB in 70 min was observed with GO, while boron-doped GO achieved the same levels of degradation in just 100 and 50 min, respectively. The photocatalytic mechanism of boron-doped GO in degrading organic pollutants and its high efficiency and high stability after 3 cycles is shown in Fig. 5(e and f), respectively. Tang et al.[149] prepared boron-doped graphene oxide (B-doped GO) using a simple one-step reflux method with graphite powder as the precursor. The photocatalytic degradation results revealed that only about 50% of the rhodamine B (RhB) dye was degraded within 120 min under UV light irradiation using a 300 W Hg lamp. In contrast, 100% of the dye was degraded under visible light irradiation. B-doped rGO demonstrated a superior photocatalytic performance compared to undoped GO. The improved photoactivity of B-doped rGO was attributed to the photosensitization of the RhB dye, which facilitated enhanced electron migration from the excited dye molecules to B-doped rGO. This efficient electron transfer led to a better overall photocatalytic performance. The role of GO as the sole photocatalyst in dye degradation and CO_2 reduction is summarized in Table 1.

Experimental studies have confirmed the photocatalytic reduction capability of GO for water splitting and the reduction of organic matter. These findings suggest that GO itself may have the potential to photocatalytically reduce CO_2,

Table 1 GO as the sole photocatalyst in pollutant degradation and CO_2 reduction

Photocatalyst	Role of GO	Pollutant	Irradiation source	Irradiation time	Efficiency	Ref.
GO	Active photocatalyst	MB	Visible light	50 min	60%	137
GO	Sole photocatalyst	MO	UV light	120 min	91%	34
GO	Sole photocatalyst	CR	UV light	120 min	90%	142
GO	Sole photocatalyst	Methyl-3-aminobenzoate	35 W xenon lamps	60 min	91.68%	141
GO	Sole photocatalyst	MB	Sunlight and UV light	—	—	35
GO	Sole photocatalyst	MB	UV light	70 min	88.3%	143
GO	Sole photocatalyst	MO	UV light	160 min	98%	139
GO	Sole photocatalyst	MB	UV light	70 min	99%	139
rGO	Sole photocatalyst	IC	Sunlight	—	91.85%	140
rGO	Sole photocatalyst	NR	Sunlight	100 min	90.17%	140
rGO	Sole photocatalyst	MB	UV light	120 min	—	132
rGO	Sole photocatalyst	MB	UV light	120 min	98.57%	144
B-doped GO	Sole photocatalyst	MO	UV light	100 min	98%	139
B-doped GO	Sole photocatalyst	MB	UV light	50 min	99%	139
B-doped GO	Sole photocatalyst	Volatile organic compounds	UV light	6 h	80%	150
B-doped GO	Sole photocatalyst	RhB	Visible light	130 min	~95%	149
GO	Sole photocatalyst	CO_2 reduction	Simulated sunlight	240 min	1.23 μmol g_{cat}^{-1} h^{-1}	151
GO	Sole photocatalyst	CO_2 reduction	UV-irradiation	240 min	0.95 μmol g_{cat}^{-1} h^{-1}	151
GO	Sole photocatalyst	CO_2 reduction	Simulated sunlight	360 min	0.172 μmol g_{cat}^{-1} h^{-1}	138

although this possibility has been scarcely explored. For example, Kuang et al.[151] investigated the intrinsic ability of graphene for CO_2 conversion as a sole photocatalyst and the effect of light irradiation by exposing GO to simulated sunlight (GO_{SS}) and UV-irradiation (GO_{UV}), thus altering the physicochemical properties of GO. The CO generation rates were 1.23 μmol g_{cat}^{-1} h^{-1} for GO_{SS} and 0.95 μmol g_{cat}^{-1} h^{-1} for GO_{UV} after 4 h, which were 2.7-fold and 2.1-fold higher than that of pristine GO (0.46 μmol g_{cat}^{-1} h^{-1} at 4 h), respectively. This suggests that irradiation enhances the photocatalytic reduction activity of GO towards CO_2. Similarly, Hsu et al.[138] investigated the photocatalytic conversion of CO_2 to methanol using GO as a promising photocatalyst. They found that the conversion rate of CO_2 to methanol on GO was 0.172 μmol g_{cat}^{-1} h^{-1} under visible light, which was six times higher than that of pure TiO_2. The mechanism proposed for high efficiency towards the conversion of CO_2 to methanol was via six-electron reaction

in which photogenerated e^- and h^+ irradiated on GO reacted with CO_2 and H_2O to produce CH_3OH, as shown in Fig. 5(d).

In conclusion, the promising photocatalytic properties of GO as a sole photocatalyst have been well-demonstrated through various studies, particularly in the degradation of organic pollutants and potential applications in CO_2 reduction. The ability to adjust the band gap of GO and enhance its interaction with other molecules through functional groups makes it a versatile and effective photocatalyst. Although various studies have shown the high photocatalytic efficiency of GO for various applications, the results are not always consistent. Thus, to address this limitation, the use of GO as a co-catalyst has emerged as a promising strategy. By combining GO with other catalytic materials or through doping with metals and non-metals, it is possible to enhance its photocatalytic efficiency, optimize its charge transfer, and expand its application potential in environmental and energy-related processes.
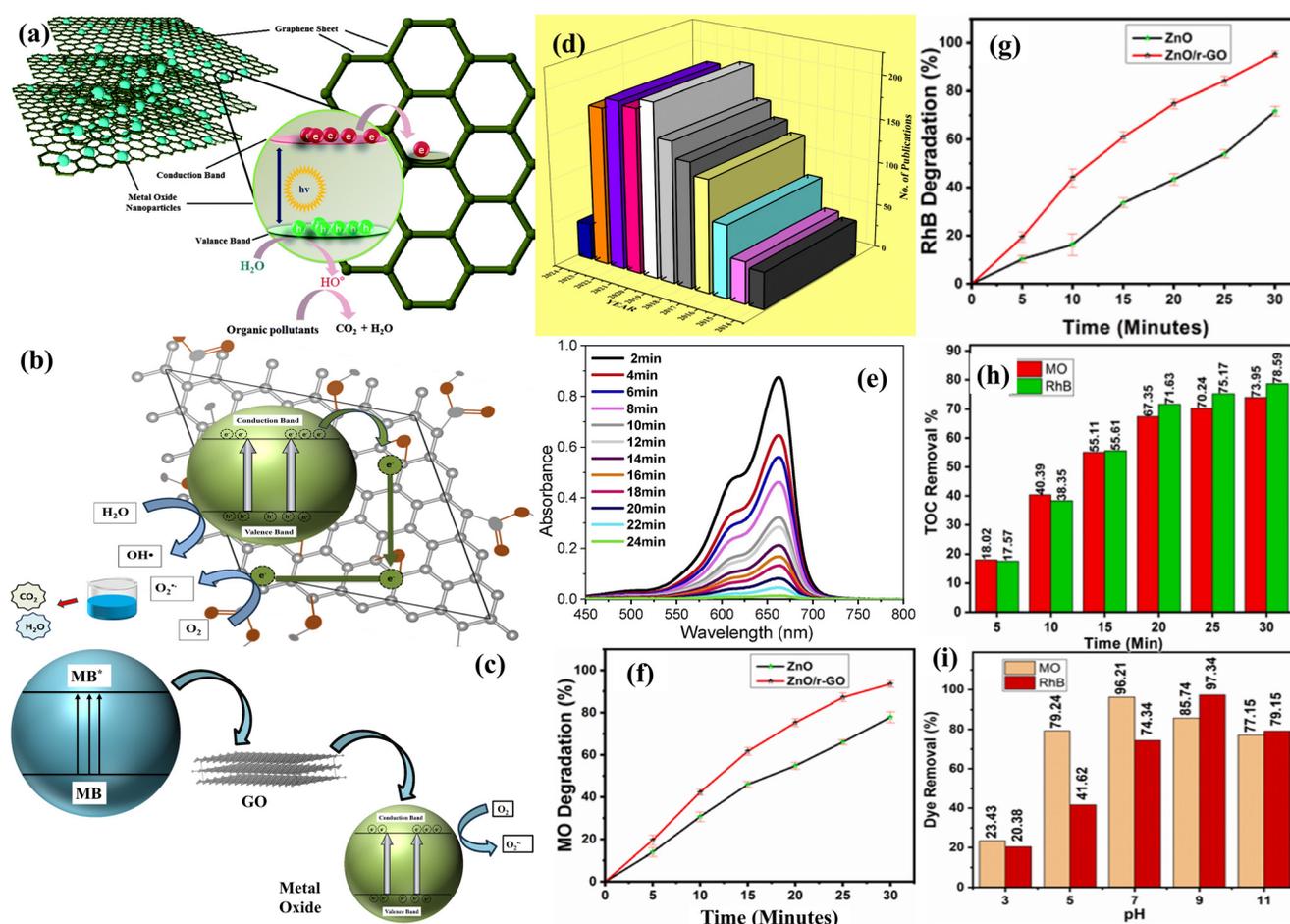

Fig. 6 (a) Electron transfer from the CB of a metal oxide to graphene via a percolation mechanism. Reproduced with permission from ref. 163 Copyright (2024), Elsevier. (b) Chemical mechanism involving the photodegradation of dyes by GO metal oxide photocatalysts, highlighting the function of GO as a charge carrier to boost the photocatalytic efficacy of GO–metal oxide nanocomposites. (c) Schematic of the efficient charge transfer facilitated by GO from dye molecules to metal oxide photocatalysts. (d) Statistical data for the number of publications on metal oxide-based GO nanocomposite for various applications. (e) Photocatalytic degradation of MB using GO/ZnO nanocomposite. Reproduced with permission from ref. 163 Copyright (2024), Elsevier. (f) Degradation of MO and (g) RhB dyes by ZnO and rGO/ZnO composite. (h) Evaluation of TOC removal during the degradation of MO and RhB by rGO/ZnO nanocomposites. (i) Investigation of the impact of initial pH on the photocatalytic degradation of MO and RhB. Reproduced with permission from ref. 164 Copyright (2022), Elsevier.

This journal is © The Royal Society of Chemistry 2025

Catal. Sci. Technol., 2025, **15**, 1702–1770 | **1715**

3.2. GO as a co-catalyst with metal oxide photocatalysts

Semiconductors have been used as model catalysts in photocatalysis due to their simplicity, affordability, high stability, nontoxicity, and suitable band positions.[20,152–155] However, the photocatalytic performance of semiconductors remains below the level required for practical applications due to the rapid recombination of photoexcited electron–hole pairs, leading to a low quantum efficiency and limited photocatalytic activity. Numerous modifications have been implemented on these photocatalysts to narrow their bandgap and reduce charge recombination.[156–159] Notably, when GO is combined with these semiconductor photocatalysts to create nanocomposites, it aids in preventing the recombination of photogenerated charge carriers by effectively separating the photogenerated e^- and h^+.[129,160] The overall mechanism of GO as a charge carrier or electron transporter in GO–metal oxide nanocomposites is depicted schematically in Fig. 6(a and b) and described through the associated reactions. When exposed to visible light, GO–metal oxide is excited, causing photogenerated e^- to transfer from the VB of the metal oxide semiconductor to its CB. In this process, GO acts as an e^- trap, facilitating the transport of these photoexcited electrons and preventing their recombination with photogenerated h^+ in the VB. Subsequently, the electrons transported by GO interact with surface O_2, leading to the generation of ROS such as $\cdot O_2^-$ radicals. Meanwhile, the photogenerated h^+ in the VB of the metal oxide semiconductors react with H_2O to form $\cdot OH$ radicals, which are another type of ROS. These ROS subsequently degrade the dye adsorbed on surface of the nanocomposite.[161] Additionally, an alternative mechanism, as illustrated in Fig. 6(c), explains the higher photocatalytic dye degradation in GO–metal oxide nanocomposites through the efficient charge transfer facilitated by GO. GO helps transfer charges from dye molecules to metal oxide photocatalysts, improving the overall efficiency of the photocatalytic process.[162] Fig. 6(d) shows the statistical data for the number of publications on metal oxide-based GO nanocomposites for various applications.

This enhanced performance is due to the unique structure of GO, which easily hybridizes with these photocatalysts and provides a pathway for efficient separation and migration of e^-. The fabrication of composite materials incorporating GO leads to an increase in both light absorption and the surface area of the materials. GO can inhibit corrosion and reduce the release of metal oxide NPs into water, while also minimizing the recombination of e^- and h^+. These characteristics contribute to extending the photocatalytic lifetime of materials with incorporated GO. By providing a protective barrier and enhancing the charge separation, GO plays a key role in improving the stability and durability of photocatalytic systems. The use of GO as a supporting material in combination with various other semiconductors to create stable, recyclable, and efficient photocatalysts has become a challenging and active area of research. Several research groups have explored the fabrication of GO-based semiconductor materials to significantly enhance their photocatalytic activities. By coupling GO with various materials, researchers have been able to design type-II heterojunctions or Z-scheme photocatalysts. These materials include TiO_2,[165] ZnO,[166] CuO,[167] CdO,[168] SnO_2,[169] and WO_3.[170] These combinations have shown promise in improving the overall efficiency and performance of photocatalysts. In the context of the photocatalytic degradation of organic dye molecules using GO–metal oxide semiconductor nanocomposites, GO plays a vital role in enhancing the efficiency of nanocomposites by offering the strong adsorption of dye molecules.[99,171] Over the past two decades, researchers have invested significant efforts to developing photocatalytic processes for the photo-oxidation of organic dyes using GO-based ZnO nanocomposites. The formation of heterostructures such as GO/ZnO and reduced GO–ZnO appears to decrease the recombination losses and extend the light response of the materials to include visible light. This expansion of the light response range improves the overall photocatalytic performance, particularly in treatment of pollutants under visible light.[172]

Deepthi *et al.*[173] synthesized GO/ZnO composite films using the sol–gel spin coating method. These composite films demonstrated a 1.3-fold improvement in photocatalytic degradation compared to bare ZnO, removing 89% of MB in 150 min. The proposed mechanism for degradation involved the action of hydroxyl and $\cdot O_2^-$ radicals. The composite films also showed stability through four cycles of reuse, maintaining consistent photocatalytic activity. To further illustrate the effectiveness of the films, the researchers subjected phenol and mixtures of dyes to photocatalytic degradation. The GO/ZnO composite successfully degraded 72% of phenol within 150 min, showcasing its potential as an efficient and stable photocatalyst for various organic pollutants. Al-Zahrani *et al.*[174] synthesized a GO/ZnO nanohybrid using a solvent-free solid-state method. The synthesized nanohybrid exhibited a band gap of 2.5 eV, which is beneficial for enhancing its photocatalytic activity. This nanohybrid was employed as a photocatalyst to efficiently degrade MB under visible light-induced photoreaction. The GO/ZnO nanohybrid demonstrated an outstanding performance, achieving a decomposition rate of 98.4% for MB within a 22 min timeframe. The rate constant was calculated to be 0.1343 min^{-1}, which was significantly higher than that of bare ZnO of 0.0448 min^{-1}. Fig. 6(e) depicts the efficient photocatalytic degradation of MB by the GO/ZnO nanocomposite. GO plays a crucial role in the photocatalytic process by aiding in the collection and transport of electrons. This enhancement led to the generation of ROS and $\cdot OH$ radicals, which effectively broke down MB. The scavenger test results supported the conclusion that the primary cause of MB degradation was the presence of $\cdot OH$ radicals, which were identified as the most active species in this process.

1716 | *Catal. Sci. Technol.*, 2025, **15**, 1702–1770

This journal is © The Royal Society of Chemistry 2025

Recently, Verma and coworkers[175] prepared a GO/ZnO nanocomposite using an eco-friendly one-pot method. This nanocomposite was applied for the photocatalytic degradation of aqueous solutions containing malachite green (MG), crystal violet (CV), and a mixture of these two dyes (CV + MG). The degradation of MG and CV dyes was observed to be 77.46% and 33%, respectively, in 180 min. The GO/ZnO nanocomposite showed significantly enhanced photocatalytic degradation of the dye mixture, achieving a degradation rate of 96.72%. Although MG and CV dyes share similar molecular structures, they exhibit different removal mechanisms. In the case of MG, adsorption played a key role in the degradation process, while for CV, the degradation process involved the initial destruction of the aromatic rings. In addition to its photocatalytic properties, the nanocomposite demonstrated enhanced antibacterial activity against various strains, including *S. aureus*, *E. faecalis*, *E. coli*, and *Citrobacter* sp. The proposed antibacterial mechanism involved lipid peroxidation, oxidative stress, proteolysis, ROS induction, and cell membrane lysis, providing a comprehensive approach to combating bacterial infections. Similarly, Elumalai et al.[164] reported the photocatalytic degradation of MO and RhB by ZnO and rGO/ZnO, as shown in Fig. 6(f and g), which reveals that rGO/ZnO showed better results compared to bare ZnO. Fig. 6(h and i) depicts the total organic carbon TOC removal percentage and impact of the initial pH of the solution towards the photodegradation of dyes.

In a related study, Sayem et al.[176] prepared GO/ZnO nanocomposites using an ultrasonication method, achieving a reduced band gap of 2.67 eV. The GO/ZnO catalyst demonstrated exceptional degradation efficiency (97.7%) within just 85 min, owing to its effective adsorption and visible-light-driven photocatalytic activity in the degradation of RhB dye. The visible-light-driven photocatalytic activity was approximately nine-times faster compared to the unmodified ZnO catalysts. The scavenger tests strongly indicated that $\cdot O_2^-$ radicals played a key role in the RhB dye degradation process by the GO–ZnO nanocomposites. The reusability studies of the GO–ZnO catalyst showed a degradation efficiency of over 91% across four consecutive cycles, while retaining its crystal structure, highlighting its stability and potential for repeated use. Alshammari et al.[177] synthesized ZnO-decorated GO nanosheets with a band gap of 2.9 eV. The GO/ZnO nanohybrid was employed for water treatment applications, demonstrating synergistic photocatalytic activity that outperformed bare GO and ZnO. The nanocomposite achieved an impressive MB degradation efficiency of approximately 98% within 180 min. This significant improvement highlights the potential of the GO/ZnO nanohybrid as an effective photocatalyst for water treatment and pollutant degradation.

Sharma et al.[178] synthesized an eco-friendly and solar light-responsive GO-wrapped zinc oxide nanohybrid using lemon and honey as chelating and complexing agents. The photocatalytic activity of the synthesized nanohybrid was tested through the degradation of hazardous organic textile dye and wastewater under natural solar light. The nanohybrid displayed excellent photocatalytic activity, achieving approximately 89% degradation of MB. In addition to decolorization, around 71% of mineralization was also accomplished. Moreover, the physicochemical parameters of the wastewater from the textile industry were monitored both before and after exposure to the nanohybrid. The results indicated significant reductions in chemical oxygen demand (COD) by 96.33%, biochemical oxygen demand (BOD) by 96.23%, and total dissolved solids (TDS) by 20.85%. These findings suggest the potential applicability of the nanohybrid in textile wastewater treatment and its efficacy in improving water quality.

Besides TiO_2 and ZnO, other metal oxides such as WO_3, Fe_2O_3, CuO, and SnO_2 are regarded as non-toxic photocatalysts for pollutant removal due to their affordability, quick response, and recovery times. For instance, Sehar et al.[179] synthesized a GO–CuO nanohybrid using a fast, cost-effective, and simple solvothermal method. This nanohybrid was employed in the photocatalytic degradation of methylene red (MR) dye. Their study examined the effects of varying the H_2O_2, photocatalyst, and dye concentrations over time on the degradation process. Impressively, the GO–CuO nanohybrid achieved approximately 94% degradation of MR with up to six times recyclability, demonstrating its efficiency and reusability as a photocatalyst. NPs as carriers significantly enhance the effectiveness of targeted drug delivery, making them valuable in treating serious conditions such as cancer and diabetes. Inspired by this advancement, Ganesan et al.[180] synthesized copper oxide NPs (CuO-NPs) using *Acalypha indica* leaf extract, and then combined them with GO to create GO–CuO nanocomposites. The photocatalytic studies demonstrated that the synthesized nanocomposites effectively degraded MB dye by 83.20% and exhibited 70% cytotoxic activity against HCT-116 human colon cancer cell lines at a concentration of 100 μg mL^{-1}. The GO–CuO nanocomposites showed a promising performance in terms of both anticancer activity and photocatalytic efficiency, outperforming the individual NPs. Likewise, Sagadevan et al.[181] prepared CuO NPs decorated with rGO nanosheets using an efficient synthetic route. The nanocomposite exhibited high photocatalytic efficiency, achieving a degradation rate of 95.6% for CR and 77.5% for MB under visible light exposure within one hour.

Ahmed et al.[182] synthesized a reduced rGO and tungsten trioxide (WO_3) composite using a precisely controlled hydrothermal method. This rGO/WO_3 composite was proven to be highly effective in the photocatalytic degradation of MB and RhB dyes under sunlight. The composite successfully degraded RhB dye by up to 85%, while MB dye experienced a lower degradation rate of 32%. The higher degradation efficiency for RhB was attributed to its greater molecular electrostatic potential compared to MB dye. This difference in potential allowed O_2^- and $\cdot$OH radicals to interact more strongly with RhB dye, leading to its superior degradation.

This journal is © The Royal Society of Chemistry 2025

Catal. Sci. Technol., 2025, **15**, 1702–1770 | **1717**

Kodarkar *et al.*[183] prepared an rGO and WO_3 nanocomposite using an ultrasound-assisted method. The intense environment generated by the ultrasound process effectively reduced the particle size of WO_3 deposited on GO nanosheets. This rGO/WO_3 nanocomposite exhibited an impressive photocatalytic degradation efficiency of 81.56% for MB dye. Additionally, the nanocomposite photocatalyst was used to examine the degradation rates of various dyes, which revealed that the degradation efficiency followed the order of CV > MB > brilliant green (BG).

The uniqueness of GO-based composites are not only employed in photocatalytic but also in photoelectrochemical applications. Metal oxide nanostructures are commonly used to decorate graphene sheets to enhance their performance, given that the synergistic effect between graphene and metal/metal oxides significantly boosts their individual properties, thereby improving their photoelectrochemical (PEC) water splitting performance. For instance, Mollaei *et al.*[184] synthesized zinc oxide nanotube arrays hybridized with rGO (rGO/ZnO NTs) on fluorine-doped tin oxide substrates using an electrodeposition technique to evaluate their PEC water splitting efficiency under visible light. The rGO/ZnO NT photoanode demonstrated a high photocurrent density of 0.441 mA cm^{-2} at 1.8 V. The significant enhancement in PEC performance was attributed to the role of rGO in the efficient charge separation and effective electron transfer. Additionally, the presence of rGO increased the carrier density, light absorption capacity, and reduced charge transfer resistance and charge recombination rate. Quiroz-Cardoso *et al.*[185] studied cadmium sulfide (CdS) semiconductors modified with GO and nickel (Ni) to evaluate the potential increase in photoactivity. Pure CdS semiconductors typically have poor efficiency due to their fast recombination of electron–hole pairs, but modification with graphene can minimize this recombination. The oxygen functional groups on the surface of GO nanosheets allow their further modification through the integration of additional semiconductors. In a sacrificial reagent ethanol solution, the composite Ni/GO–CdS exhibited high photocatalytic activity, increasing the H_2 production to 8866 μmol g^{-1} h^{-1}, which was 6.3 times that of bare CdS. Similarly, Zhang *et al.*[186] reported the preparation of a novel metal-free rGO–$Zn_xCd_{1-x}S$ nanocomposite *via* a facile coprecipitation-hydrothermal reduction strategy. The optimized RGO–$Zn_{0.8}$-$Cd_{0.2}S$ photocatalyst exhibited a high H_2 production rate of 1824 μmol h^{-1} g^{-1} at an RGO content of 0.25 wt%, with an apparent quantum efficiency of 23.4% at 420 nm. This work further demonstrates that RGO is a promising substitute for noble metals in photocatalytic H_2 production.

The reduction of CO_2 to various carbon fuels can efficiently address environmental issues and the energy crisis. The photocatalytic degradation of CO_2 offers a unique solution by directly converting solar energy into chemical energy, a process popularly known as "artificial photosynthesis". Platinum is the most extensively employed co-catalyst for enhancing CO_2 photoreduction. Meanwhile,

graphene samples, including GO and rGO, are recognized as effective co-catalysts for semiconductors due to their high electron mobility, 2D structure, large surface area, and excellent chemical stability. These features make GO a tremendous metal-free co-catalyst alternative to the costly noble metal platinum.[187] Hossain *et al.*[188] synthesized rGO/CuNP nanocomposites on Cu foil with various proportions using a facile electrochemical reduction method, controlling the concentration of Cu and GO precursors. To evaluate the electrocatalytic activity of the rGO/Cu nanocomposite for the electrochemical reduction of CO_2, linear sweep voltammetry (LSV) and electrochemical impedance spectroscopy were performed and the results compared with that of bare Cu substrate, Cu NPs, and rGO. The rGO/Cu nanocomposite exhibited a much higher current density and lower onset potential compared to the other electrodes. Additionally, it demonstrated the lowest charge-transfer resistance (355.40 Ω cm^{-2}). The electrode was found to be highly stable during electrolysis. The superior electrocatalytic activity and stability of the rGO/Cu nanocomposites for the electrochemical reduction of CO_2 were attributed to the uniformly distributed small Cu NPs on the rGO and their synergistic coupling effect. In another study, Yu *et al.*[189] prepared GO/CdS nanorod composites using a one-step microwave-hydrothermal method in an ethanolamine-water solution. These composite samples demonstrated high activity for the photocatalytic reduction of CO_2 to CH_4, even in the absence of a noble metal Pt co-catalyst. The optimized rGO/CdS nanorod composite photocatalyst achieved a remarkable CH_4 production rate of 2.51 μmol h^{-1} g^{-1} at an rGO content of 0.5 wt%. This rate was over 10 times greater than that of pure CdS nanorods and surpassed that of an optimized Pt–CdS nanorod composite photocatalyst under the same conditions. The enhanced photocatalytic activity was attributed to the deposition of CdS nanorods on the rGO sheets, which functioned as electron acceptors and transporters, effectively separating the photogenerated charge carriers. Additionally, the incorporation of rGO improved the adsorption and activation of CO_2 molecules, facilitating the photocatalytic reduction of CO_2 to CH_4.

The diversity in metal oxides presents unique benefits and challenges in their use as photocatalysts. By combining different metal oxides, these limitations can often be mitigated, leading to an improved overall photocatalytic performance. The discussion above illustrates how GO serves not only as a co-catalyst but also as an efficient standalone photocatalyst. It is capable of enhancing the photocatalytic efficiency through its unique structural properties and ability to facilitate charge transfer. In addition, GO-based photocatalysts have shown promising results in the photodegradation of organic dye pollutants. The roles of GO in these photocatalytic processes and notable achievements in dye degradation are summarized in the table below.

In summary, the versatility and adaptability of GO in various photocatalytic applications make it a promising material for application as both a co-catalyst and sole
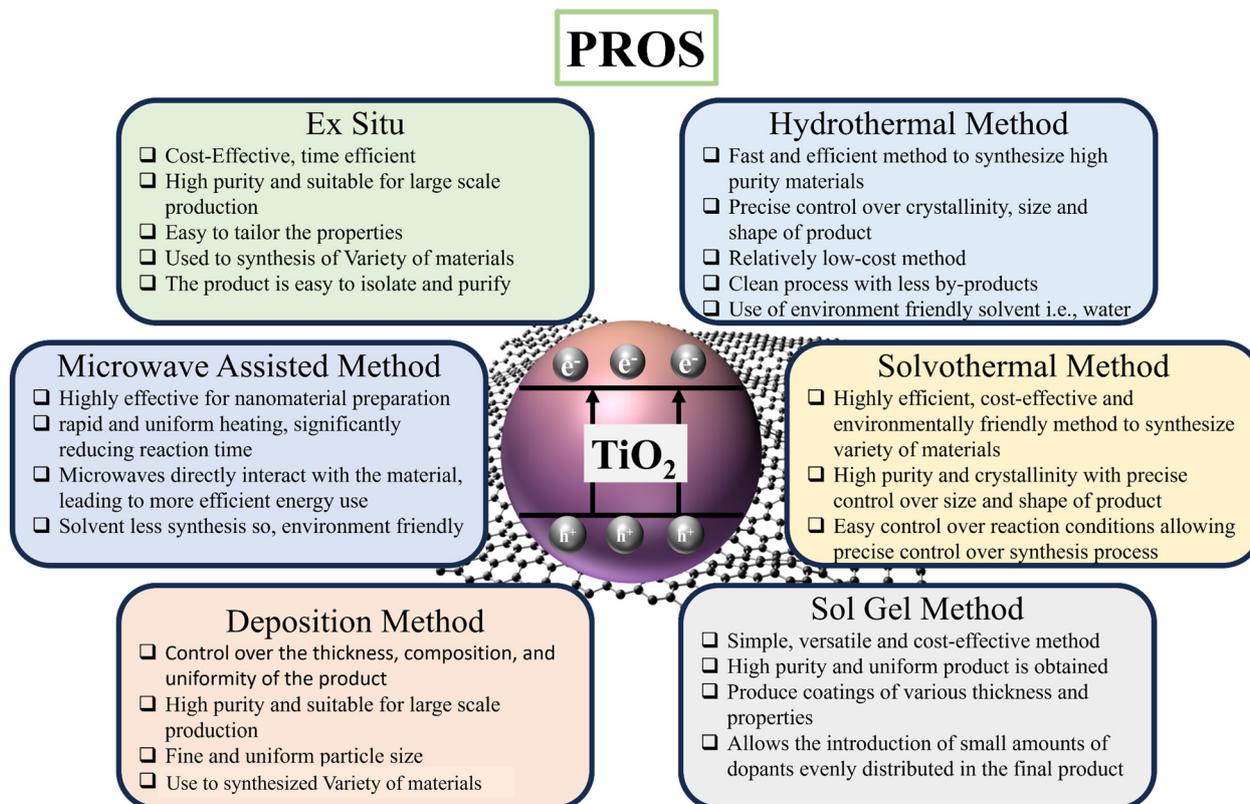
1718 | *Catal. Sci. Technol.*, 2025, **15**, 1702–1770

This journal is © The Royal Society of Chemistry 2025

Fig. 7 Advantages of various methods for the synthesis of GO/TiO$_2$ nanocomposites.

catalyst. The ability of GO to enhance the photodegradation efficiency in different systems underscores its potential in the field of environmental remediation. In the next sections, the synergistic effect of GO with TiO$_2$ is explained in detail along with the synthesis methods, photocatalysis mechanism, and multifunctional photocatalysis applications of GO/TiO$_2$ in various fields of environmental remediation and energy.

4. Synthesis of GO/TiO$_2$ nanocomposites

Current research on the fabrication of GO/TiO$_2$ systems highlights various specialized synthetic strategies aimed at engineering their crystal size, shape, morphology, and controlled exposed crystal facets to enhance their photocatalytic performance.[29] GO/TiO$_2$ nanocomposites are typically synthesized using two main techniques, *i.e.*, *in situ* crystallization and *ex situ* hybridization.[190] To achieve the desired properties of GO/TiO$_2$ for optimal photocatalytic applications, the synthesis of GO/TiO$_2$ systems is further discussed in this section. Fig. 7 shows the advantages of the method used to synthesize GO/TiO$_2$ nanocomposites.

4.1. *Ex situ* hybridization

The *ex situ* hybridization process involves mixing GO dispersions with pre-synthesized TiO$_2$ NPs. To enhance the

quality of the GO/TiO$_2$ nanocomposites, TiO$_2$ NPs and graphene sheets are pre-functionalized through carbon–carbon coupling (covalent) or π–π stacking reactions (non-covalent).[191] Ramesh Raliya *et al.*[192] prepared a composite by mixing GO with TiO$_2$ at varying concentration ratios and its effects on their photocatalytic performance were evaluated. Similarly, Morawski *et al.*[193] developed a visible light-active rGO/TiO$_2$ photocatalyst by mechanically blending TiO$_2$ with a specific mass ratio of reduced GO in 1-butyl alcohol, followed by ultrasonication. Gao *et al.*[194] prepared GO/TiO$_2$ nanocomposites by mixing TiO$_2$ NPs with a GO dispersion in water, then sonicating, stirring, centrifuging, and vacuum drying to produce the final nanocomposites. The improvement in photocatalytic activity was attributed to the increased light absorption and effective electron–hole charge separation resulting from the mixing process. However, with *ex situ* hybridization, it is sometimes possible to obtain a low-density and non-uniform coverage of nanostructures on GO sheets.[195–197]

4.2. *In situ* crystallization

The most widely used method for synthesizing GO/TiO$_2$ nanocomposites is *in situ* crystallization. In this process, GO or rGO is commonly employed as the starting material because the oxygen-containing functional groups on their surface serve as nucleation sites for the growth and attachment of semiconductor nanocrystals. Various methods can be applied

to fabricate GO/TiO$_2$ nanocrystals, including mixing, sol–gel, electrochemical deposition, hydrothermal and solvothermal methods, microwave irradiation, photo-assisted reduction, combustion, and self-assembly approaches.

4.2.1 Hydrothermal method. The hydrothermal/solvothermal technique is another simple but mature synthesis method widely accepted for developing hybrid photocatalysts,

which involves growing crystals from an aqueous solution in an autoclave under high temperature and pressure. The low boiling point of water enables it to be used under high pressure, making it a safer and more cost-effective alternative to high-boiling solvents such as DMSO, which can be expensive and hazardous. The elevated temperature in hydrothermal synthesis facilitates the formation of fine crystals of the desired
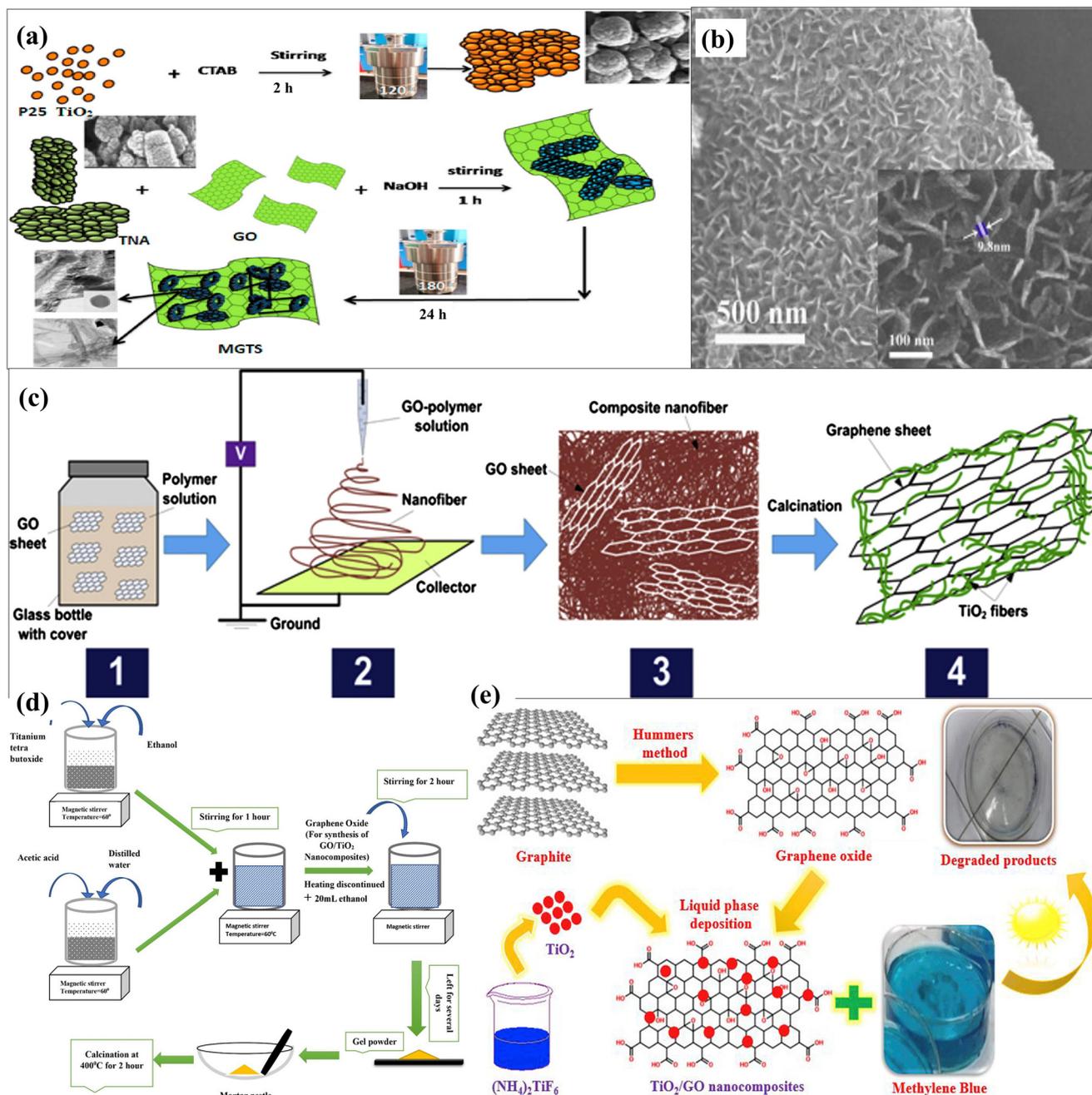
Fig. 8 (a) Schematic of the hydrothermal synthesis route for GO/TiO$_2$ nanocomposite. Reproduced with permission from ref. 205 Copyright (2019), Elsevier. (b) High-magnification SEM image of ultrathin 2D carbon-self-coated TiO$_2$ on rGO. Reproduced with permission from ref. 206 Copyright (2015), Elsevier. (c) Schematic of the fabrication of TiO$_2$ nanofibers decorated with rGO sheets *via* electrospinning (steps 1–4). Reproduced with permission from ref. 207 Copyright (2015), Elsevier. (d) Schematic of the process for the synthesis of GO/TiO$_2$ nanocomposites *via* sol–gel method. Reproduced with permission from ref. 208 Copyright (2022), Springer Nature. (e) Deposition method for the synthesis of GO/TiO$_2$ nanocomposite. Reproduced with permission from ref. 209 Copyright (2019), Elsevier.

1720 | Catal. Sci. Technol., 2025, 15, 1702–1770

This journal is © The Royal Society of Chemistry 2025

nanocomposites. This technique allows precise control of the composition and consistency of the produced nanocrystals. The physicochemical properties and morphology of the crystals are highly dependent on the hydrothermal conditions such as temperature, duration, precursors used, and cooling time. The high pressure at elevated temperatures during hydrothermal treatment ensures good interaction between precursors.[198]

Several researchers have explored the use of the hydrothermal technique for preparing GO nanostructured materials.[199] This method typically employs organic molecules as precursors in an alkaline medium. Although the hydrothermal technique is regarded as economical and eco-friendly, it generally requires high temperatures. For instance, Ruidíaz-Martinez et al.[200] hydrothermally synthesized an rGO/TiO$_2$ nanocomposite for the photocatalytic degradation of ethylparaben. Titanium isopropoxide and triethanolamine were used as TiO$_2$ precursors and mixed to obtain a Ti(IV) solution. The rGO/TiO$_2$ composites were created by adding different amounts of GO dispersion to a water (1:14) mixture under continuous agitation. Subsequently, the Ti(IV) solution was added, and the mixture was agitated at room temperature to obtain a homogeneous solution, which was then placed in a Teflon vessel within a stainless steel reactor. Similarly, Manikandan et al.[201] synthesized a multidimensional self-assembled hierarchical structure of rGO/TiO$_2$ composites using a two-step hydrothermal method, as shown in Fig. 8(a). They first prepared TiO$_2$ aggregates using P25 NPs and cetyltrimethylammonium bromide at 120 °C for 6 h, followed by treating GO/TiO$_2$ nano aggregates at 180 °C for 24 h. Shen et al.[202] applied a green and efficient method to prepare a GO/TiO$_2$ nanohybrid via a one-step hydrothermal process, using glucose as the reducing agent. The results demonstrated its effective reduction. Nawaz et al.[203] evaluated the synthesis of GO/TiO$_2$ using the hydrothermal method for the photodegradation of carbamazepine. It was observed that the GO/TiO$_2$ nanostructured material exhibited a higher rate of adsorption and photodegradation than TiO$_2$ alone, achieving over 99% carbamazepine removal within 90 min. Najafi et al.[204] studied the effect of TiO$_2$ morphology on the structure of GO/TiO$_2$ nanocomposites synthesized via a one-step hydrothermal method. GO/TiO$_2$ nanocomposites with different TiO$_2$ morphologies were fabricated using this straightforward technique. Specifically, GO/TiO$_2$ nanowires were prepared by combining titanium nanowires (NWs) and a GO aqueous suspension as the starting materials. In a typical preparation process, titanium NWs were added to ethanol and the GO suspension. Subsequently, the resulting solution was transferred to a Teflon-sealed autoclave for hydrothermal treatment. The GO/TiO$_2$ NWs demonstrated better photocatalytic degradation of MB compared to GO/TiO$_2$ NPs.

4.2.2 Solvothermal method. In recent years, the solvothermal method has garnered significant attention for fabricating GO/TiO$_2$. This technique involves the preparation of various NPs using non-aqueous media at high pressure and temperature. Unlike the hydrothermal method, which uses water as the solvent, the solvothermal method employs organic solvents, which typically have a more pronounced effect on the size, shape, distribution, and crystallinity of the prepared NPs.[210] The solvothermal method is a simple and highly efficient way to synthesize GO/TiO$_2$. It can be classified into two categories, i.e., synthesis in alkaline media and synthesis in the presence of organic molecule precursors.[211] This synthesis route is considered innovative, given that there are relatively few published papers on the production of GO using this method. The solvothermal approach for producing GO has several advantages, including being non-toxic, cost-effective, and generating almost no by-products during the reaction process.[212]

Recently, Ayala et al.[213] synthesized an rGO/TiO$_2$ nanocomposite via the solvothermal technique for potential use in photoelectrocatalytic processes. GO was added to a mixture of water and ethanol and sonicated for 30 min. Then, TiO$_2$ was added, and the resulting solution was placed in a Teflon-lined autoclave at 180 °C for 18 h. The synthesized composite had a band gap of 2.86 eV. Li et al.[214] synthesized rGO/TiO$_2$ composites with a sandwich-like structure using a simple solvothermal method. Similarly, Yadav et al.[215] synthesized GO/anatase TiO$_2$ nanocomposites using a simple solvothermal method. Briefly, anatase TiO$_2$ NPs were added to a solution of GO aqueous suspension and ethanol. This reaction mixture was sonicated to exfoliate GO, and then transferred to a Teflon-lined autoclave and maintained at 130 °C for 4 h in an electric oven. The photocatalytic performance of the prepared nanocomposites was evaluated by the degradation of gaseous benzene under UV light irradiation. The GO/anatase TiO$_2$ nanocomposites exhibited a better photocatalytic performance than pure TiO$_2$ NPs. In the procedure described by Jiang et al.,[206] a facile one-pot solvothermal method was used to successfully prepare novel carbon self-coated rGO/TiO$_2$ nanohybrids. Fig. 8(b) shows an SEM image of a synthesized carbon-coated rGO/TiO$_2$ nanohybrid.

4.2.3 Sol–gel method. This simple and inexpensive wet-chemical method is used to prepare composite materials with excellent control of their size. In this technique, the solution (sol) gradually evolves towards the production of a gel-like formation consisting of solid and liquid phases. There are two categories of sol–gel techniques, i.e., aqueous and non-aqueous sol–gel synthesis.[216] The sol–gel technique can be used to achieve optimal chemical interaction and vigorous mixing between GO and TiO$_2$. This process transforms the liquid precursor into a sol, which gradually forms into a gel-like network structure. It involves the hydrolysis of a TiO$_2$ precursor (commonly titanium alkoxide), followed by condensation in the presence of graphene and GO. The overall process does not require elevated temperature or pressure and is preferred for its controllability, reliability, and economic cost.[217] The dispersion between TiO$_2$ and GO provides relatively stable oxo- and hydroxo-bonds between the two materials, eventually leading to the formation of a

This journal is © The Royal Society of Chemistry 2025

Catal. Sci. Technol., 2025, **15**, 1702–1770 | **1721**

sol, and then gel-like networks upon the further addition of GO. Then, the prepared gel is dried and calcined.[210]

Štengl et al.[218] prepared GO/TiO$_2$ nanocomposites with varying GO contents using a one-step sol–gel method, employing TiO$_2$ peroxo-complexes as the precursor. NaOH and hydrogen peroxide were used to hydrolyze titanium oxysulfate (TiOSO$_4$) to produce the TiO$_2$ peroxo-complex. Velasco-Hernández et al.[219] synthesized GO/TiO$_2$ nanocomposite thin films on glass substrates using the sol–gel route and dip coating technique for photocatalytic applications. The energy band gap of the thin films after annealing at 450 °C was estimated to be in the range of 3.38–3.45 eV. These thin films demonstrated enhanced activity for the photocatalytic degradation of MB and high efficiency in CO$_2$ photoreduction. Kumar et al.[208] prepared GO/TiO$_2$ nanocomposites for room temperature gas sensing applications using the sol–gel technique, as shown in Fig. 8(d). They synthesized pristine TiO$_2$ and GO/TiO$_2$ nanocomposites by mixing titanium tetrabutoxide (Ti(OC$_4$H$_9$)$_4$) and ethanol in a 1:4 ratio and magnetically stirred the solution. Then, a mixture of distilled water and acetic acid was added and stirred for 1 h while heating. After heating, ethanol was added, and the solution was stirred for another 2 h. Then, the solution was left at room temperature for about 7 days until a gel powder was formed. The dried gel powder was ground, and then calcined to obtain pristine TiO$_2$. To prepare GO/TiO$_2$ nanocomposites with different weight percentages of GO, an appropriate amount of GO was added to the process. The GO/TiO$_2$ nanocomposite with 7 wt% of GO demonstrated the highest response percentage of 18.66% at 200 ppm. Additionally, this composite exhibited the lowest response time of 80 s. Ma et al.[220] used GO and tetrabutyl titanate as precursors to synthesize GO/TiO$_2$ nanocomposites and found that their photocatalytic activity was influenced by both the GO content and calcination atmosphere.

4.2.4 Deposition method. Deposition techniques offer the benefits of a straightforward experimental method and the formation of nanocomposites at comparatively low temperatures. For instance, Ming-Zheng Ge et al.[221] employed both electrodeposition and carbonation methods to deposit rGO films on TiO$_2$ nanotubes, which were produced through a two-step electrochemical anodization process. Athanasekou et al.[222] utilized the dip-coating process to deposit GO/TiO$_2$ nanocomposites on the surface of ceramic membranes, including γ-alumina and silica single-channel nanofiltration membranes. This hybrid photocatalytic/ultrafiltration system showed improved pollutant removal efficiency compared to the reference membrane prepared by the same dip-coating technique using TiO$_2$ without GO. In recent years, fabricating TiO$_2$-based nanohybrids through electrospinning has become a popular method. For instance, Pant et al.[207] employed this 4 steps simple and efficient technique to immobilize TiO$_2$ nanofibers on rGO sheets, as depicted in Fig. 8(c). They used electrospinning to fabricate TiO$_2$ precursor-containing polymeric fibers on the surface of GO sheets, followed by the simultaneous formation of TiO$_2$ nanofibers and GO reduction

through calcination. Recently, Rajoria et al.[223] synthesized GO/TiO$_2$ nanotube electrodes using a simple anodization method. The electrodeposition of GO on the TiO$_2$ surface produced GO/TiO$_2$ nanotube electrodes through anodization. GO was added to deionized water, and anodization was performed at 15 V for 15 min, followed by calcination of the synthesized GO/TiO$_2$ nanotube electrode at 300 °C for 1 h, with TiO$_2$ as the anode and stainless steel as the cathode. Al-Musawi et al.[224] synthesized a highly uniform and crystalline GO/TiO$_2$ nanocomposite using the liquid-phase deposition process. Similarly, Khan et al.[209] synthesized GO/TiO$_2$ nanocomposites by varying the amount of GO (2–8%) through a liquid deposition method, as depicted in Fig. 8(e), resulting in a highly crystalline nanocomposite with spherical morphology. Photo deposition involves the deposition of well-defined NPs on the surface of a semiconductor. The basic requirements for photo deposition include having a reduction/oxidation potential in a favorable position for efficient charge transfer, sufficient active sites on the surface, and the incident light photon energy exceeding the band-gap energy of the semiconductor.[225] Recently, Nasir et al.[226] demonstrated the photocatalytic oxidation of graphite using grey TiO$_2$ under UV light to synthesize GO/TiO$_2$ composites with adjustable properties in a single step. These composites can be directly used for visible light active photocatalysis applications under sunlight. Similarly, Ramakrishnan et al.[227] prepared GO/TiO$_2$ by reducing GO with TiO$_2$ NPs under UV light using different concentrations of rGO.

4.2.5 Microwave-assisted method. The microwave-assisted strategy in this context facilitates the synthesis of semiconductor nanomaterials with precise control of their size and shape. It is environmentally friendly, fast, and generates a homogeneous heating process. The microwave radiation technique offers several advantages, including reduced reaction times, a cleaner reaction environment, and energy savings through rapid and intense heating within the sample.[228] Recently, Rasuli et al.[229] demonstrated the preparation of rGO/TiO$_2$ by combining UV-C irradiation with the microwave technique. UV-C irradiation activates TiO$_2$ NPs, and the photogenerated electrons from these NPs are transferred to GO sheets, causing local reduction and breakdown into graphene nanosheets. In the study by Setiawan et al.,[230] the photocatalytic performance of low-grade TiO$_2$ anatase was successfully enhanced by compositing it with GO via a microwave-assisted method, which was activated by UV and Xe light. Similarly, Romeiro et al.[231] reported a one-step microwave-hydrothermal method for the preparation of rGO/TiO$_2$ nanocomposites without the use of any reducing agents. Gijare et al.[232] fabricated GO/TiO$_2$ nanocomposites using the microwave-assisted technique for application as glucose sensors. Wang et al.[233] demonstrated that reducing GO using both direct and microwave-assisted reduction in the presence of Ti powder significantly reduced the reduction time due to the microwave effect. In this process, the Ti ions generated from the reaction of Ti powder with GO were hydrolytically transferred to TiO$_2$, forming rGO/

1722 | Catal. Sci. Technol., 2025, 15, 1702–1770

This journal is © The Royal Society of Chemistry 2025

TiO_2, which was highly effective in removing MB. Yang et al.[234] prepared TiO_2 and rGO nanocomposites using a fast and simple microwave irradiation method. This involved reacting GO with commercial TiO_2 nanoparticles in a water/ethanol solvent, while exploring different microwave powers and time intervals.

5. TiO_2-graphene oxide-based nanocomposites: synergistic effect, mechanism, and multifunctional photocatalysis applications in energy and environment

Graphene has become a "star" material since it was discovered by Geim and Novoselov in 2004, and since then the manufacture and uses of this rigorous 2D material have rapidly received extensive interest.[97,98] One of the most exciting graphene applications is the synthesis of heterogeneous semiconductor/graphene hybrid photocatalysts. Heterogeneous photocatalysis is a promising and environmentally friendly method that is well-recognized in the scientific community.[235,236] In photocatalysis, graphene is also well-known as a co-catalyst, serving as an economical alternative to the expensive noble metal co-catalysts.[237] It may also be used as a photosensitizer for visible light absorption given that it is an excellent support for charge transport in conventional photocatalysts. This happens when the graphene material is the primary component that absorbs light, without influencing the bandgap of broad bandgap semiconductors such as TiO_2. The main feature is its
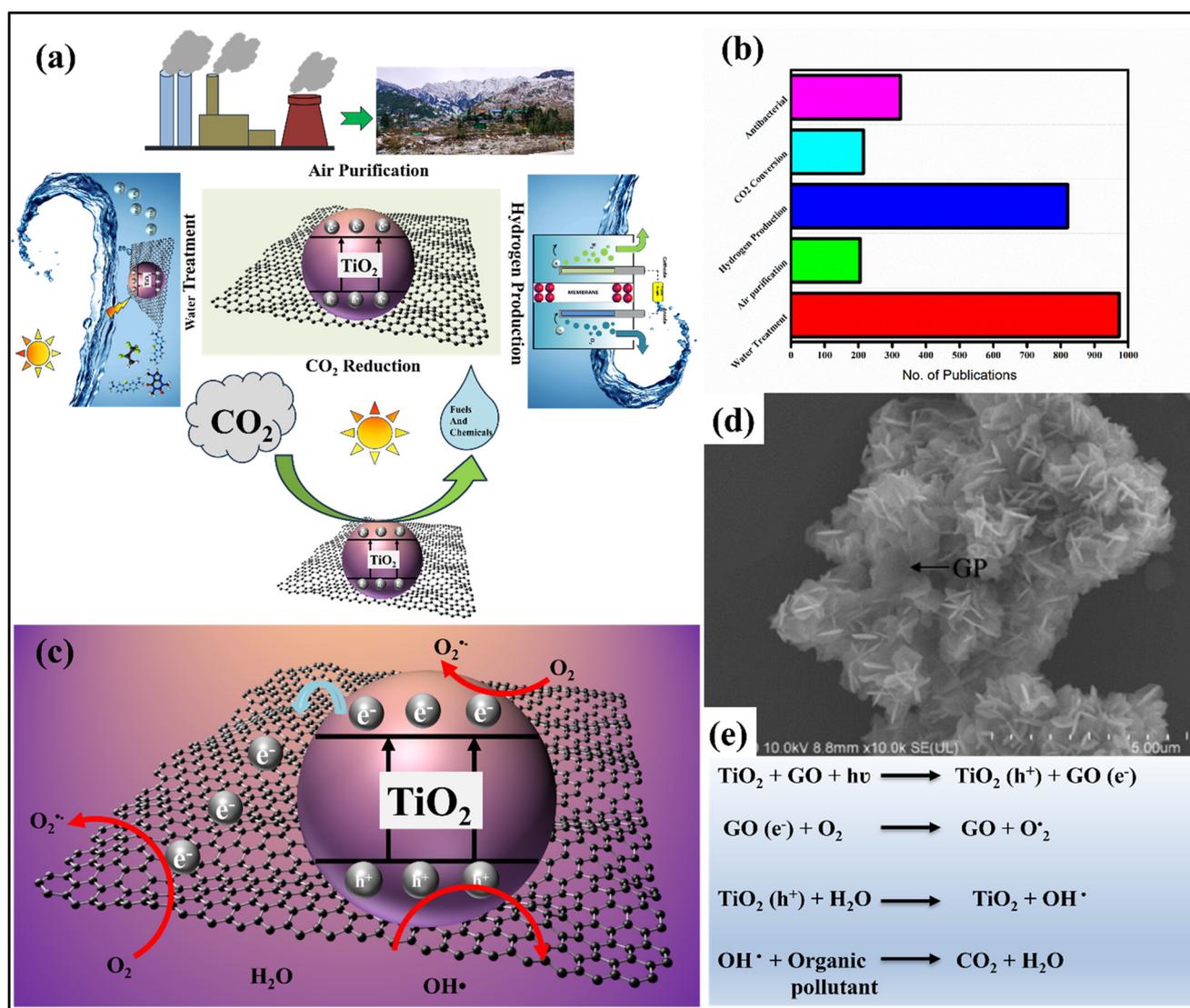
Fig. 9 (a) Schematic illustrating different photocatalytic applications of GO/TiO_2 nanocomposites. (b) Schematic of the general mechanism of GO/TiO_2 photocatalysis. (c) Number of publications on the multifunctional applications of GO/TiO_2. (d) SEM image of GO nanosheet incorporating TiO_2 NPs. Reproduced with permission from ref. 243 Copyright (2014), Elsevier. (e) Mechanism of GO/TiO_2 photocatalysis.

This journal is © The Royal Society of Chemistry 2025

Catal. Sci. Technol., 2025, **15**, 1702–1770 | **1723**

appropriate bandgap for visible light stimulation, which makes it a promising photosensitizer in heterostructure photocatalysts, resulting in enhanced photocatalytic activity.[238,239] The use of graphene as a hybrid with TiO_2 leads to an increase in the surface area of the catalyst by creating more active sites for redox processes to occur, increasing the visible-light utilization, and reducing the overall exciton recombination given that graphene accepts photogenerated electrons and contributes to high carrier transport due to its high conductivity.[240,241] TiO_2 has a higher Fermi level than graphene, and therefore electrons move from TiO_2 to graphene *via* the interface. Then, while TiO_2 contains positive charges, graphene accumulates extra negative charges, resulting in a space charge layer at the point of contact known as a Schottky junction.

The Schottky junction can behave as an electron trap, efficiently capturing electrons, and thus enhancing the photocatalysis activity. Meanwhile, the Schottky barrier functions as the primary barrier to electron transport from graphene to TiO_2. Under visible light, the electrons on the Fermi level of graphene are irradiated, and the Schottky barrier must be overcome to ensure electron injection into the TiO_2 conducting band. In the UV light irradiation process, graphene acts as an electron acceptor, promoting the separation of electron–hole pairs.[242] Fig. 9(a) shows the multifunctional applications of GO/TiO_2 nanocomposites and Fig. 9(b) displays the number of publications related to GO/TiO_2 composites in water treatment, air purification, CO_2 reduction, and H_2 production applications.

The proposed photocatalytic mechanism of GO/TiO_2 materials is depicted in Fig. 9(c) and (d) shows an SEM image of GO incorporating TiO_2. When the GO/TiO_2 nanocomposite is exposed to UV radiation, electron–hole pairs are effectively generated. The excited electrons from the CB can readily transfer to the GO sheets, allowing their free movement along the graphene network. This efficient separation of electron–hole pairs suppresses their recombination, while the enhanced separation of charge carriers boosts the generation of ROS, significantly increasing the photocatalytic performance of GO/TiO_2 hybrids.[244] The mechanism of GO/TiO_2 photooxidation, primarily through the action of photogenerated ·OH radicals, has been explored in numerous studies.[245–247] In aqueous systems, $·O_2^-$ radicals are quickly converted to hydrogen peroxide (H_2O_2), and during the photocatalytic or photolytic reaction of H_2O_2, the formation of ·OH radicals is observed. The chemical bonds between TiO_2 and GO (d–π interactions) facilitate efficient photogenerated electron transfer from the CB (d orbital) of TiO_2 to the Fermi level (π orbital) of the GO sheet. The TiO_2 CB electrons can move freely through the graphene matrix, which acts as an electron acceptor, and ultimately transfers the electrons to the surface, where they react with water and dissolved oxygen to form various ROS. These ROS, such as ·OH radicals and $·O_2^-$ radicals, possess high oxidation potential and can effectively oxidize water and organic pollutants, as shown in Fig. 9(e).[238]

Over the last decade, various heterogeneous photocatalytic applications have been investigated, including water splitting, H_2 generation, CO_2 photoreduction, organic compound degradation, and even antibiotic inactivation. GO/TiO_2 hybrids show an enhanced performance in all these applications compared to their parent materials.

5.1. Application in environmental remediation

GO is synthesized by oxidizing high-purity graphite. It has distinct characteristics from that of graphite because of the presence of several oxygen functional groups on the top layer of GO sheets. These features include fascinating optical qualities, high dispersion in various polar solvents, and the ability to connect numerous molecular structures to its surface, such as by H-bonding. These features promote the adsorption of diverse molecular structures on its surface, resulting in greater control of the size and shape of the resulting structures. In addition, the typical cost of making GO is lower than that of graphite and numerous other nanomaterials.[100,248] Rowley-Neale *et al.*[249] found that the surface area of a GO/TiO_2 composite (78.12 m^2 g^{-1}) is greater than that of bare TiO_2 (57.01 m^2 g^{-1}) utilizing the BET equation for nitrogen adsorption/desorption. The researchers demonstrated that increasing the surface area improved the pollutant adsorption performance of the GO/TiO_2 composite by roughly 37% compared to TiO_2. Thus, the contact area between the photocatalyst and contaminants is enlarged.[250] Hunge *et al.*[251] observed that TiO_2 has a bandgap of 3.11 eV, while a GO/TiO_2 composite had a bandgap of 2.72 eV. The fabrication of Ti linkages with carbon in a GO/TiO_2 composite successfully increases the bandgap of TiO_2 from the UV to visible region. The interactions of GO with TiO_2 yield intermediate states in proximity to the TiO_2 VB, allowing the modification of the prohibited band gap.[252] This also decreases the charge carrier recombination rates, while improving the photodegradation performance.

5.1.1 Photocatalytic degradation of organic pollutants in wastewater treatment. GO-based TiO_2 compounds are widely employed in light-driven dye photocatalysis in aqueous solution. Owing to their extraordinary features, GO-based oxide semiconductors increase the electron separation, which boosts photo-driven processes such as carcinogen deterioration and solar fuel (H_2) generation. Also, GO/TiO_2 photocatalysts have an enhanced specific surface area, hence enhancing their photocatalytic activity and making them promising in a variety of applications. Many studies have shown that rGO paired with TiO_2, a well-known semiconductor material, improves their efficacy in the photodegradation of CEC from water bodies.[146,253,254]

Atchudan *et al.*[255] synthesized a GO/TiO_2 nanocomposite for the effective photodegradation of MB and MO, as illustrated in Fig. 10(a). GO/TiO_2 completely degraded MB in 25 min, whereas MO was degraded in 240 min, as shown in the UV spectra in Fig. 10(b and c), respectively. Zhang *et al.*[240] reported that a GO/TiO_2 composite with 10% GO

1724 | *Catal. Sci. Technol.*, 2025, **15**, 1702–1770

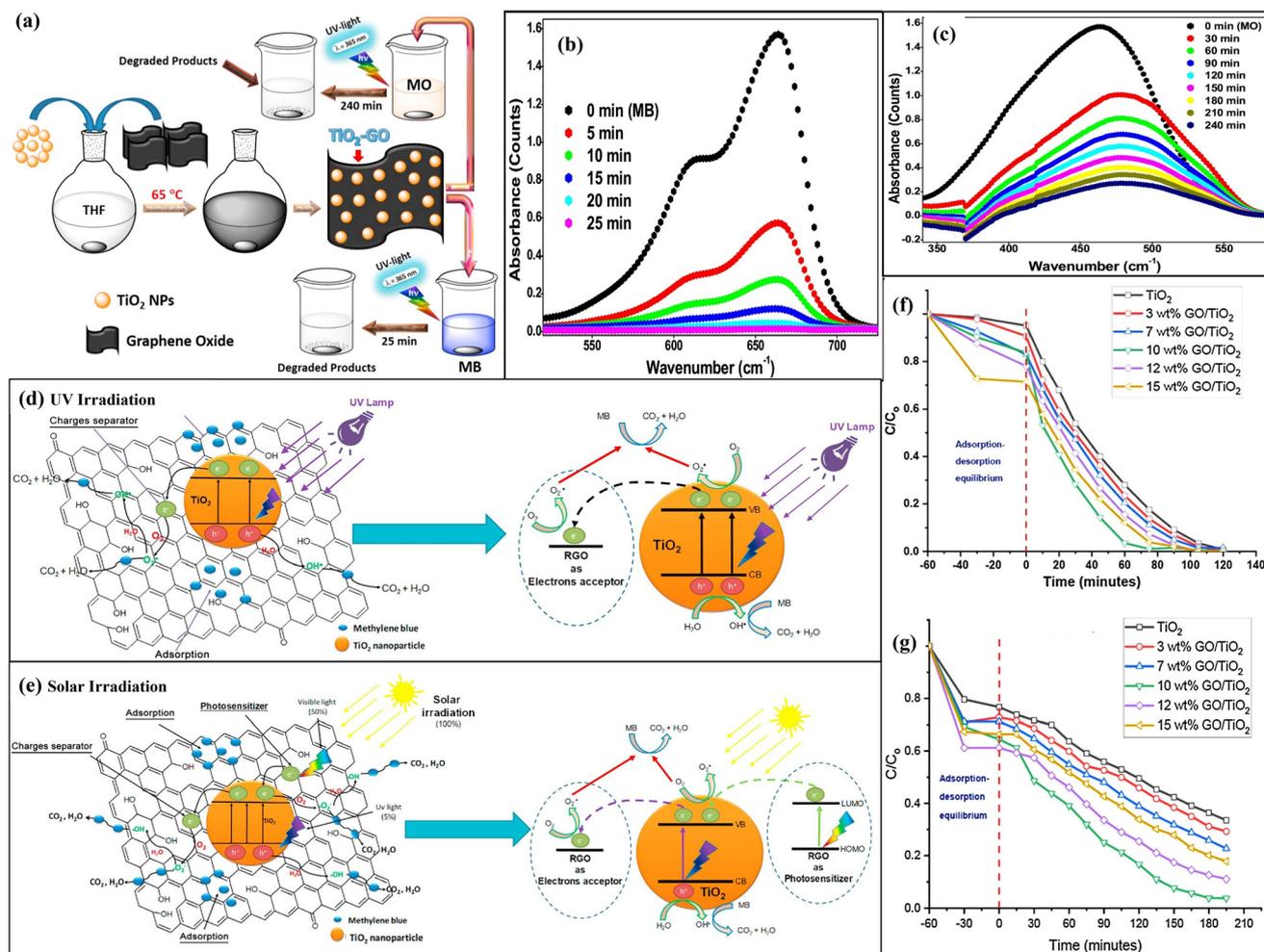This journal is © The Royal Society of Chemistry 2025

Fig. 10 (a) Schematic of the synthesis of GO/TiO$_2$ nanocomposite and the degradation process of MB and MO. Absorbance spectra of degradation of (b) MB and (c) MO. Reproduced with permission from ref. 255 Copyright (2017), Elsevier. Schematic depicting the mechanism of rGO and synergy with TiO$_2$ NPs in the photocatalytic degradation of MB under (d) UV and (e) solar irradiation. Reproduced with permission from ref. 257 Copyright (2019), Elsevier. Photodegradation using various contents of GO loaded on TiO$_2$ NPs of (f) RhB and (g) AG-25. Reproduced with permission from ref. 258 Copyright (2019), Elsevier.

content outperformed bare P25 and GO–P25 in terms of MB photodegradation under UV irradiation. This improved photocatalytic behavior was also exhibited for the breakdown of RB, which was rationalized by the greater BET surface area of the composite and stronger interaction between TiO$_2$ and GO compared to GO–P25. In fact, high stability and interaction between TiO$_2$ and GO sheets are required for efficient charge transfer and dissociation during the photocatalytic degradation. Sharma et al.[256] investigated GO/TiO$_2$ nanocomposites synthesized employing the green alga *Chlorella pyrenoidosa*. This study utilized crystal violet (CV) as its model contaminant. The research was carried out under visible light, and the photocatalytic activity of TiO$_2$ and GO/TiO$_2$ nanocomposite for CV degradation was investigated. It was found that the nanocomposite was better owing to its lower bandgap and greater dye adsorption. Pristine TiO$_2$ degraded only 43% of CV, whereas GO–TiO$_2$ degraded 63% under the same circumstances.

Liu et al.[259] treated MO with an rGO/TiO$_2$ nanohybrid before subjecting it to visible light radiation. Within just 240 min, the nanohybrid degraded over 90% of the dye. In another study, rGO/TiO$_2$ demonstrated 88% degradation effectiveness for meta chrome yellow dye (extremely poisonous and carcinogenic) in sunlight with 80% efficacy. The increased efficiency was ascribed to the formation of ·O$_2^-$ radicals, which played a crucial role in pollutant oxidation.[260] Furthermore, Garrafa-Gálvez et al.[257] investigated the photocatalytic degradation of MB using rGO/TiO$_2$ nanocomposites under both natural sunlight and UV light. The mechanism of rGO/TiO$_2$ towards the degradation of MB is shown in Fig. 10(d and e). The nanohybrid showed 100% and 85% degradation of MB in 60 min of UV and sunlight, respectively. Kusiak-Nejman et al.[244] studied the same system but employed UV-vis light with a greater UV intensity. In this case, the nanocomposite showed 91.48% MB degradation after 60 min. Adly et al.[258]

This journal is © The Royal Society of Chemistry 2025

Catal. Sci. Technol., 2025, **15**, 1702–1770 | **1725**

studied the use of GO/TiO$_2$ composites for the photocatalytic removal of RhB and acid green 25 (AG-25). RhB was eliminated within 1.25 h, while 96% of AG-25 was cleared after 3 h, as shown in the UV spectra in Fig. 10(f and g). The achieved result was attributed to increase in the GO content to optimal levels, which allowed incoming sunlight light to interact with TiO$_2$, resulting in a boost in photocatalytic activity. GO plays several essential roles in nanocomposites, including the ability to interact with organic pollutants *via* adsorption on its surface and to

Table 2 List of various GO/TiO$_2$ nanocomposites from the literature used for multifunctional application in environmental remediation

Pollutant (conc. and volume)	Catalyst amount	Light source	Irradiation time	Efficiency	Stability/reusability	Ref.
Rhodamine B (10 mg L^{-1} & 50 mL)	1.0 g L^{-1}	UV lamp	75 min	100%	4 cycles	258
Acid green 25 (40 mg L^{-1} & 50 mL)	1.0 g L^{-1}	UV lamp	180 min	96%	4 cycles	258
Methylene blue (10 mg L^{-1} & 25 mL)	10 mg	UV lamp	120 min	99.2%	4 cycles	264
Methyl orange (20 mg L^{-1} & 100 mL)	100 mg	UV lamp	240 min	84%	—	265
Acid navy blue dye	—	Mercury lamps	90 min	95%	—	266
Methylene blue (50 mL)	20 mg	UV light	25 min	100%	—	255
Methyl orange (50 mL)	20 mg	UV light	240 min	84%	—	255
Orange ME2RL dye	—	Sunlight	—	99.6%	5 cycles	267
Crystal violet	—	Sunlight	—	95%	—	268
Brilliant green	—	Sunlight	—	81%	—	268
Malachite green	—	Sunlight	—	93%	—	268
Rhodamine B	—	Sunlight	—	97%	—	268
Methylene blue (5 mg L^{-1} & 30 mL)	—	Sunlight	120 min	92.7%	5 cycles	269
Methylene blue (5 mg L^{-1} & 30 mL)	—	UV light	120 min	55.8%	5 cycles	269
Rhodamine B (5–20 ppm & 100 mL)	0.4–1.6 g L^{-1}	Visible light	120 min	99%	6 cycles	270
Methylene blue (10 mg L^{-1} and 9 mL)	4.5 mg	Artificial solar-like radiation	120 min	98.1%	—	271
Rhodamine B (10 mg L^{-1} and 9 mL)	4.5 mg	Artificial solar-like radiation	120 min	99.8%	—	271
Alizarin yellow GG	—	Sunlight	150 min	100%	—	272
Diclofenac	—	Sunlight	60 min	100%	6 cycles	273
Methyl orange (30 ppm & 50 mL)	20 mg	UV light	30 min	95%	—	274
Methyl orange (3.05 × 10^{-5} mol L^{-1} & 7.5 mL)	500 mg L^{-1}	Visible light	240 min	87.4%	—	275
Acid orange (50 mg L^{-1} & 50 mL)	500 mg L^{-1}	UV light	30 min	100%	6 cycles	224
Methyl orange (3.5 × 10^{-5} mol L^{-1} & 200 mL)	200 mg	UV light	60 min	91.9%	10 cycles	276
Clofibric acid (20 mg L^{-1} & 1000 mL)	100 mg L^{-1}	UV-A lamp	360 min	100%	—	277
Formalin (40 mg L^{-1})	180 mg	Simulated sunlight	90 min	93.8%	—	278
Carbamazepine (300 ppb & 200 mL)	10 mg L^{-1}	UV light	—	100%	—	279
Carbamazepine	200 mg L^{-1}	UV light	—	—	3 days	280
Sulfamethoxazole	200 mg L^{-1}	UV light	—	—	3 days	280
Diclofenac	200 mg L^{-1}	UV light	—	—	3 days	280
Diuron (7.5 mg L^{-1})	500 mg L^{-1}	UV light	180 min	100%	—	281
Alachlor (12.5 mg L^{-1})	500 mg L^{-1}	UV light	180 min	100%	—	281
Isoproturon (12.5 mg L^{-1})	500 mg L^{-1}	UV light	180 min	100%	—	281
Atrazine (6.25 mg L^{-1})	500 mg L^{-1}	UV light	180 min	~98%	—	281
Microcystin-LA (0.2 μM & 10 mL)	500 mg L^{-1}	Sunlight	5 min	100%	—	282
Microcystin-LA (0.2 μM & 10 mL)	500 mg L^{-1}	Visible light	120 min	88%	—	282
Sulfamethoxazole	—	Sunlight	60 min	50%	—	283
Erythromycin	—	Sunlight	60 min	86%	—	283
Clarithromycin	—	Sunlight	60 min	84%	—	283
Oxytetracycline (20 mg L^{-1} & 50 ml)	6 mg L^{-1}	Sunlight	240 min	100%	—	284
Oxytetracycline (20 mg L^{-1} & 50 mL)	6 mg L^{-1}	Visible light	240 min	90%	—	284
Diphenhydramine (100 mg L^{-1} & 7.5 mL)	1000 mg L^{-1}	UV and visible light	60 and 240 min	—	—	171
Ethyl paraben (0.3 mM & 700 mL)	700 mg L^{-1}	UV light	40 min	98.6%	—	285
Famotidine		Sunlight	45 min	90%	—	286
Risperidone (2 mg L^{-1} & 50 mL)	5 mg	Sunlight	90 min	100%	—	287
Methanol		UV and visible light	300 min	100% and 24.3%	3 cycles	288
Toluene (28 mg m^{-3})	10 mg	UV light	48 min	100%	—	289
Acetaldehyde (25 ppm)	100 mg	UV light	160 min	42%	—	290
O-Xylene (25 ppm)	100 mg	UV light	160 min	54%	—	290
Phenol (20 mg L^{-1} & 100 ml)	50 mg	Visible light	720 min	97.9%	—	291
Methyl ethyl ketone	—	Visible light	6 min	96.8%	—	292
Formaldehyde	—	UV light	540 min	72%	—	293
Methanol	—	UV light	300 min	100%	—	294
Nitrogen oxide	—	Visible light	110 min	50.4%	—	295
Nitrogen oxide	—	UV light	40 min	52.28%	—	296
Nitrogen oxide	—	Visible light	40 min	29.34%	—	296

1726 | *Catal. Sci. Technol.*, 2025, **15**, 1702–1770

This journal is © The Royal Society of Chemistry 2025

act as an e⁻ scavenger, preventing the recombination of e⁻ and h⁺ pairs in TiO₂.

In another study, Kurniawan et al.[261] effectively degraded MB using a GO/TiO₂ photocatalyst under UV irradiation. The photocatalyst eliminated the dye within 4 h, surpassing the performance of bare TiO₂, indicating a synergistic effect between GO and TiO₂. The proposed mechanism involves the absorption of photons by the pollutant under UV-vis irradiation, leading to the formation of an excited state. Subsequently, the excited MB molecules transfer electrons to the CB of TiO₂, generating positive carbon radicals. These injected electrons interact with the O₂ molecules adsorbed on the TiO₂ surface, resulting in the formation of $\cdot O_2^-$ and $\cdot OH$ ROS. Subsequently, the generated $\cdot O_2^-$ species attack the positive carbon radicals of the dyes, leading to the formation of hydroxylated oxidation by-products. Eventually, MB is degraded into biodegradable oxidation by-products, which are adsorbed onto the surface of GO. Al-Musawi et al.[262] fabricated GO/TiO₂ using the Hummers and Hoffman's method combined with the liquid phase deposition method. The resulting GO/TiO₂ composite was employed for the efficient degradation of acid orange 7 (AO7) under UV light irradiation. Complete degradation of AO7 was achieved within 30 min under the optimized conditions, including pH of 5 and nanocomposite dose of 0.5 g L⁻¹. Liang et al.[263] detailed the synthesis of TiO₂ nanocrystals through hydrolysis combined with hydrothermal treatments, leading to their uniform growth on a GO substrate. The resulting GO/TiO₂ hybrids exhibited a three-fold increase in photocatalytic activity compared to P25 TiO₂ for the degradation of RhB dye. In a separate study, Lavanya et al.[264] developed rGO-wrapped anatase/rutile mixed-phase TiO₂ nanofibers via an efficient electrospinning method. The rGO/TiO₂ composite degraded 99.2% of MO within 120 min, demonstrating enhanced activity compared to its individual components. The superior performance of the rGO/TiO₂ composite was attributed to the synergistic effect of the anatase/rutile mixed phase within a one-dimensional nanostructure, as well as the electronic interaction between TiO₂ and rGO, which facilitated improved electron transfer. These notable characteristics also minimized the charge recombination, thereby enhancing catalytic efficiency. Table 2 summarizes the literature related to GO/TiO₂ nanocomposites for the degradation of organic pollutants in wastewater.

5.1.2 Photocatalytic degradation of pesticides, pharmaceutical, personal care products, and chemicals. Pesticides, insecticides, medicines, and personal care items are examples of contaminants of emergent concern (CEC) that are difficult to degrade and remove. These pollutants enter water bodies from agricultural fields and industry, polluting freshwater, percolating through the soil, and contaminating groundwater. Thus, to address this issue, Luna-Sanguino et al.[297] synthesized an rGO/TiO₂ nanocomposite via a simple hydrothermal method. The rGO/TiO₂ photocatalysts were tested for the solar-assisted photodegradation of methomyl, pyrimethanil, isoproturon,

and alachlor pesticides on a pilot plant scale. The nanocomposite thoroughly disintegrated these pesticides, demonstrating exceptional photodegradation properties. Similarly, Appavoo and colleagues[279] synthesized GO/P25 nanocomposites using a straightforward microwave hydrothermal method. They tested the nanocomposites, which had different levels of graphene loading, for their ability to degrade carbamazepine (CBZ), a significant pharmaceutical water pollutant, under UVA irradiation. Under the optimal conditions, the GO/P25 nanocomposites achieved 100% degradation of the pharmaceutical pollutant.

Moreira et al.[280] investigated the effectiveness of GO/TiO₂ photocatalysis for the solar-driven decomposition of various organic micropollutants, human pathogen indicators, and associated genes in urban wastewater, utilizing a pilot-scale CPC photoreactor at Plataforma Solar de Almería in Spain. The GO–TiO₂ composite demonstrated excellent photocatalytic activity against pharmaceuticals such as carbamazepine, sulfamethoxazole, and diclofenac. Similarly, Cruz et al. conducted a comparison between the photocatalytic activities of TiO₂ and GO/TiO₂ composites against a mixture of four pesticides classified as priority pollutants by the European Union including diuron, alachlor, isoproturon, and atrazine. They also assessed the influence of two water matrices, ultrapure and natural water, on their photocatalytic performance. The GO/TiO₂ composite exhibited a superior performance in terms of pesticide photodegradation and total organic carbon (TOC) abatement compared to bare TiO₂, with an even more pronounced increase in natural water matrices. The GO/TiO₂ composite nearly completely degraded all the pesticides in both natural and ultrapure water within 180 min. Microcystins (MCs) are common cyanobacterial toxins found in water and freshwater. Sampaio et al.[282] investigated the photocatalytic degradation of a cyanobacterial toxin, microcystin-LA (MC-LA), in aqueous solutions under both simulated solar light and visible light irradiation. The GO/TiO₂ composite surpassed bare TiO₂, degrading all MC-LA in 5 min under solar light and achieving 88% degradation in 2 h under visible light. The exceptional photocatalytic activity of GO/TiO₂ was ascribed to the optimal assembly and interfacial coupling between TiO₂ NPs and GO sheets, which effectively hindered electron–hole recombination. The reaction intermediates of MC-LA photocatalytic degradation were identified, primarily resulting from the attack of $\cdot OH$ radicals on the MC-LA molecule during solar light irradiation. Karaolia et al.[283] also observed the enhanced photocatalytic properties of GO/TiO₂ for urban wastewater treatment. They examined the removal of three antibiotics, sulfamethoxazole, erythromycin, and clarithromycin, under sunlight. The GO/TiO₂ nanocomposite achieved 92%, 86%, and 84% removal of sulfamethoxazole, erythromycin, and clarithromycin, respectively, in 60 min, as shown in Fig. 11(a and b). The improved photocatalytic activity was attributed to the strong interaction between TiO₂ and GO, which facilitates charge transfer from TiO₂ to graphene and prevents electron–hole

This journal is © The Royal Society of Chemistry 2025

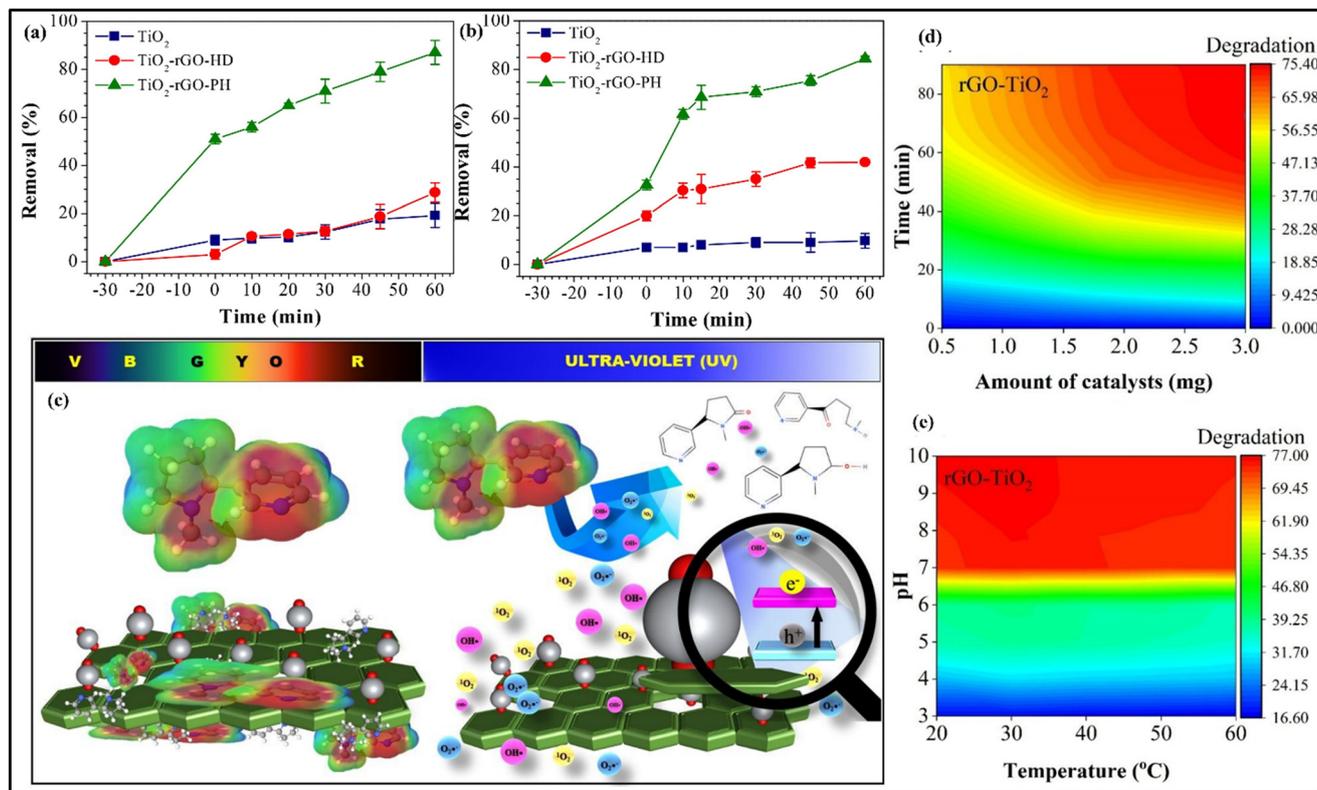*Catal. Sci. Technol.*, 2025, **15**, 1702–1770 | **1727**

Fig. 11 Photocatalytic degradation of (a) clarithromycin and (b) erythromycin. Reproduced with permission from ref. 283 Copyright (2018), Elsevier. (c) Illustration of nicotine degradation by an rGO/TiO$_2$ nanohybrid due to ROS generation under UV irradiation, and exclusive nicotine adsorption on defective carbon rings of the rGO/TiO$_2$ nanohybrid under visible light. (d) Nicotine degradation profiles under UV irradiation over time using varying amounts of rGO/TiO$_2$ catalyst. (e) Effect of pH on nicotine degradation after 90 min at different temperatures using 2 mg of rGO/TiO$_2$.[298] Copyright (2020), the Royal Society of Chemistry.

recombination. Gholamvande et al.[286] developed a GO/TiO$_2$ composite to use in the photodegradation of famotidine, an anti-ulcer medication, as a representative water pollutant. Their findings indicated that the composite achieved 90% degradation of famotidine within 45 min, outperforming plain TiO$_2$, which only managed a 30% degradation rate. Similarly, Calza and colleagues[287] investigated the photocatalytic performance of rGO/TiO$_2$ against risperidone (an antipsychotic medication) under solar and visible light. The rGO/TiO$_2$ nanocomposite exhibited a faster degradation rate than pure TiO$_2$, successfully breaking down 100% of the drug within 90 min of exposure to solar radiation. Furthermore, the nanocomposite demonstrated high stability, maintaining close to 90% efficiency even after being reused in five cycles.

Wang et al.[284] prepared ball-like TiO$_2$ on GO sheets for the removal of oxytetracycline (OTC), a pollutant commonly found in natural surface water and wastewater. Semiconductor photocatalysis is known for its green and efficient removal of organic contaminants; however, most photocatalysts are primarily effective when exposed to UV light. In contrast, the GO/TiO$_2$ photocatalyst achieved high removal efficiencies of 100% and 90% of OTC under sunlight and visible light, respectively. Additionally, the degradation of OTC using TiO$_2$/GO was validated with two real water

samples, resulting in average OTC removal efficiencies of 90% and 75% under solar and visible light, respectively. Pastrana-Martinez et al.[171] addressed the issue of diphenhydramine (DP), a widely used antihistamine and one of the most detected healthcare products in fish liver samples across the United States, by synthesizing a GO/TiO$_2$ nanocomposite for the photocatalytic degradation of DP under UV and visible light. Their study found that GO/TiO$_2$ demonstrated a superior performance compared to bare TiO$_2$ and the commercial photocatalyst P25, achieving 50% degradation of DP within 60 min under UV light and 22% degradation within 240 min under visible light. Parabens, a group of alkyl esters of p-hydroxybenzoic acid, exhibit estrogenic activity and may act as endocrine disruptors, posing a risk to human health and the environment. The primary sources of parabens in the environment include the release of industrial and domestic sewage. Thus, removing parabens from water is crucial for safeguarding human health and the environment.[299] López-Ramón et al.[285] conducted a study in which GO/TiO$_2$ composites were synthesized using a straightforward one-step hydrothermal method. The composites displayed a photocatalytic efficiency of 98.6% for the photodegradation of ethyl paraben (EtP) within 40 min of UV irradiation. This high efficiency was attributed to the uniform assembly of TiO$_2$ NPs on the reduced GO sheets,

enabling the material to function as both an electron acceptor and electron donor, thereby minimizing charge recombination. In another study, Lin et al.[300] investigated the photocatalytic degradation of isopropanol using rGO/TiO$_2$ composites under simulated sunlight. These composites were fabricated using the hydrothermal method and demonstrated the ability to remove 92.24% of isopropanol within 6 h. Numerous researchers have synthesized GO/TiO$_2$ nanocomposites, demonstrating their efficacy in the enhanced photocatalytic degradation and efficient removal of various organic compounds. For instance, Maiti et al.[298] reported the use of one of these nanocomposites to degrade nicotine. Under UV light exposure and with a catalyst dosage of 2 mg, the rGO/TiO$_2$ nanocomposite degraded approximately 80% of nicotine within 90 min. The degradation of nicotine by the rGO/TiO$_2$ nanohybrid was

attributed to the generation of ROS under UV irradiation and the selective adsorption of nicotine on the defective carbon rings of the rGO/TiO$_2$ nanohybrid under visible light, as shown in Fig. 11(c). The kinetic studies on the generation of free radicals showed that the rGO–TiO$_2$ nanosystem exhibits a significant rate of ROSs formation ability, approximately 1.7 times higher than that of TiO$_2$ alone. The profiles of nicotine degradation over time under UV irradiation using varying amounts of rGO–TiO$_2$ catalysts, as well as the impact of pH on nicotine degradation at different temperatures, are illustrated in Fig. 11(d and e), respectively. Additionally, Fan et al.[301] focused on phenol degradation using a GO/TiO$_2$ nanocomposite, while Kaur et al.[302] used rGO/TiO$_2$ for the degradation of triclosan, and Shen et al.[303] applied them for the removal of phenol-4-sulfonic acid. Table 2 summarizes the results for the degradation of pesticides,
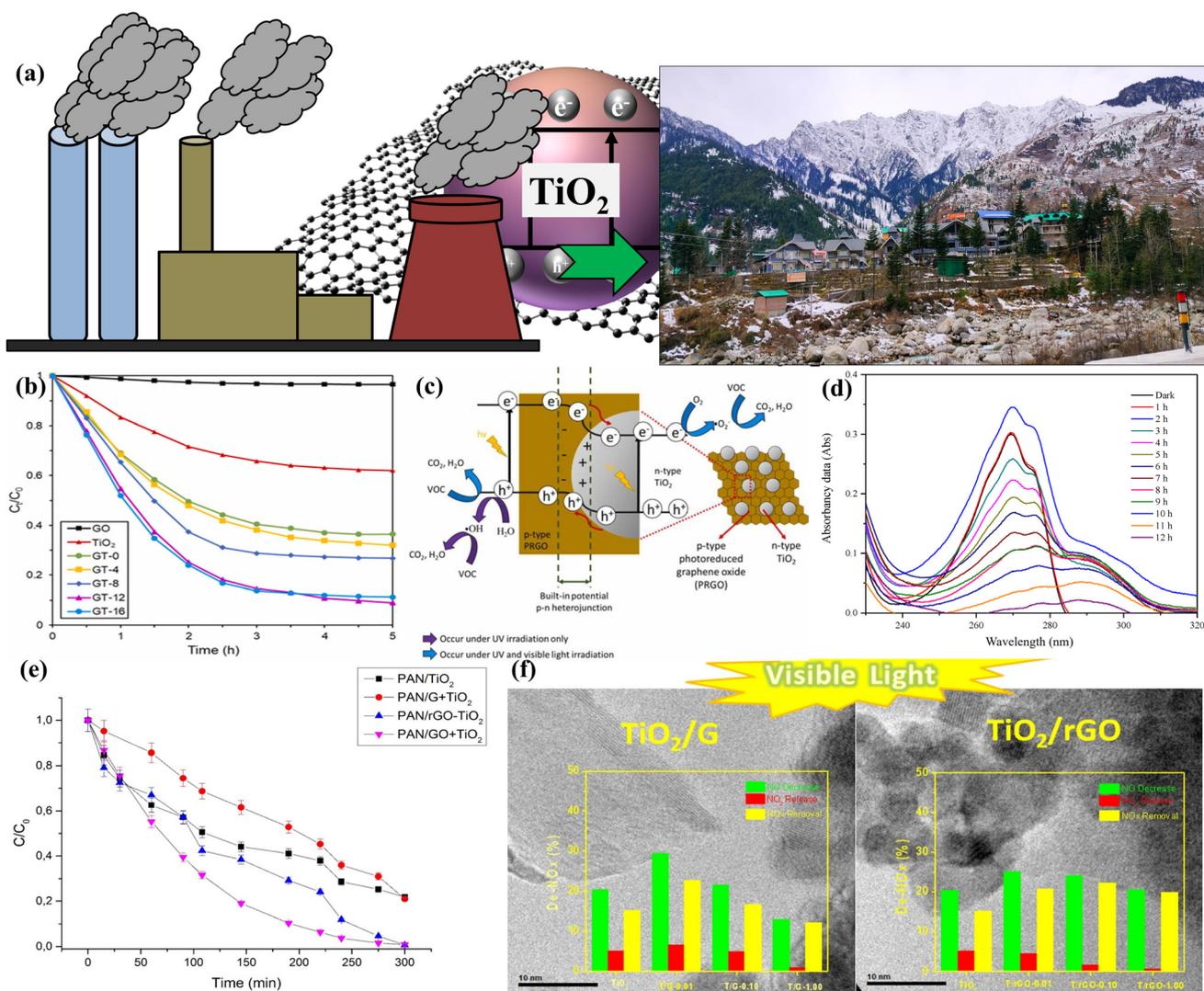

Fig. 12 (a) Schematic illustrating air pollution to clean environment using GO/TiO$_2$. (b) Photocatalytic oxidation of methanol under UV-irradiation. (c) Schematic of rGO/TiO$_2$ p–n heterojunction for the photocatalytic degradation of VOCs. Reproduced with permission from ref. 288 Copyright (2020), Elsevier. (d) Absorption spectra for the photocatalytic degradation of phenol.[291] (e) Photocatalytic degradation of methanol by various photocatalysts. Reprinted (adapted) with permission from ref. 294 Copyright (2017), the American Chemical Society. (f) Effect of GO/TiO$_2$ and rGO/TiO$_2$ on NO$_x$ removal. Reproduced with permission from ref. 296 Copyright (2016), Elsevier.

pharmaceuticals, polymers, personal care products, and chemicals using GO/TiO$_2$ nanocomposite.

5.1.3 Photodegradation of volatile organic compounds. According to the World Health Organization, air pollution is described as "contamination of the indoor or outdoor environment by any chemical, physical, or biological agent that alters the natural characteristics of the atmosphere". Seinfeld and Pandis offered an extended definition, stating that "air pollution is the presence of one or more substances in the air at concentrations or durations exceeding natural levels, with the potential to cause harmful effects".[304] The release of gaseous pollutants into the environment has become a significant concern due to their detrimental effects on human health. This issue can be mitigated through various means such as controlling the sources of pollution, employing air purifiers, using alternative fuels that do not emit pollutants, and adopting green and sustainable methods to eliminate air pollutants.[305]

The common anthropogenic air pollutants found indoors and outdoors include particulate matter (PM), nitrogen oxides (NOx), and volatile organic compounds (VOCs). PM air pollution consists of a mixture of microscopic solid particles and liquid droplets.[306] NOx emissions come from combustion processes in both stationary and mobile sources, which are often associated with traffic-related emissions. Notably, approximately 80% of NOx emissions from vehicles are due to diesel engines.[307,308] The European Union defines VOCs as any organic compounds that have a vapor pressure of 0.01 kPa or higher at 293.15 K, or that exhibit similar volatility under specific use conditions. Anthropogenic VOC emissions are estimated to be around 142 TgC per year in the atmosphere. Additionally, ground-level ozone (O$_3$) is formed through photochemical reactions between sunlight, NOx, and VOCs, resulting in photochemical smog, which has detrimental effects on human health and climate.[309]

Similar to the process of removing pollutants from water, GO/TiO$_2$ has been adopted to eliminate various air pollutants. Fig. 12(a) depicts a schematic diagram of GO/TiO$_2$ used as an air purifier. In a recent study by Tai et al.,[288] GO/TiO$_2$ was prepared using a straightforward UV-assisted photoreduction method. The resulting nanocomposite exhibited improved photoactivity, removing 100% and 24.3% of methanol under UV and visible light, respectively, as shown in Fig. 12(b). This enhanced performance was attributed to the larger built-in potential of the p–n heterojunction (+0.05 eV) and the smaller band gap (2.90–3.15 eV) of GO/TiO$_2$, which slowed down the charge carrier recombination and increased light absorption. The primary reactive species responsible for the photocatalytic activities were hVB$^+$ species and ·O$_2^-$ radicals, as described in the schematic diagram in Fig. 12(c). Zhou et al.[289] enhanced the interaction between TiO$_2$ and rGO by reducing the Fermi level of GO using Cu^{2+}. The Cu^{2+} treatment promoted the formation of a thicker and more uniform layer of TiO$_2$ NPs on the rGO surface. This optimized GO/TiO$_2$ catalyst effectively degraded 100% of toluene within 48 min, surpassing the performance of pure TiO$_2$ and unoptimized rGO/TiO$_2$. The

optimized rGO/TiO$_2$ exhibited photocatalytic reaction rates that were 1.47 times and 1.91 times higher than that of the unoptimized rGO/TiO$_2$ and pure TiO$_2$, respectively. This improvement highlights the significance of optimizing the interaction between TiO$_2$ and rGO for enhancing photocatalytic activity. Lin et al.[290] employed a GO/TiO$_2$ nanocomposite to photodegrade two volatile organic compounds (VOCs), acetaldehyde and o-xylene. The rGO/TiO$_2$ nanocomposites were synthesized using a simple solvothermal process for the photocatalytic reactions. This study demonstrated a significant improvement in the removal efficiency of acetaldehyde and o-xylene. The removal rates increased sharply from 15% and 12% with pure TiO$_2$ to 42% and 54% when using rGO/TiO$_2$ as the photocatalyst, respectively.

In a different study, Wang et al.[291] prepared an rGO/TiO$_2$ nanocomposite for the degradation of phenol. The rGO/TiO$_2$ nanocomposites exhibited a high specific surface area of 156.4 m^2 g^{-1} and band gap of 2.91 eV. This nanocomposite effectively degraded phenol to 97.9% and had a degradation rate constant of 0.0190 h^{-1}, as given in Fig. 12(d). Methyl ethyl ketone (MEKT) is a ketone compound known for its high mobility and toxicity, posing significant risks to both the ecology and human health, even at low concentrations. Thus to address this, Tri et al.[292] synthesized a GO/TiO$_2$ catalyst for the degradation of MEKT. Their study explored various parameters, including catalyst dose, inlet concentration of MEKT, relative humidity (RH), and gas flow rate, to understand their effects on the degradation process. The GO/TiO$_2$ nanocomposite demonstrated a high efficiency in removing MEKT, achieving a removal rate of 96.8% under visible light, which significantly outperformed commercial TiO$_2$, only achieving a removal rate of 32.7%. This suggests that the use of the GO/TiO$_2$ catalyst is a promising approach for the degradation of MEKT and improving air quality. Chen et al.[293] synthesized an rGO/TiO$_2$ nanocomposite through a simple and mild one-step water bath method for the degradation of indoor gaseous formaldehyde. The rGO/TiO$_2$ nanocomposite successfully removed 72% of formaldehyde in 9 h through photocatalytic action, demonstrating significantly enhanced activity compared to pure TiO$_2$. This suggests that the rGO/TiO$_2$ nanocomposite is a promising material for improving indoor air quality by efficiently degrading gaseous formaldehyde. Roso et al.[294] prepared a GO/TiO$_2$ photocatalyst and investigated the impact of the degree of oxidation of GO. They found that rGO provided the best performance for the gas-phase degradation of methanol, which was attributed to its enhanced electron mobility facilitated by its strong interaction with the photocatalyst. The GO/TiO$_2$ nanocomposite achieved the complete degradation (100%) of methanol in 300 min, demonstrating high photocatalytic efficiency, as reveled in Fig. 12(e). This suggests that optimizing the degree of oxidation of GO can play a crucial role in enhancing the performance of GO/TiO$_2$ photocatalysts for the degradation of volatile organic compounds.

NO$_x$ are pollutants known for their harmful effects on human health and their role in the formation of smog and acid rain. Zhu et al.[295] improved the photocatalytic activity of

1730 | Catal. Sci. Technol., 2025, **15**, 1702–1770

This journal is © The Royal Society of Chemistry 2025

black TiO_2 by synthesizing a GO/TiO_2 nanocomposite. This nanocomposite displayed remarkably high activity in the photocatalytic removal of nitrogen monoxide (NO), achieving an NO conversion rate of 50.4%, which significantly exceeded that of pure black TiO_2 (33.9%). This enhanced performance demonstrates the potential of the GO/TiO_2 nanocomposite as an effective photocatalyst for reducing the NO_x concentration in the environment. Trapalis et al.[296] synthesized a GO/TiO_2 nanocomposite via a solvothermal method and achieved the efficient removal of NOx. The band gap of the GO/TiO_2 composite was reduced to 3.08 eV compared to that of 3.20 eV for pure TiO_2, which contributed to its enhanced photocatalytic performance. The GO/TiO_2 nanocomposite demonstrated an NOx removal efficiency of 52.28% under UV light and 29.34% under visible light, as given in Fig. 12(e). These results indicate that the GO/TiO_2 nanocomposite is an effective photocatalyst for the removal of NO_x and has

potential for applications in air purification. Table 2 summarizes the literature related to the photocatalytic removal of VOCs using GO/TiO_2 nanocomposites.

In conclusion, the GO/TiO_2 nanocomposites offer versatile functionality as materials for wastewater treatment and air purification. This is due to the synergistic combination of the photocatalytic properties of TiO_2 and the excellent electrochemical performance of GO. Together, these properties make GO/TiO_2 nanocomposites a highly effective option for removing a variety of pollutants from water and the air, contributing to improved environmental quality and human health.

5.1.4 Photodegradation of MPs and polymers. Plastic photodegradation typically takes 300 to 500 years naturally, while chemical degradation often requires additional energy or leads to secondary pollution. The primary transportation pathways of major MPs from different sources to
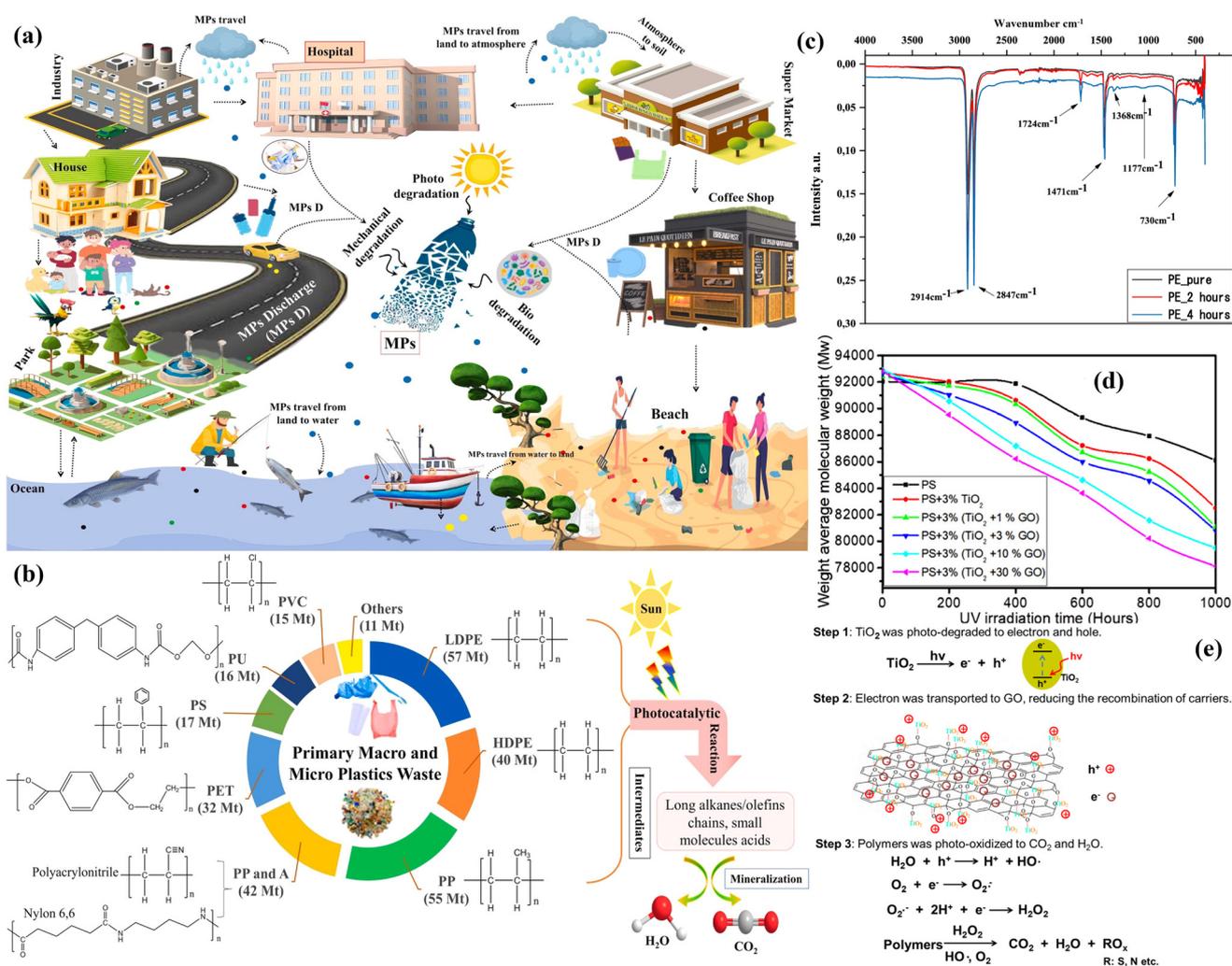

Fig. 13 (a) Primary source of MPs in the environment. (b) Commonly used plastics, along with their chemical structures and photocatalytic degradation strategies. Reproduced with permission from ref. 314 Copyright (2021), Elsevier. (c) FTIR spectra of PE particles before and after 2 and 4 hours of UV exposure. Reproduced with permission from ref. 312 Copyright (2022), Springer Nature. (d) Decrease in average molecular weights under UV irradiation. Reproduced with permission from ref. 313 (e) illustration of the proposed mechanism for polymer photodegradation. Reproduced with permission from ref. 315.

This journal is © The Royal Society of Chemistry 2025

Catal. Sci. Technol., 2025, 15, 1702–1770 | 1731

environmental media are illustrated in Fig. 13(a). The most common plastics include PE, polypropylene (PP), poly-vinyl chloride (PVC), PS, and phenolic resin, with PP and PE being the most widely used in everyday life.[310] The chemical structures of these frequently used plastics, together with the corresponding amounts of waste produced, are presented in Fig. 13(b). Given that global plastics are primarily composed of polymers, innovative technologies are essential for the effective breakdown of these materials in the natural environment. This necessity underpins the study of new methods for future plastic degradation.[311] In response to this emerging issue, Uogintė et al.[312] synthesized a GO/TiO$_2$ nanocomposite for the efficient photocatalytic degradation of propylene (PE). Degradation experiments were performed in a batch system under UV light to optimize the photocatalyst amount, initial pH, and contact time. Under the optimized conditions, the GO/TiO$_2$ nanocomposite achieved a mass loss of 23.67% after 120 min and 50.46% after 480 min. Their study found that lower pH levels and longer contact times with UV-activated nanomaterials were more favorable for achieving a higher degradation efficiency. The FTIR results confirmed the efficient degradation of PE microplastic particles, as indicated by the appearance of peaks corresponding to newly formed functional groups at 1724 cm^{-1} and 1177 cm^{-1}, together with an increase in the carbonyl index, as shown in Fig. 13(c). Dinoop et al.[313] synthesized a GO/TiO$_2$ nanocomposite with varying GO weight percentages using an ultrasonication-assisted hydrothermal approach to study the photodegradation of PS. The GO/TiO$_2$-loaded solid-state PS exhibited accelerated photodegradation compared to pristine PS and the PS-TiO$_2$ composite.

Gel permeation chromatography revealed that the degradation proceeded through random chain scission, leading to a decrease in the average molecular weight. The highest degradation percentage was observed for the PS-GO/TiO$_2$ composite with 30% GO, as shown in Fig. 13(d), depicting the maximum decrease in the MW of PS. The mechanical strength studies indicated a reduction in the strength of the PS-GO/TiO$_2$ composite upon UV irradiation, which was attributed to the polymer chain deterioration due to bond rupture. Additionally, shifts in the decomposition temperature and glass transition temperature to lower values further supported the conclusion that polymer chain deterioration occurred due to bond cleavage as a result of photodegradation under UV irradiation. Similarly, in the study by Verma et al.,[316] polypropylene was successfully degraded under natural sunlight. The results demonstrated that GO/TiO$_2$ outperformed TiO$_2$ alone in degrading polypropylene. Due to the higher photocatalytic activity of the GO/TiO$_2$ nanocomposite, it effectively deteriorated the polypropylene surface by attacking C–H groups and generating PP macroradicals. This improvement with GO/TiO$_2$ was attributed to its more efficient utilization of the solar spectrum, reduced recombination rate of photogenerated electron–hole pairs, and increased surface area. Shi et al.[315] prepared a GO/TiO$_2$ nanocomposite. The introduction of GO in TiO$_2$ resulted in a reduced band gap from 3.28 eV (in TiO$_2$) to 3.03 eV (in GO/TiO$_2$). This GO/TiO$_2$ nanocomposite could completely degrade polymers in the natural environment within 15 days. The photodegradation mechanism of polymers by the GO/TiO$_2$ composite is illustrated in Fig. 13(e). When exposed to natural light, charge separation occurs in the TiO$_2$ semiconductor. The generated electrons are efficiently transferred to the graphene sheets of GO, while the holes remain within TiO$_2$, reducing the charge recombination. The accumulated holes undergo oxidative reactions with H$_2$O to produce ˙OH radicals. At the same time, the electrons and h$^+$ interact with O$_2$ to form H$_2$O$_2$, leading to the degradation of the polymers. These radicals attack polymers and degrade them into simple molecules such as CO$_2$ and H$_2$O.

5.1.5 As photo-biomaterial in antibacterial/antiviral applications. The COVID-19 pandemic has placed significant strain on public health worldwide.[317] Additionally, diarrhea, which is caused by enterotoxins produced by *Escherichia coli* and transmitted through contaminated drinking water, leads to 1.3 million deaths in children under five each year.[318] Antibiotics are commonly used to treat pathogenic bacteria, but their overuse has contributed to the rise of drug-resistant bacterial strains.[319,320] Thus, photocatalytic technology has emerged as a green and advanced oxidation process (AOP) for disinfection, attracting increasing attention as an alternative method. TiO$_2$ is the most widely applied photocatalyst for disinfection, as first reported by Matsunaga et al.[321] This technology holds promise for addressing waterborne pathogens and other contaminants, providing a sustainable and effective solution for public health challenges. GO/TiO$_2$ composites are highly effective materials for the photocatalytic removal of microorganisms.[194,322,323] Their strong antimicrobial properties stem from their large surface area, excellent 2D structure, increased adsorption capacity for microbes, rapid electron movement *via* conjugated π bonds, and expanded range of visible light absorption.[153,324]

Prakash et al.[325] investigated several GO/TiO$_2$ nanohybrids with variable GO concentrations (10–50 wt%). Their antibacterial activity was assessed against *S. aureus*, *P. aeruginosa*, *Escherichia coli*, and *E. faecalis*. All the GO/TiO$_2$ samples possessed antibacterial action, while the nanohybrid with the highest GO concentration outperformed the others. The improved performance was attributed to the reduction in electron–hole recombination. Chai et al.[326] studied the *in vitro* and *in vivo* antibacterial activity of a GO/TiO$_2$ coating under light irradiation. The results demonstrated that the GO/TiO$_2$ composite exhibited excellent antibacterial activity against *Streptococcus mutans* both *in vitro* and *in vivo* under NIR light irradiation. The *in vitro* antibacterial activity against *S. mutans* was assessed using the spread plate method. After NIR light exposure, there was no significant difference in the bacterial colonies between the Ti and TiO$_2$ coatings. However, the GO/TiO$_2$ coating showed a marked reduction in

1732 | *Catal. Sci. Technol.*, 2025, **15**, 1702–1770

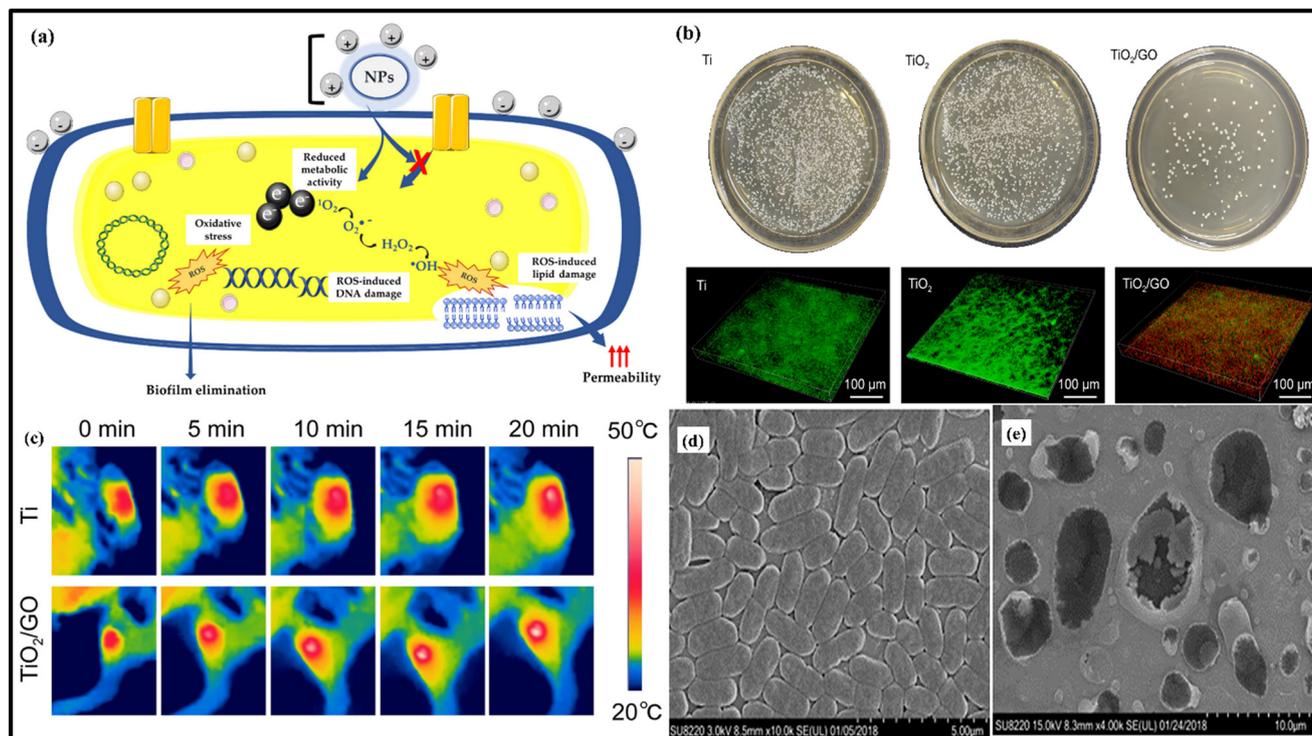This journal is © The Royal Society of Chemistry 2025

Fig. 14 (a) General mechanism of antibacterial action of nanomaterials.[327] (b) *S. mutans* colonies on various samples and fluorescence images of *S. mutans* on the samples. (c) Thermal images of GO/TiO$_2$ coatings. Reproduced with permission from ref. 326 copyright (2022), Springer Nature. FE-SEM images of *Enterobacter hormaechei* (d) before and (e) after UV irradiation in the presence of rGO/TiO$_2$. Reproduced with permission from ref. 328 Copyright (2021), Elsevier.

bacterial colonies, indicating that the antibacterial activity was enhanced following GO modification, as shown in Fig. 14(a). This improvement was attributed to the synergistic effects of hyperthermia and ROS generated during NIR light irradiation. The antibacterial properties of the samples were further evaluated using live/dead staining. As illustrated in Fig. 14(b), bacteria on both Ti and TiO$_2$ coatings were entirely stained green after exposure to NIR light, indicating the survival of *S. mutans*, whereas the GO/TiO$_2$ coating showed much less isolated live bacteria. Further, to assess the *in vivo* antibacterial activity of the GO/TiO$_2$ coating, an animal model with *S. mutans* infection was developed in a mouse tibia. After surgical implantation, the implants were exposed to NIR light, resulting in temperatures of approximately 40 °C for the Ti coating and 50 °C for the GO/TiO$_2$ coating. This indicated that the GO/TiO$_2$ coating exhibited excellent photothermal properties *in vivo*, as shown in Fig. 14(c). In the Ti group, significant neutrophil infiltration was observed, indicating severe soft tissue infection. In contrast, only mild inflammation was noted in GO/TiO$_2$.[326]

Similarly, Jin *et al.*[329] investigated the combined impact of NPs and GO in a GO/TiO$_2$ hybrid on A549 cells. They claimed that this combination would harm the mitochondria, enhance the number of lysosomes, and hence destabilize and kill the cell. Chang *et al.*[330] synthesized magnetic GO/TiO$_2$ nanohybrids. The results showed that GO/TiO$_2$ has high antibacterial action against *E. coli*. GO/

TiO$_2$ was discovered to totally inactivate *E. coli* virtually within 30 min of sun irradiation.[330] Raja *et al.*[331] used rGO/TiO$_2$ to kill *S. aureus* and *E. coli*. This nanocomposite demonstrated improved antibacterial action against both pathogens. The higher antibacterial activity of the rGO–TiO$_2$ nanocomposite can be attributed to the following reasons: (1) the presence of rGO enhances the interaction between the TiO$_2$ surface and bacteria by converting it from a negatively charged to positively charged state. (2) The presence of rGO increases the visible light absorption. In the investigation by Akhavan and Ghaderi,[332] GO/TiO$_2$ films were used to photo-inactivate *E. coli* in water solutions using solar light. This was one of the earliest uses of GO/TiO$_2$ films, which demonstrated much greater efficiency than anatase TiO$_2$ films (improvement by a factor of around 7.5). The improved performance was due to the reduction in electron–hole recombination. Similarly, Zhou *et al.*[328] investigated the antibacterial activity and mechanism of an rGO/TiO$_2$ nanocomposite against *E. hormaechei*. Under UV-visible light irradiation, the rGO/TiO$_2$ nanocomposite demonstrated greater antibacterial efficacy against *E. hormaechei* compared to individual TiO$_2$ or rGO, as confirmed by the FESEM images of the bacteria, as shown in Fig. 14(d and e), respectively. This enhanced activity was attributed to the improved adsorption and reduced recombination of photo-induced e$^-$ and h$^+$ pairs. The hybrid photocatalyst facilitated better charge separation and

This journal is © The Royal Society of Chemistry 2025

Catal. Sci. Technol., 2025, **15**, 1702–1770 | 1733

chemical binding, thereby accelerating the antibacterial process. Wanag *et al.*[323] synthesized an rGO/TiO$_2$ nanocomposite *via* a hydrothermal method to investigate its antibacterial activity against *E. coli*. This nanocomposite had a band gap of 3.27 eV and completely inhibited bacterial growth within 75 min under artificial solar light.

Gao *et al.*[194] examined the impact of different TiO$_2$ nanostructures on GO for antibacterial applications. The GO/TiO$_2$ composites with spherical TiO$_2$ NPs displayed improved antibacterial activity against *E. coli*. Under sunlight, the GO/TiO$_2$ composite completely eradicated the bacteria within 120

min. Wang *et al.*[333] synthesized a highly recoverable GO/TiO$_2$ composite using a simple ultrasonic treatment of GO nanosheets and TiO$_2$ NPs. The photocatalytic disinfection activity of the GO/TiO$_2$ composite was examined under a solar simulator. The composite successfully removed 99.5% of *E. coli* within 90 min of irradiation, demonstrating its effectiveness for microbial disinfection. Similarly, Fernandez-Ibanez *et al.*[322] prepared rGO/TiO$_2$ composites through the photocatalytic reduction of exfoliated GO by TiO$_2$ under UV irradiation. The rGO/TiO$_2$ composite was tested in suspension reactors for disinfection against *E. coli* and *Fusarium solani* under sunlight
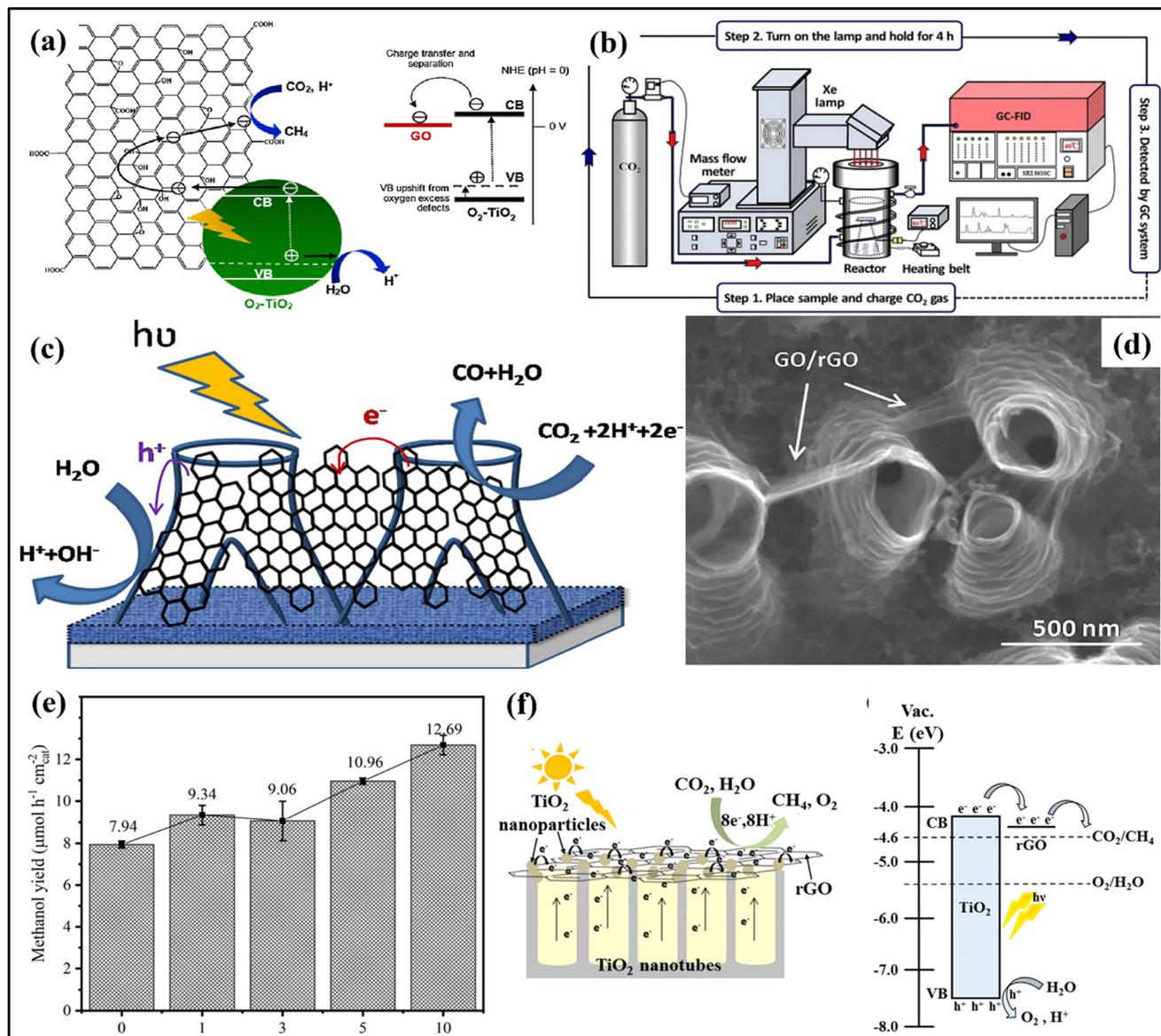

Fig. 15 (a) Schematic of CO$_2$ reduction and charge transfer on GO/OTiO$_2$ nanocomposite. Reproduced with permission from ref. 339 Copyright (2015), Elsevier. (b) Schematic of the setup for the photocatalytic conversion reaction system used for CO$_2$ reduction. Reproduced with permission from ref. 303 Copyright (2021), Elsevier. (c) Schematic of the photocatalytic CO$_2$ reduction process involving GO/rGO-wrapped TiO$_2$ multi-leg nanotubes. (d) FESEM image of GO/rGO-wrapped TiO$_2$ nanotubes. Reproduced with permission from ref. 335 Copyright (2019), Elsevier. (e) Methanol yield over GO/TiO$_2$. Reproduced with permission from ref. 219 Copyright (2018), Elsevier. (f) Schematic of the photocatalytic conversion of CO$_2$ to CH$_4$ and energy level diagram of rGO/TiO$_2$ under simulated solar illumination. Reproduced with permission from ref. 340 Copyright (2015), Elsevier.

and compared to pure TiO_2. The composite completely eradicated both microorganisms within 30 min of UV light exposure. An increased rate of inactivation of *E. coli* was observed with the rGO/TiO_2 composite compared to P25 alone, while the rate of inactivation of *F. solani* spores was similar for both rGO/TiO_2 and P25. Selvakumar *et al.*[331] developed an rGO/TiO_2 nanocomposite with a reduced band gap of 2.7 eV as an effective antibacterial agent against *Staphylococcus aureus* and *Escherichia coli*. The rGO/TiO_2 photocatalyst was active under visible light and efficiently degraded both types of bacteria. Table 2 summarizes a list of various GO/TiO_2 nanocomposites used as antibacterial agents in various studies.

5.2. Photocatalytic reduction of carbon dioxide into useful products

The long-standing reliance on fossil fuels for industrialization and economic development has not only depleted these carbon-emitting resources but has also resulted in unprecedented atmospheric levels of CO_2.[155,334–336] As a major greenhouse gas, CO_2 significantly contributes to global warming and climate change. The photocatalytic reduction of CO_2 into valuable fuels has gained global attention given that it simultaneously mitigates the severe challenge of global warming and addresses the impending energy crisis.[337] CO_2 is a highly stable molecule given that it is the end product of the combustion of all carbon-based fuels. Converting CO_2 into potential fuels is an endothermic process, meaning that it requires a significant energy input to drive the reaction. This high energy demand presents a major challenge to the efficiency and feasibility of CO_2 conversion technologies.[338] Fig. 15(a) shows the general photocatalytic mechanism and charge separation of $GO/$ oxygen rich-TiO_2 ($GO/OTiO_2$) for CO_2 reduction.

To address these emerging challenges, Olowoyo *et al.*[341] fabricated a nanocomposite of rGO with TiO_2 NPs using a combined sonothermal–hydrothermal method. This process resulted in a nanocomposite with a reduced band gap of 2.9 eV compared to the band gap of pure TiO_2 (3.2 eV). The reduction in the band gap enhanced the activity of the composite for the photocatalytic reduction of CO_2 to methanol under UVA and visible light irradiation, achieving a methanol production rate of 2.33 mmol g^{-1} h^{-1}. This demonstrates the potential of the rGO/TiO_2 nanocomposite for efficient and effective CO_2 conversion into valuable fuels.

Further, Liu *et al.*[303] prepared an rGO/TiO_2 aerogel using a one-step hydrothermal method, followed by freeze-drying. The TiO_2 in this aerogel had a nano-rod shape and was uniformly distributed within the rGO sheets, resulting in a reduced band gap of 2.9 eV. The aerogel efficiently converted CO_2 into various valuable fuels such as methanol (MeOH), methane (CH_4), ethanol (EtOH), and dimethyl ether (DME). This rGO/TiO_2 photocatalyst achieved a 15.7 times higher total carbon conversion rate than that of pure P25, demonstrating its potential for highly efficient CO_2 conversion. Fig. 15(b) shows a photocatalytic conversion

reaction system that was used for efficient CO_2 conversion into value-added fuels.

In a separate study, Tan *et al.*[342] fabricated a GO/TiO_2 nanocomposite containing 5 wt% GO and oxygen-rich TiO_2 through chemical methods. GO was introduced using wet chemical impregnation. This GO/TiO_2 nanocomposite demonstrated efficient CO_2 reduction to methane, achieving a total yield of 3.450 μmol g^{-1} after 8 h of reaction time. Additionally, it exhibited an apparent quantum yield of 0.0103%. Similarly, Rambabu *et al.*[335] developed a novel composite architecture consisting of GO-wrapped TiO_2 nanotubes for the photocatalytic reduction of CO_2. Fig. 15(c) shows the CO_2 reduction mechanism by the GO/TiO_2 nanocomposite. The TiO_2 nanotubes, formed through electrochemical anodization, were enveloped with GO layers, creating interconnecting bridges between adjacent nanotubes, as shown in Fig. 15(d). This distinctive nanostructure facilitated the separation of photogenerated electron–hole pairs and improved charge transfer for the reduction of adsorbed CO_2. The GO/TiO_2 composite exhibited outstanding photocatalytic activity, achieving a maximum CO yield of 1538 μmol g^{-1} within the initial 20 min of UV-A irradiation, which stabilized to approximately 760 μmol g^{-1} after 2 h. Velasco-Hernández *et al.*[343] fabricated GO/TiO_2 nanocomposite thin films on glass substrates using a sol–gel route and the dip coating technique for photocatalytic applications. After annealing at 450 °C, the bandgap of the composite was estimated to be in the range of 3.38–3.45 eV. The nanocomposite was employed as a photocatalyst for efficiently reducing CO_2 to methanol under simulated UV light at 25 °C. The results of CO_2 photoreduction indicated that the methanol yield increased with a higher amount of GO in the thin TiO_2 films, suggesting the synergistic effect of the nanocomposite. These thin films showed promising potential application in CO_2 photoreduction, with a methanol production of 68.443 μmol cm^{-2} observed after 5 h of reaction under UV light.

Shehzad *et al.*[344] reported the enhanced photocatalytic conversion of CO_2 using rGO/TiO_2. The performance of this photocatalyst was assessed for CO_2 reduction with H_2O in a continuous gas-phase fixed-bed photoreactor. The presence of rGO/TiO_2 resulted in the highest amounts of methane (CH_4) and carbon monoxide (CO) at 12.75 and 11.93 μmol g^{-1} h^{-1}, respectively, outperforming bare TiO_2. The improved photocatalytic activity was attributed to several factors, including interfacial chemical bonding, efficient electron transfer, enhanced light absorption, and increased CO_2 adsorption facilitated by rGO. Likewise, Liu *et al.*[345] synthesized rGO/TiO_2 nanocomposites for the photoreduction of CO to CH_4 and MeOH under a high-pressure mercury lamp. These nanocomposites demonstrated notable photocatalytic activity in reducing CO_2 to CH_4 (2.10 μmol g^{-1} h^{-1}) and CH_3OH (2.20 μmol g^{-1} h^{-1}), owing to the synergistic effect between TiO_2 and graphene. To develop a noble metal-free approach for CO_2 reduction, Razzaq *et al.*[340] synthesized rGO/TiO_2, where TiO_2 nanotubes were enveloped

This journal is © The Royal Society of Chemistry 2025

Catal. Sci. Technol., 2025, **15**, 1702–1770 | **1735**

within rGO to develop a novel nanostructured photocatalytic material. This unique nanostructure exhibited significantly enhanced photocurrent density and photochemical activity, facilitating the conversion of CO_2 into methane under simulated solar light irradiation. The improved performance was attributed to the combined effect of enhanced light absorption and effective charge separation promoted by rGO. rGO demonstrated a methane evolution rate (5.67 ppm cm^{-2} h^{-1}), which was approximately 4.4 times higher than that of pure TiO_2 (1.28 ppm cm^{-2} h^{-1}). The proposed mechanism for photocatalytic CO_2 photoreduction and the corresponding energy level diagram based on the relative positions of the CB, VB, and redox potential for rGO/TiO_2 are illustrated in Fig. 15(f). Upon illumination, electron–hole (e^-/h^+) pairs are generated at various active sites, including the TiO_2 nanotubes and the surface TiO_2 NPs embedded within the rGO platelets. The 1D TiO_2 nanotubes facilitated unidirectional vectorial charge transfer to the rGO platelets, while the photoexcited electrons from the surface TiO_2 NPs were effectively separated by the rGO platelets. These photogenerated electrons react with adsorbed CO_2 molecules and protons derived from water oxidation to produce CH_4. Simultaneously, the holes migrate in the opposite direction to oxidize adsorbed H_2O. The CB of anatase TiO_2 is positioned at −4.2 eV, and the work function of rGO is located at −4.4 eV *versus* vacuum, whereas the redox potential of the CO_2/CH_4 pair is approximately −4.6 eV. Under illumination, the photoexcited electrons in TiO_2 are efficiently extracted by the rGO platelets and transferred to surface-adsorbed CO_2, resulting in CH_4 generation with an enhanced yield. The rGO platelets serve as an efficient pathway for separating and transferring photoexcited electrons, significantly improving the photocatalytic performance. Additionally, the VB of TiO_2, located below the water redox potential (−5.3 eV *vs.* vacuum), enables the oxidation of water molecules, producing O_2 and H^+ protons. This dual process of CO_2 reduction and water oxidation highlights the synergistic role of rGO and TiO_2 in achieving efficient photocatalytic activity. Various studies using GO/TiO_2 nanocomposites for CO_2 reduction into value-added fuels are summarized in Table 3.

5.3. Photocatalytic H_2 production

The current depletion of natural fuels presents a concerning situation for our planet, emphasizing the urgent need to establish alternative sustainable energy sources. In this case, H_2 is emerging as a promising solution due to its sustainability, renewability, environmental benefits, and cost-effectiveness.[355,356] However, approximately 95% of H_2 is derived from nonrenewable resources, and thus researchers are actively exploring methods to produce H_2 economically. One of these methods is photovoltaic water electrolysis, which utilizes semiconductor materials with small band gaps to generate H_2 at low costs. Another promising approach for H_2 production is photocatalytic water splitting, employing a semiconductor as a photocatalyst powered by solar energy. This method offers a clean, cost-effective, and environmentally friendly means for producing H_2.[357–359] Photocatalytic H_2 production has garnered significant attention as the most efficient and cost-effective method for synthesizing H_2. This process, known as water splitting, involves the photocatalytic cleavage of water molecules (yielding H_2 (g) and O_2 (g)) using two abundant natural sources, water and solar light. This reaction, involving the production of H_2 and O_2, is referred to as photo reduction and the oxidation of water, respectively.[360] The addition of rGO to TiO_2 proves advantageous in augmenting H_2 production across UV, UV-vis, and specifically the visible light spectrum. The present focus is directed towards enhancing

Table 3 List of GO/TiO_2 results in CO_2 reduction and H_2 production

Catalyst	Sacrificial agent	Solvent (reductant)	Radiation	Evaluation	Efficiency	Ref.
5 mg	Triethanolamine	20 mL HPLC-grade water : ACN mixture (4 : 16 v/v)	UV light	CO_2 reduction to MeOH	2330 μmol g^{-1} h^{-1}	341
20 mg	—	Water	UV-vis light	CO_2 reduction to MeOH, CH_4, EtOH, DME	3.37 μmol g^{-1} h^{-1}	303
—	—	Water	UV light	CO_2 reduction to MeOH	12.69 μmol h^{-1} cm^2	343
—	—	Water	Visible light	CO_2 reduction to CH_4	3.450 μmol g^{-1}	342
—	—	Water	UV light	CO_2 reduction to CO	760 μmol g^{-1}	335
—	—	Water	UV light	CO_2 reduction to CH_4	12.75 μmol g^{-1} h^{-1}	344
—	—	Water	UV light	CO_2 reduction to CO	11.93 μmol g^{-1} h^{-1}	344
100 mg	—	100 mL distilled water containing KOH (0.2 mol L^{-1})	UV light	CO_2 reduction to CH_4 and MeOH	2.10 and 2.20 μmol g^{-1} h^{-1}	345
—	—	—	Sunlight	CO_2 reduction to CH_4	5.67 ppm cm^{-2} h^{-1}	340
—	—	—	UV light	H_2 production	39.26 mmol h^{-1} g^{-1}	346
—	—	—	Sunlight	H_2 production	168 μmol h^{-1}	347
200 mg	2% methanol	200 mL water	Visible light	H_2 production	875 μmol g^{-1} h^{-1}	348
2 mg	Ethanol	Water	UV light	H_2 production	9530 μmol h^{-1} g^{-1}	349
—	—	—	UV light	H_2 production	800 μmol h^{-1} m^2	350
50 mg	Methanol	20% v/v methanol aqueous solution	UV-vis	H_2 production	13 996 μmol g^{-1} h^{-1}	351
—	—	—	UV light	H_2 production	127.5 μmol cm^{-2} h^{-1}	352
100 mg	Triethanolamine	Water	Visible light	H_2 production	380 μmol h^{-1}	353
—	—	—	Visible light	H_2 production	305.6 μmol h^{-1}	354

1736 | *Catal. Sci. Technol.*, 2025, **15**, 1702–1770

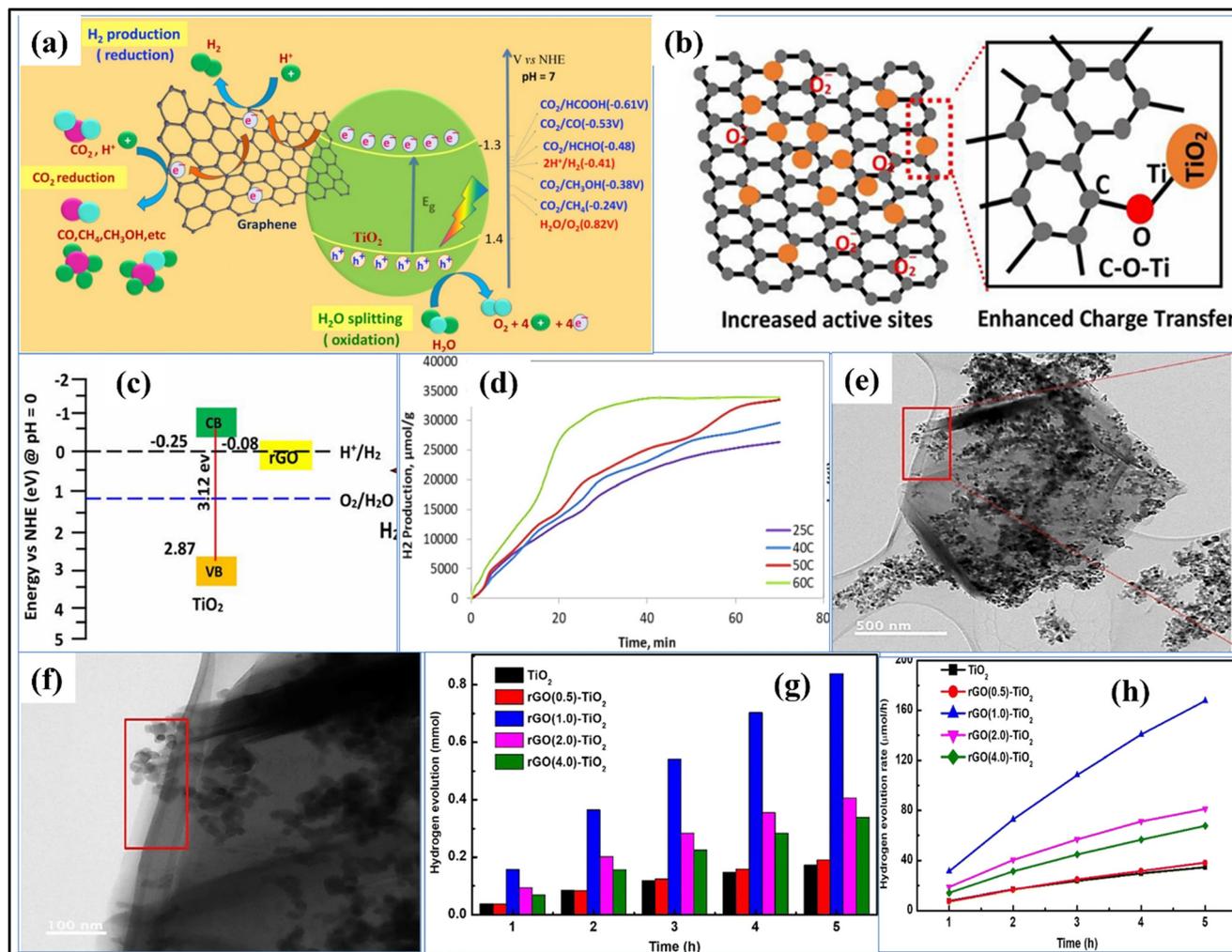This journal is © The Royal Society of Chemistry 2025

Fig. 16 (a) Schematic illustrating photocatalytic H$_2$ production mechanism of GO/TiO$_2$ nanocomposite.[362] Copyright (2021), Elsevier. (b) Formation of the Ti–O–C bond in the separation-free rGO/TiO$_2$ catalyst and its role in the photocatalytic process. (c) Energy band diagram of TiO$_2$ and rGO illustrating the charge transfer mechanisms for the photocatalytic H$_2$ production process in rGO/TiO$_2$. Reproduced with permission from ref. 347 Copyright (2020), Springer Nature. (d) Photocatalytic H$_2$ production rate in the presence of rGO/TiO$_2$ photocatalyst. Reproduced with permission from ref. 346 Copyright (2022), Elsevier. (e and f) HRTEM image of GO/P25.[348] (g and h) Photocatalytic water splitting in the presence of rGO/TiO$_2$ photocatalyst. Reproduced with permission from ref. 347 copyright (2020), Springer Nature.

the compatibility of photocatalysts with visible light activity. Under UV and UV-vis irradiation, the optimal concentration of rGO, the hierarchical structure of TiO$_2$, and the overall quantity of photocatalyst within the solvent are pivotal for achieving photocatalytic efficacy. However, a higher concentration of rGO can obscure the catalytic centers of TiO$_2$.[361] Fig. 16(a) shows the photocatalytic mechanism of H$_2$ production on GO/TiO$_2$.

Recently, Moustafa *et al.*[346] synthesized rGO/TiO$_2$ nanostructures *via* the hydrothermal method for efficient H$_2$ production through photoelectrochemical water-splitting reactions. The proposed mechanism suggests that TiO$_2$ forms Ti–O–C bonds with rGO, facilitating electron migration and enhancing the charge separation efficiency, as shown in Fig. 16(b). The excited electrons on the TiO$_2$ side are utilized in the H$_2$ evolution reaction, while the excited electrons on the rGO sites can readily transfer to the TiO$_2$ acceptor

through a percolation mechanism, thereby promoting the H$_2$ evolution reaction. The energy band diagram of TiO$_2$ and rGO illustrating the charge transfer mechanisms is shown in Fig. 16(c). The comparative analysis with anatase TiO$_2$ NPs and pristine rGO revealed that the rGO/TiO$_2$ nanocomposite exhibited a two-fold increase in photocatalytic H$_2$ production activity, reaching the maximum H$_2$ production rate of 39.26 mmol h^{-1} g^{-1} catalyst, as shown in Fig. 16(d). Hernández-Majalca *et al.*[348] aimed to develop a fast and straightforward synthesis method for GO/TiO$_2$ nanocomposites with self-tuning optoelectronic properties, ideal for photocatalytic H$_2$ production applications. Fig. 16(e and f) show the HRTEM images of the synthesized GO/TiO$_2$ nanocomposite. The GO/TiO$_2$ nanocomposites exhibited a reduced band gap of 2.6 eV compared to that of TiO$_2$ of 3.1 eV, resulting in enhanced H$_2$ production of 875 μmol g^{-1} h^{-1}, which is 15 times greater than that of bare TiO$_2$. This heightened activity of the

This journal is © The Royal Society of Chemistry 2025

Catal. Sci. Technol., 2025, **15**, 1702–1770 | **1737**

nanocomposite was attributed to the role of GO as an electron collector, possessing high charge mobility. This feature is attributed to its 2D structure, together with the conjugation of the π bond.

In a similar study, Singh *et al.*[347] investigated photocatalytic water splitting using rGO/TiO$_2$, which efficiently facilitated the conversion of solar energy into chemical energy through enhanced charge separation activity. The incorporation of GO in the hybrid material was found to reduce the band gap of the samples from 3.12 to 2.99 eV. Pure TiO$_2$ produced 173 μmol of H$_2$ with an H$_2$ production rate of 35 μmol h^{-1}, as observed in Fig. 16(g and h). The low photocatalytic activity observed for pure TiO$_2$ was attributed to the rapid recombination between core-bonded electrons and valence bond (VB) holes, facilitated by the generation of a large overpotential during H$_2$ generation. Upon incorporating GO, the H$_2$ production increased from 190 to 838 mmol, which was five times higher than that of pristine TiO$_2$. TiO$_2$–GO (1.0 wt%) exhibited the highest H$_2$ production rate of 168 μmol h^{-1}. Table 3 summarizes the results of CO$_2$ reduction and H$_2$ production using GO/TiO$_2$ photocatalysts. Serafin *et al.*[349] investigated the photoproduction of H$_2$ using rGO/TiO$_2$ under UV light irradiation in a gas phase system containing water and ethanol. The experimental findings demonstrated a notable enhancement in H$_2$ generation when TiO$_2$ was combined with rGO. Among the tested compositions, the rGO/TiO$_2$ composite calcinated at 700 °C showed the highest performance, achieving an H$_2$ photogeneration rate of 9.53 mmol h^{-1} g^{-1}. Similarly, Wang *et al.*[350] pursued a distinct methodology by fabricating an rGO/TiO$_2$ nanostructure, wherein TiO$_2$ nanorods were sandwiched between two rGO nanosheets for H$_2$ production. This nanostructure demonstrated enhanced H$_2$ photoproduction, achieving a rate of up to 800 μmol h^{-1} m^2, which was over 2.5 times higher compared to bare TiO$_2$. Chen *et al.*[351] developed a highly efficient photocatalyst for H$_2$ production by decorating TiO$_2$ NPs with nano-spherical-like rGO. The rGO/TiO$_2$ composite demonstrated a superior performance compared to bare TiO$_2$, achieving an H$_2$ production rate of 13 996 μmol g^{-1} h^{-1}, which was 3.45 times more efficient than TiO$_2$. The GO/TiO$_2$ nanocomposites used for H$_2$ production based on the literature are summarized in Table 3.

In conclusion, the photocatalytic reduction of CO$_2$ into valuable fuels and H$_2$ production are promising approaches to mitigate global warming and address the energy shortage. Research highlights the efficacy of rGO/TiO$_2$ nanocomposites in enhancing the CO$_2$ conversion, achieving methanol production rates of up to 2.33 mmol g^{-1} h^{-1}. These composites, prepared through techniques such as sonothermal–hydrothermal synthesis and electrochemical anodization, exhibit reduced band gaps (*e.g.*, 2.9 eV), which facilitate efficient CO$_2$ reduction into methanol, methane, and other hydrocarbons. In H$_2$ production, photocatalytic water splitting using GO/TiO$_2$ has emerged as a sustainable method. Enhanced charge separation and light absorption

have led to significant improvements in the H$_2$ generation rate, reaching up to 39.26 mmol g^{-1} h^{-1} catalyst. The incorporation of GO aids in electron transfer and minimizes the recombination losses, making these nanocomposites highly effective for both CO$_2$ reduction and H$_2$ generation. The summarized results indicate that optimizing the morphology and composition of TiO$_2$ significantly impacts its photocatalytic efficiency.

5.4. Photocatalysis-assisted organic synthesis

The use of photoactive materials as catalysts in organic synthesis has gained significant attention in recent years, driven by the growing demand for energy-efficient, environmentally friendly processes and the convenient accessibility of solar energy. Organic transformations are critical for numerous chemical and industrial applications, enabling the production of essential compounds such as alcohols, aldehydes, and amides. Photocatalysis using plasmonic noble metals offers an innovative approach for synthesizing these products. Traditional methods for organic transformations often rely on harsh conditions, such as elevated temperatures and high pressures. In contrast, photocatalysts facilitate a wide range of organic reactions, including hydrogenation, addition, decomposition, oxidation, and reduction, under mild and environmentally sustainable conditions.[363,364] Among the various photocatalysts, metal oxide semiconductors such as TiO$_2$ are recognized as efficient photocatalysts. When excited with energy greater than its bandgap, TiO$_2$ generates electron–hole pairs, which drive diverse redox reactions.[365] The incorporation of plasmonic metal NPs on TiO$_2$ further enhances the efficiency of these reactions, yielding high selectivity and improved product yields through radical generation. Additionally, GO has emerged as a promising heterogeneous carbocatalyst due to its large surface area, excellent thermal stability, moderate-to-strong acidity, and ease of recovery and reuse. These characteristics make GO a highly attractive option for sustainable and efficient organic transformations.[366]

In 2005, Tian and Tatsuma explored the oxidation potential of Au nanoparticle (Au NP)-supported TiO$_2$ for ethanol and methanol oxidation, leveraging the localized surface plasmon resonance (LSPR) properties of Au NPs.[367] Ohtani *et al.*[368] were the first to demonstrate the capability of TiO$_2$-supported Au NPs to oxidize isopropanol. They proposed a mechanism where the electrons transferred from the Au NPs to the TiO$_2$ CB reduce molecular oxygen, while the remaining holes on the Au NPs effectively oxidize isopropanol. The enhanced photocatalytic activity was attributed to light absorption driven by the LSPR of the Au NPs. A fascinating development in this field was reported by Xiao *et al.*,[369] who observed a light-induced switching in amine oxidation products using plasmonic Au nanorods (Au NRs) decorated on TiO$_2$ nanofibers under visible to near-infrared (VIS-NIR) light irradiation. Under these conditions, the plasmonic Au NRs/TiO$_2$ system demonstrated remarkable
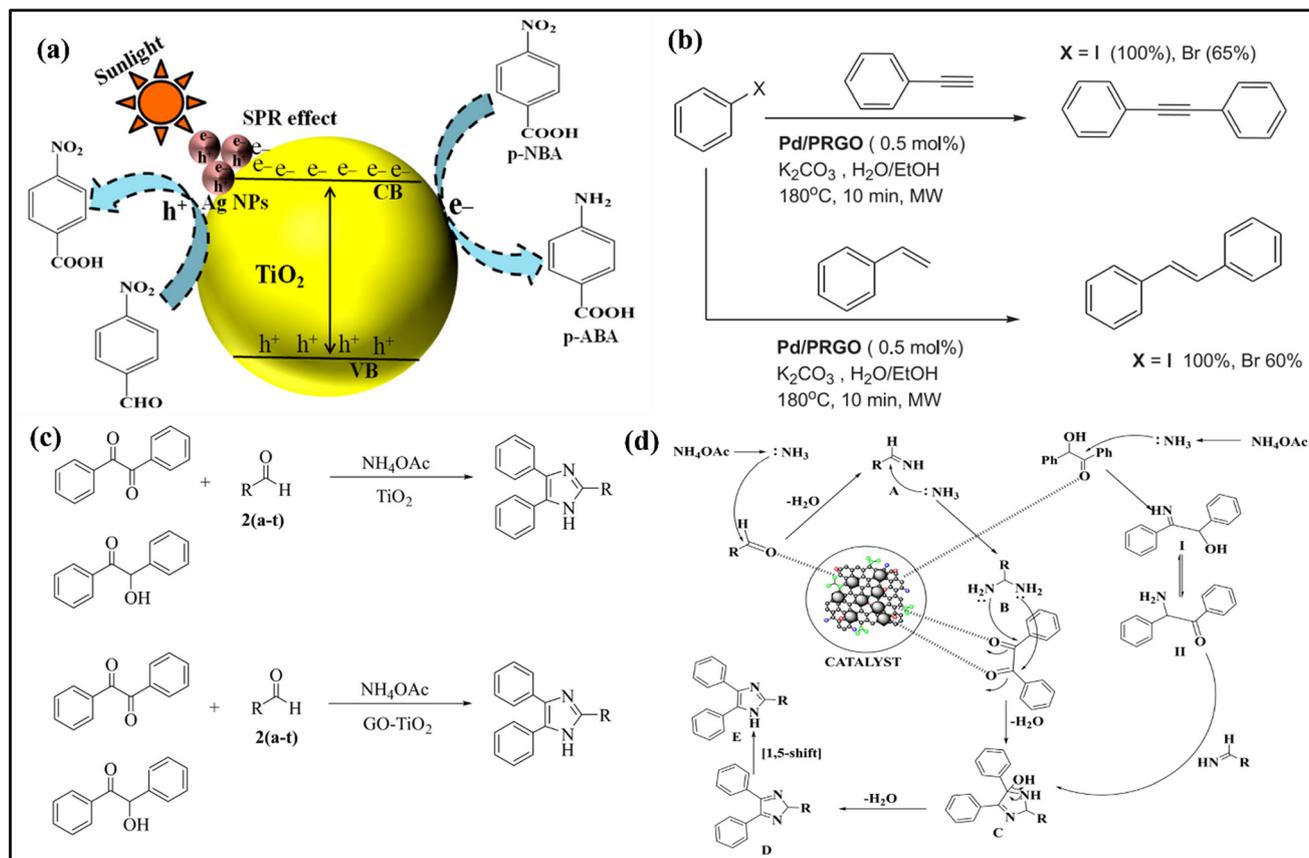
1738 | *Catal. Sci. Technol.*, 2025, **15**, 1702–1770

This journal is © The Royal Society of Chemistry 2025

Fig. 17 (a) Schematic of the mechanism of *p*-NBA reduction and *p*-NBAL oxidation with Ag–TiO$_2$. Reproduced with permission from ref. 370 Copyright (2020), Elsevier. (b) Heck and Sonogashira coupling reaction using Pd/rGO catalyst. Reproduced with permission from ref. 372 Copyright (2021), John Wiley and Sons. (c) Synthesis scheme of imidazole derivatives using TiO$_2$ and GO/TiO$_2$ catalyst. (d) Schematic of mechanism for the formation of 2,4,5-trisubstituted imidazole. Reproduced with permission from ref. 373 Copyright (2023), John Wiley and Sons.

activity for the solvent-free coupling of amines to imines using air as an oxidant. The selectivity for imines increased significantly under light irradiation, reaching approximately 80% compared to ~50% in the dark, while the selectivity for oximes decreased from ~49% in the dark to ~19% under light. This work highlights the potential of plasmonic photocatalysts in driving selective oxidation reactions under sustainable and mild conditions. The reduction of organic compounds is a crucial process for synthesizing chemically and industrially valuable products. Plasmonic materials have emerged as effective catalysts for these reduction reactions, enabling milder reaction conditions. Aulakh *et al.*[370] demonstrated the photo-induced reduction of *p*-nitrobenzoic acid (*p*-NBA) under UV and sunlight irradiation using plasmonic Ag–TiO$_2$ nanocomposites. The Ag–TiO$_2$ photocatalyst, synthesized *via* a photodeposition method, exhibited enhanced catalytic activity due to the formation of Ag nanodeposits (1–3 wt%) on TiO$_2$, which increased the hydrodynamic size of the composite by 1.5 to 2.7 times. Remarkably, 2 wt% Ag–TiO$_2$ achieved efficient *p*-NBA reduction under sunlight, while bare TiO$_2$ showed negligible activity. Fig. 17(a) depicts the mechanism of *p*-NBA reduction and *p*-nitrobenzaldehyde (*p*-NBAL) oxidation with Ag–TiO$_2$

under sunlight. In another study, Zhang and colleagues[371] reported the synthesis of porous TiO$_2$ hollow spheres loaded with plasmonic Au NPs for the reduction of 4-nitrophenol. Their nanohybrid system exhibited superior reactivity and selectivity compared to previously reported Au-mediated photocatalysts. The porous hollow structure of the TiO$_2$ spheres played a critical role in enhancing the photocatalytic performance by offering a high surface area for reactant adsorption and reducing the charge carrier recombination. These findings highlight the potential of plasmonic nanomaterials in achieving efficient and selective catalytic reductions under sustainable conditions.

TiO$_2$ has shown great potential as a catalyst for the demethylation of guaiacol, achieving a product selectivity of 50% catechol and 35% phenol, with hydrogenation identified as the primary reaction pathway. This activity is largely attributed to the Lewis acid properties of TiO$_2$.[374] When TiO$_2$ was employed as a support for a CoMoS catalyst, a significant improvement in the conversion rate was observed, alongside a shift in selectivity towards hydrodeoxygenation. This reaction predominantly yielded phenol, benzene, and cyclohexane as the major products. The enhanced hydrodeoxygenation tendency can be attributed to the larger

This journal is © The Royal Society of Chemistry 2025

Catal. Sci. Technol., 2025, **15**, 1702–1770 | **1739**

cluster size of the active phase, which weakens the interaction between the active phase and the TiO_2 support, thereby facilitating the desired reaction pathway.[375]

GO and its analogs are used to catalyze various organic transformations. Among these, Masteri-Farahani et al.[376] demonstrated the use of GO in biodiesel production. In their work, GO was surface-functionalized through silylation with (3-mercaptopropyl)trimethoxysilane, refluxed in dry toluene under a nitrogen atmosphere. The SH groups were oxidized to SO_3H acidic sites, resulting in GO–$PrSO_3H$. This catalyst was effectively employed for the esterification of acetic acid with butanol and oleic acid with methanol, showcasing excellent recyclability and reusability for up to five cycles. Gupta et al.[377] also developed a simple and rapid method for synthesizing tetrahydropyridine derivatives by reacting methylacetoacetate, 4-chlorobenzaldehyde, and aniline using recyclable GO as an efficient catalyst in CH_3CN as the solvent. The GO catalyst could be easily recovered by filtration and reused for up to five cycles without requiring regeneration, making this method eco-friendly and cost-effective. Soni et al.[378] further demonstrated the use of GO as a catalyst for synthesizing biscoumarin derivatives, achieving high to excellent yields in a short time frame. Additionally, palladium NPs supported on GO-based materials have recently gained prominence as highly effective catalysts for the synthesis of heterocyclic compounds. Heravi et al.[379] explored the application of palladium supported on GO (Pd/GO) as a catalyst for the Suzuki–Miyaura cross-coupling reaction. This reaction involved arylboronic acid, aryl halide, and K_2CO_3 as the base, using GO–PEG–imidazole–Pd (2.8×10^{-4} mol%) as the catalyst in water at 80 °C for 5–420 min. The authors systematically optimized the reaction conditions, including the amount of catalyst, base, and solvent, selecting 2.8×10^{-4} mol% of catalyst as the optimal concentration. Notably, the catalyst exhibited excellent reusability, being recycled and reused for up to seven runs. Moussa et al.[380] reported the synthesis and application of palladium NPs supported on reduced graphene oxide as a heterogeneous catalyst. This catalyst demonstrated an outstanding catalytic performance for a variety of coupling reactions, including Suzuki–Miyaura, Heck, and Sonogashira reactions, as shown in Fig. 17(b). In the Suzuki–Miyaura coupling, the catalyst exhibited remarkable recyclability, achieving an impressive turnover number (TON) of 7800 and turnover frequency (TOF) of 230 000 h^{-1}. These results underscore the potential of Pd-based GO materials in promoting efficient and sustainable catalytic processes for coupling reactions. Several reviews have highlighted the extensive research on the use of GO and its composites in organic synthesis.[366,372,381] These comprehensive studies cover a broad spectrum of applications, showcasing the versatility and effectiveness of GO-based materials in facilitating diverse organic transformations.

Although the literature on the use of GO/TiO_2 in organic synthesis is limited, the recent study by Samal et al.[373] introduced GO/TiO_2 as an effective catalyst for synthesizing imidazole derivatives. This innovative approach demonstrated excellent results, providing an eco-friendly and efficient method for the one-pot synthesis of 2,4,5-trisubstituted imidazole derivatives. This method offers numerous advantages, including mild reaction conditions, rapid reaction times, low catalyst loading, high productivity, improved atom economy, and broad substrate compatibility with both α-hydroxy ketones and 1,2-diketones. The reaction scheme is shown in Fig. 17(c). Among the catalysts tested, GO/TiO_2 outperformed TiO_2 alone in terms of catalytic efficiency. The optimization studies revealed that stirring the reaction mixture at 60 °C under ultrasonication for 18 min, with a 10 mol% catalyst loading in an ethanolic solvent system, yielded over 90% of the desired product. The proposed mechanism is outlined in Fig. 17(d). GO/TiO_2 facilitates the activation of carbonyl groups in the reactant. Ammonia, generated from ammonium acetate, reacts with substituted benzaldehyde to form imine intermediate (A), which is further converted into diamine intermediate (B). Intermediate (B) reacts with benzil to produce product C. Alternatively, benzoin reacts with ammonia to form intermediate (II), which then combines with intermediate (A) to yield product C. Finally, product C undergoes dehydration and a [1,5]-H-shift, leading to the formation of the desired product D. The reusability of the GO/TiO_2 catalyst was evaluated using a model reaction. After each reaction cycle, the catalyst was recovered by filtration, washed with ethanol/acetone, and dried at 80 °C. The recovered catalyst was weighed and reused for five consecutive runs without any significant loss in catalytic activity, demonstrating its excellent stability and sustainability. This study highlights the potential of GO/TiO_2 as a versatile and reusable catalyst for green and efficient organic synthesis.

In conclusion, the integration of photoactive materials, such as plasmonic noble metals, TiO_2, and GO, has significantly advanced the field of organic synthesis by providing sustainable and energy-efficient alternatives to traditional catalytic processes. These materials enable diverse organic transformations under mild conditions, reducing the need for harsh reaction environments, while delivering high selectivity and productivity. TiO_2 and its composites, particularly with plasmonic metals, have been proven to be effective in oxidation, reduction, and other critical reactions, while GO and its derivatives excel as heterogeneous catalysts due to their unique structural and chemical properties.

Recent developments, such as the use of GO/TiO_2 composites for synthesizing imidazole derivatives, underscore the growing potential of these hybrid materials. The ability to achieve high yields, excellent reusability, and eco-friendly reaction conditions highlight their importance in advancing green chemistry. The continued exploration of these innovative materials holds promise for expanding the scope of organic transformations, enhancing industrial applications and promoting sustainable chemical processes.

6. Graphene oxide/other metal oxides nanocomposites and their photocatalytic applications

In addition to TiO_2, metal oxides such as ZnO, WO_3, Fe_2O_3, CuO, and SnO_2, are regarded as nontoxic photocatalysts suitable for multifunctional applications due to their low cost, quick response, and fast recovery times. GO/ZnO composites, in particular, have demonstrated effective photocatalytic degradation of various pollutants, including dyes and organic compounds.[382–385] These composites have also been investigated for photocatalytic water splitting for H_2 production.[386] The inclusion of GO enhances electron–hole separation, thereby boosting the photocatalytic efficiency of ZnO. GO/WO_3 composites are highly effective for the degradation of pollutants under visible light. The narrow bandgap of WO_3 (2.4–2.8 eV), coupled with the electron-accepting properties of GO, enhances the photocatalytic activity. These composites also show promise in photoelectrochemical cells for solar energy conversion, benefiting from their improved charge transport and light absorption capabilities.[387–391]

Similarly, CuO is a p-type semiconductor with excellent optical and catalytic properties, possessing a low bandgap energy of around 1.2–1.7 eV.[392] GO/CuO composites exhibit significant activity for the photocatalytic degradation of pollutants, with GO improving the photocatalytic performance by reducing electron–hole recombination.[179,393–395] Additionally, these composites are being explored for electrochemical energy storage and conversion applications, such as in batteries and supercapacitors, due to their enhanced electrical conductivity and charge storage capacity.[396] Other nanocomposites, such as GO/SnO_2, GO/CeO_2, and GO/Fe_2O_3, are also widely used as photocatalysts for a variety of environmental and energy applications. Each type of these metal oxides has unique advantages and limitations. In some cases, combining them can minimize their limitations, and subsequently enhance their photocatalytic efficacy. Table 4 displays some examples of reported nanocomposites of GO derivatives with other metal oxides, highlighting their targeted pollutants and energy production applications.

7. Computation aspects of GO, TiO_2 and GO–TiO_2 nanocomposites in describing their photocatalytic applications

As discussed above, TiO_2, GO and their nanocomposites have extensively been investigated experimentally for various photocatalytic applications. In addition, these materials have been studied theoretically to understand their physiochemical properties influencing their surface, optical and electrical properties, which contribute to their photocatalytic activities. Density functional theory (DFT) stands as a powerful computational method that has revolutionized research across condensed matter physics, quantum chemistry, and materials science. At its fundamental core, DFT provides a sophisticated theoretical framework for calculating electronic structures, with a primary focus on ground state electron density.[418] This approach offers a computationally efficient and flexible means of approximating complex many-body electron problems in both the ground and excited states.[419] In the realm of materials research, DFT has emerged as an especially transformative tool for studying metal oxides, enabling scientists to investigate property enhancements through strategic methodological approaches, such as doping with metal and nonmetal elements, creating oxygen vacancies, and forming heterojunctions by coupling with other semiconductors. For instance, Ikram et al.[420] studied the effect of Ba doping on altering the electronic and optical properties of TiO_2. The crystalline atomic structure of anatase TiO_2 and Ba-TiO_2 was modeled by a $2 \times 2 \times 2$ supercell, as shown in Fig. 18(a). The partial density of states (PDOS) for pure TiO_2 (shown in Fig. 18(b)) revealed that the VB was predominantly composed of O 2p states, while the CB was primarily characterized by Ti 3d states. However, the electronic structure was changed in Ba-TiO_2, creating a slightly asymmetric DOS near the VB, as shown in Fig. 18(c). Notably, in-gap states emerged within the band gap, with a prominent peak in the minority spin DOS near the upper VB. This modification also shifted the VB edge closer to the Fermi level, suggesting an increased charge-carrier concentration and a slight reduction in the band gap. The findings suggested that Ba-doped TiO_2 exhibited an enhanced photocatalytic performance due to their modified electronic structure, which allows for better utilization of visible light in photocatalytic applications. Similarly, Pan et al.[421] explored how noble metals can enhance the catalytic activity of anatase TiO_2 for H_2 evolution. The structural model of H-doped TiO_2 and noble metal-doped TiO_2 is shown in Fig. 18(d). According to the comparison of different noble metal dopants, the researchers found notable variations in their thermodynamic stability. Silver (Ag)- and gold (Au)-doping proved to be more thermodynamically stable compared to platinum (Pt)-, palladium (Pd)-, and ruthenium (Ru)-doping. The band structures of noble metal-doped TiO_2 (Fig. 18(e)) clearly show that the introduction of dopants reduces the bandgap of TiO_2.

Using first-principles DFT calculations, Tian and Liu et al.[423] demonstrated that sulfur-doped anatase TiO_2 introduces an S 3p hybrid energy level within the forbidden band, causing an upward shift in the VB and a reduction in the bandgap. This bandgap narrowing results in a redshift in the absorption spectrum, which becomes more pronounced as the dopant concentration increases. Similarly, using first-principles Hartree–Fock calculations, Karvinen et al.[424] analyzed a supercell system with atomic clusters to investigate the electronic properties of various metal cations doped in TiO_2. Their findings revealed that doping V^{3+}, Mn^{3+},

Table 4 GO as a co-catalyst with metal oxide other than TiO_2 for multifunctional applications

Photocatalyst (metal oxide morphology)	Dye conc./solvent/sacrificial agent	Catalyst amount	Applications	Irradiation source	Time	Efficiency	Ref.
GO/ZnO (polygon)			MB degradation	100 W mercury vapor lamp	22 min	98.4%	174
GO/ZnO (thin films)			MB degradation	300 W tungsten halogen bulb	150 min	89%	173
GO/ZnO (thin films)			Phenol degradation	300 W tungsten halogen bulb	150 min	72%	173
GO/ZnO (nanorods, hexagons, and nanosphere)			MG, CV, and MG + CV degradation	Simulated light	180 min	77.46%, 33%, and 96.72%	175
GO/ZnO (NPs)			RhB degradation	Visible light	85 min	97.7%	176
GO/ZnO (NPs)			MB degradation	UV light	180 min	98%	177
rGO/ZnO (hexagonal tube)			MO and RhB degradation	Halogen lamp (500 W)	30 min	93.51% and 95.23%	164
rGO/ZnO (nanorods)	50 mL of 5 ppm	3 mg	MO degradation	UV light	360 min	99%	397
rGO/ZnO (nanorods)	5 ppm	100 mg	RhB degradation	UV light	20 min	94%	398
rGO/ZnO (nanorods)	5 ppm	100 mg	4-Chlorophenol degradation	UV light	60 min	94%	398
rGO/ZnO (nanorods)	1.5×10^{-5} mol L^{-1}	—	RhB degradation	UV light	45 min	100%	399
rGO/ZnO (nanosheet)	50 mL of 40 mg L^{-1}	20 mg	MB degradation	Visible light	80 min	100%	400
GO/ZnO (nanorods)	50 mL of 40 ppm	50 mg	MB degradation	Sunlight	40 min	89%	178
GO/ZnO (NPs)	100 mL of 0.015 g L^{-1}	20 mg	MB degradation	50 W high-pressure mercury lamp	90 min	97.6%	401
GO/CuO (rectangular)	20, 40, 60, and 80 ppm	0.002–0.008 mg	MR degradation	Sunlight	90 min	94%	179
GO/CuO (NPs)	50 mL of 20 mg L^{-1}	20 mg	MB degradation	Visible light	60 min	83.20%	180
rGO/CuO (NPs)	50 mL of 2.23×10^{-5} M	10 mg	CR and MB degradation	100 W Xe lamp	60 min	95.6% and 77.5%	181
rGO/WO$_3$ (nanosheet)	100 ml of 1 mg L^{-1}	10 mg	RhB degradation	Sunlight	270 min	85%	182
rGO/WO$_3$ (nanoflower)	20 ppm	40 mg	MB degradation	UV light	120 min	81.56%	183
rGO/WO$_3$ (nanorods)	100 mL of 2×10^{-5} M	20 mg L^{-1}	RhB degradation	Visible light	120 min	94%	402
rGO/WO$_3$ (nanorods)	100 mL of 2×10^{-5} M	20 mg L^{-1}	Ciprofloxacin degradation	Visible light	120 min	90%	402
Indigo-RGO/WO$_3$ (nanosphere)	100 mL solution of 10 ppm	20 mg	MB degradation	Sunlight	120 min	80.41%	403
GO/α-Fe$_2$O$_3$ (nanosphere)	50 mL of 10 mg L^{-1}	5 mg	MB degradation	UV light	90 min	90%	404
rGO/SnO$_2$ (NPs)	1×10^{-5} M	1 mg mL^{-1}	MO degradation	UV light	60 min	84%	405
rGO/ZnO (NPs)	—	—	PEC water splitting	Solar irradiation	—	430 μA cm^{-2} (at 1.23 V *vs.* RHE)	406
rGO/Fe$_3$O$_4$ (NPs)	—	—	PEC water splitting	Solar irradiation	—	280 μA cm^{-2} (at 1.23 V *vs.* RHE)	406
rGO/ZnO (nanorods)	—	—	PEC water splitting	Solar irradiation	—	10 mA cm^{-2} (*vs.* RHE)	407
rGO/ZnO (single crystal)	—	0.2 mg mL^{-1}	PEC water splitting	White light irradiation	—	65 μA cm^{-2} (*vs.* Ag/AgCl)	408
rGO/ZnO (nanorods)	—	—	PEC water splitting	UV light	—	0.6 mA cm^{-2} (*vs.* Ag/AgCl)	409
GO/ZnO (triangles)	—	—	PEC water splitting	UV light	—	1.517 mA cm^{-2} (at 1.45 V *vs.* RHE)	410
GO/CuO (spongy ball)	Methanol solution	40 mg	H$_2$ production	UV-vis light	—	19.2×10^3 μmol h^{-1} g^{-1}	411
GO/Cu$_2$O (nanosphere)	10 vol% methanol aqueous solution	30 mg	H$_2$ production	Visible light	—	118.3×10^3 μmol	412
GO/ZnO (NPs)	—	—	CO$_2$ reduction to methanol	UV-vis light	180 min	263.17 μmol g$_{cat}^{-1}$	413
rGO/Cu$_2$O (rhombic dodecahedra, octahedral and cubic)	50 mL of water	25 mg	CO$_2$ reduction to methanol	Visible light	1200 min	355.3 μmol g^{-1} cat	414
GO/Cu-TiO$_2$ (nanosheet)	—	—	CO$_2$ reduction to methane and acetone	Visible light	—	12.09 and 0.75 μmol h^{-1} g$_{cat}^{-1}$	415

1742 | *Catal. Sci. Technol.*, 2025, **15**, 1702–1770

This journal is © The Royal Society of Chemistry 2025

Table 4 (continued)

Photocatalyst (metal oxide morphology)	Dye conc./solvent/sacrificial agent	Catalyst amount	Applications	Irradiation source	Time	Efficiency	Ref.
Ag/rGO–ZnO (nanorods)	Water	100 mg	CO_2 to CO and CH_4	UV-vis	—	62.7 μmol g^{-1} h^{-1}	416
rGO/Cu$_2$O (NPs)	—	—	CO_2 reduction to methanol	Visible light	24 h	862 μmol g^{-1}	417
rGO/CuO (nanorods)	—	—	CO_2 reduction to methanol	Visible light	24 h	1228 μmol g^{-1}	417

Cr^{3+}, and Fe^{3+} ions into anatase TiO_2 significantly narrows the bandgap, whereas V^{3+} and Fe^{3+} ions have a minimal impact on the bandgap size in rutile TiO_2. Moreover, the incorporation of these metal ions extends the light absorption range into the visible spectrum, enabling TiO_2 to exhibit a strong response to visible light. Yang et al.,[425] using DFT-based theoretical calculations, studied the photodeposition of Au and Ru metal clusters as cocatalysts on the surface of anatase TiO_2 (101) and their role in enhancing photocatalytic activity. The synthesized Ru/TiO$_2$ and Au/TiO$_2$ composites exhibited excellent HER activity, which was attributed to their strong interfacial chemical bonds that act as electron traps, facilitating the capture of photoinduced electrons. Further, to address the low HER efficiency of TiO_2, Zhuang et al.[426] used first-principles simulations to investigate the performance of TiO_2 loaded with non-noble metal Ni. They found that Ni clusters preferentially aggregate on the (101) crystal plane of TiO_2 due to the structural differences between the crystal planes. The Ni clusters improve the photogenerated carrier separation, introduce interstitial states in the bandgap of TiO_2, and elevate the Fermi level, significantly enhancing the HER efficiency. Electrochemical calculations further identified O_{2c} atoms near Ni clusters as the active HER sites, with Ni loading notably reducing the Gibbs free energy of HER. Additionally, ternary narrow bandgap semiconductors have gained attention for increasing the absorption of visible light by TiO_2. Pillai et al.[422] synthesized an AgBiS$_2$–TiO$_2$ heterojunction photocatalyst via a solvothermal method, demonstrating that coupling AgBiS$_2$ with TiO_2 broadens its visible light absorption and decreases its bandgap. The electronic and optical properties of AgBiS$_2$ and TiO_2 were studied using DFT. The band structure and the partial density of states (PDOS) of TiO_2 and AgBiS$_2$ are shown in Fig. 18(f and g), respectively. TiO_2 exhibited an indirect band gap of approximately 2.7 eV. Its VBM was located between its Z and P k-points, while its CBM was situated between its Γ and X k-points in the reciprocal space. The upper valence band (UVB) was primarily composed of O p-states, and the lower conduction band (LCB) was mainly dominated by Ti d-states, with the Ti p-states also present near the UVB. Alternatively, the calculated band structure and PDOS for AgBiS$_2$ showed an indirect band gap of about 0.7 eV. The VBM was found between the H and A k-points, while the CBM was positioned between the Γ and A k-points in the

Brillouin zone. The electronic states around the UVB were attributed to the AgS$_4$ tetrahedra, and that near the LCB corresponded to the electronic states of the BiS$_6$ octahedra. The UVB is dominated by S p-orbitals and Ag d-orbitals, while the LCB is primarily influenced by Bi and S p-states. As previously noted, the forbidden transitions suggest that the actual energy required for electrons to transition from the VB to the CB will exceed the computed band gap. Under visible light, the photocatalytic H_2 production by the AgBiS$_2$/TiO$_2$ composite was 1000 times higher than that of pure TiO_2, showcasing its potential for solar-driven H_2 production.

Recently, Allam et al.[427] utilized DFT to predict the photocatalytic performance and analyse the competitive adsorption in aqueous-phase reactions. Their study integrated a comprehensive experimental inhibition assay with DFT and machine learning (ML)-enhanced explicit solvation simulations to evaluate the predictive ability of the calculated interaction energies in photocatalytic inhibition. Computational methods were employed to investigate the inhibitory effects of a series of small organic molecules on the TiO_2 photocatalytic degradation of para-chlorobenzoic acid (pCBA). Their study focused on tryptophan, coniferyl alcohol, succinic acid, gallic acid, and trimesic acid as interfering agents, examining their impact on competitive reaction kinetics through both bulk and surface phase interactions. The DFT results revealed a strong correlation between the interaction energies of anatase surfaces and various inhibitory molecules, aligning with experimental observations from probe–quencher competition studies. This analysis highlighted that the adsorption site interactions played a dominant role than general reactivity with OH· radicals. The DOS analysis provided valuable insights into the surface interactions between TiO_2 and adsorbate molecules. Although the addition of pCBA to the surface did not alter the TiO_2 electronic states, most inhibitory molecules (except trimesic acid) formed new electronic states below the Fermi level with varying densities. Trimesic acid displayed a high density of states near the Fermi level, similar to pCBA, aligning with its strong surface site competition observed experimentally. Other molecules, such as coniferyl alcohol, tryptophan, succinic acid, and gallic acid, introduced distinct interaction states, influencing the adsorption affinity trends. The width of the gap (ΔE) between the Fermi level and the VBM correlated with the inhibitory effects, where coniferyl alcohol created the largest ΔE, followed by tryptophan,
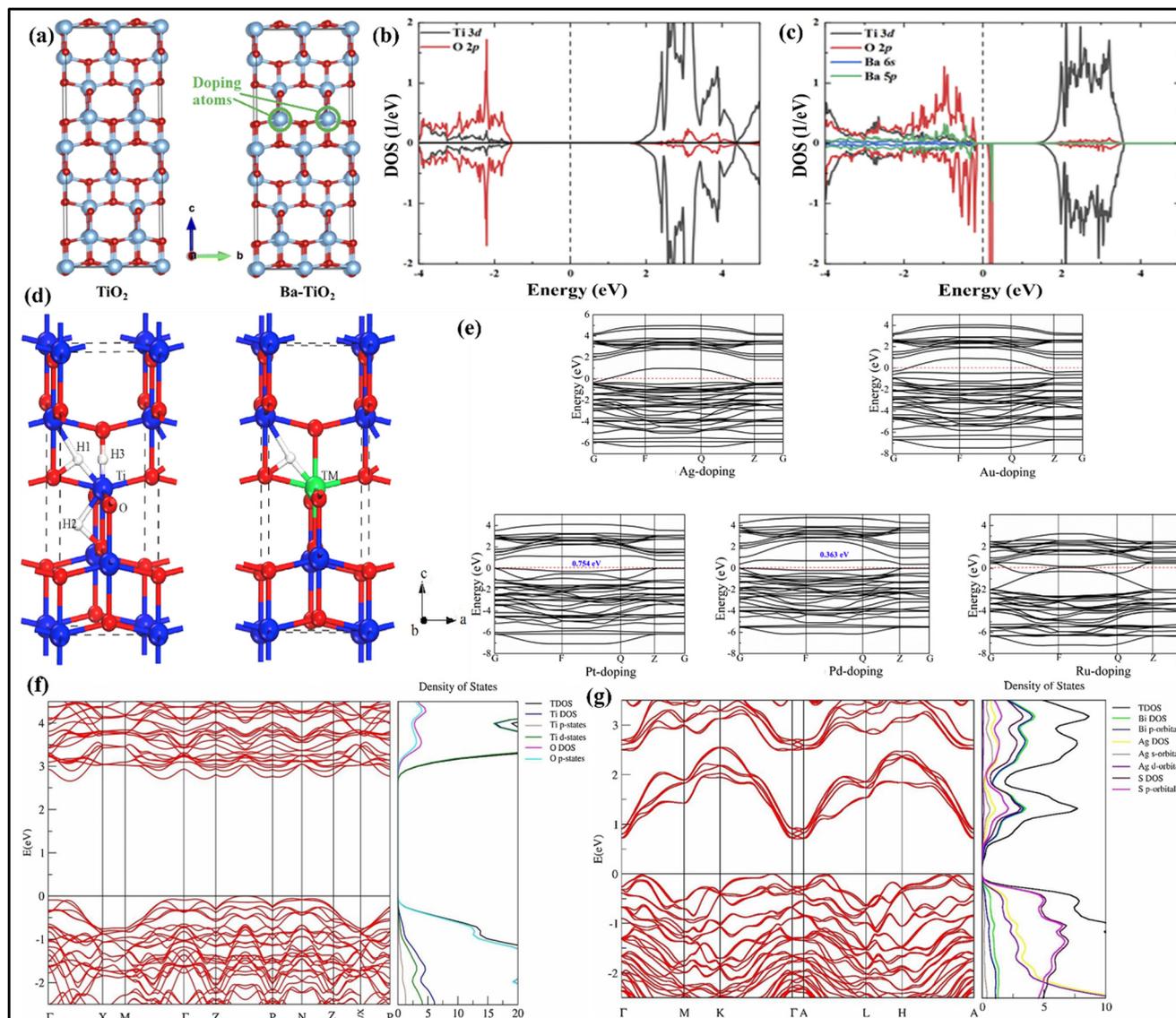
This journal is © The Royal Society of Chemistry 2025

Catal. Sci. Technol., 2025, **15**, 1702–1770 | **1743**

Fig. 18 (a) Computational model for the anatase TiO_2 and Ba-doped TiO_2 and PDOS of (b) TiO_2 and (c) Ba-doped TiO_2.[420] Copyright (2022), the Royal Society of Chemistry. (d) Structural model for H-occupied mechanism and noble metal-doped TiO_2. (e) Calculated band structure in the Brillouin zone of doped TiO_2. Reproduced with permission from ref. 421 Copyright (2018), Elsevier. (f and g) Calculated electronic structure and PDOS of TiO_2 and $AgBiS_2$. Reproduced with permission from ref. 422 Copyright (2019), Elsevier.

succinic acid, and gallic acid. Gallic acid, despite having tightly grouped states near the Fermi level, ranked lower than trimesic acid in adsorption affinity. These trends in ΔE and electron density aligned well with the experimental observations and calculated interaction energies, confirming the approximate adsorption hierarchy of pCBA ≈ trimesic acid > gallic acid > succinic acid > tryptophan > coniferyl alcohol. Additionally, ML-accelerated solvation simulations showed that water molecules saturated the active sites of anatase, suggesting that inhibitory cosolvents and probes not only compete with each other but also with water for adsorption on the TiO_2 surface. Moreover, molecules with multiple functional groups, such as trimesic acid, demonstrated stronger adhesion to TiO_2, significantly inhibiting photocatalytic activity.

Similarly, DFT studies have been utilized to investigate GO, uncovering its potential and versatile role in photocatalytic applications. Dabhi et al.[428] conducted a comprehensive investigation into the structural, electronic, and vibrational properties of GO using DFT, focusing on the intricate relationships between epoxy and hydroxyl functional groups. Their study meticulously examined the geometrical structures of GO with various functional group configurations across different unit cell sizes and oxygen densities. Fig. 19(a) comprehensively illustrates the structural variations, presenting both top (XY plane) and perspective views of GO models with distinct functionalization patterns. The findings of their study revealed that the electronic properties of GO can be significantly tuned by altering its functional groups and oxygen density, as shown in Fig. 19(b). Specifically, the structure of
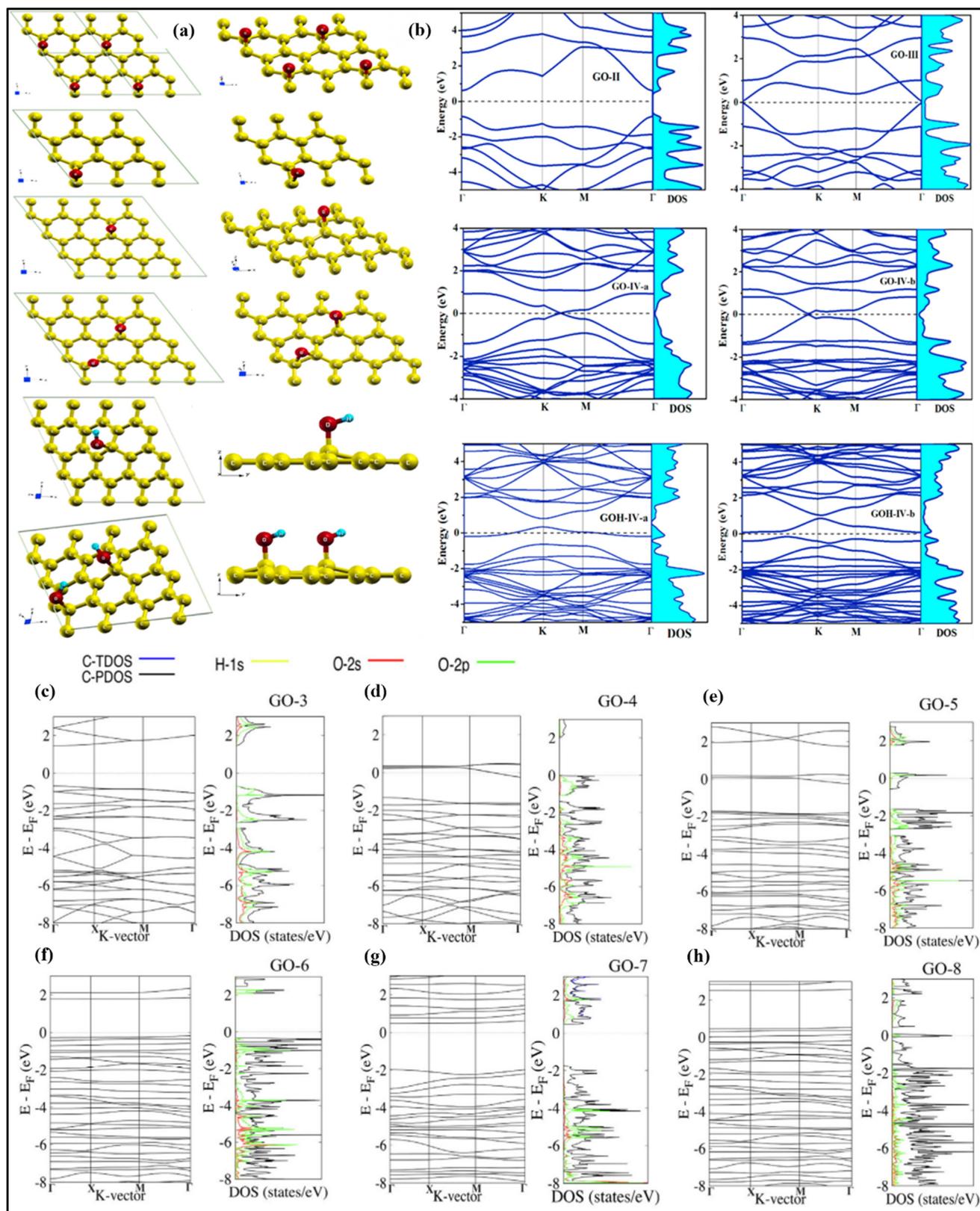
1744 | Catal. Sci. Technol., 2025, 15, 1702–1770

This journal is © The Royal Society of Chemistry 2025

Fig. 19 (a) Structure in *XY* plane and perspective view of epoxy group on different unit cells on GO. (b) Electronic band structure together with total density of states of different unit cell on GO. Reproduced with permission from ref. 428 Copyright (2017), Elsevier. (c–h) DOS, PDOS and band structure of different GO models. Reproduced with permission from ref. 429 Copyright (2017), Elsevier.

This journal is © The Royal Society of Chemistry 2025

Catal. Sci. Technol., 2025, **15**, 1702–1770 | **1745**

GO, which contains one epoxy group and has an oxygen-to-carbon (O/C) ratio of 12.5%, exhibits a direct band gap of 1.48 eV, indicating semiconducting behaviour. In contrast, other structures with varying O/C ratios (ranging from 3.125% to 6.25%) displayed semi-metallic characteristics, with the Dirac point shifting in relation to the functional groups. The study also highlighted that as the O/C ratio increases, the C–O bond length increases, while the C–C bond length decreases, demonstrating a structural transformation that correlates with electronic changes. Phonon dispersion calculations confirmed the dynamic stability of all the considered GO models, given that no imaginary phonon modes were detected throughout the Brillouin zone. The results underscore the potential for engineering the electronic properties of graphene oxide through careful control of its functionalization and oxidation levels, which can have significant implications for its application in electronic devices and catalysis. In a similar study, Celaya et al.[429] explored the computational aspects of GO, investigating its potential photocatalytic activity through advanced theoretical methodologies. Employing DFT, these researchers meticulously modelled various GO configurations by systematically incorporating different concentrations of epoxy and hydroxy functional groups onto a pristine graphene layer. The DFT calculations unveiled remarkable transformations in the electronic structure of GO. Fig. 19(c–h) illustrate the DOS, projected DOS, and band structures for various GO systems under study, as follows: (c) GO containing 25% epoxy groups (GO-3); (d) GO containing 25% hydroxyl groups (GO-4); (e) GO with a combination of 12.5% hydroxyl groups and 12.5% epoxy groups (GO-5); (f) GO containing 50% epoxy groups (GO-6); (g) GO with a mixture of 19% hydroxyl groups and 25% epoxy groups (GO-7); and (h) GO with 8% hydroxyl groups, 4% epoxy groups, and 4% carboxyl groups (GO-8). The pristine graphene layers exhibited a non-semiconducting nature, with no states present at the Fermi level. However, functionalization with groups such as epoxy, hydroxyl (–OH), and carboxyl led to significant changes in their electronic structure, transforming this material into a semiconductor. GO systems with epoxy groups (GO-3 and GO-6) displayed strong chemisorption, with adsorption energies of −9.50 and −16.27 eV, and cohesion energies of −6.64 and −5.81 eV, respectively. These modifications resulted in band gap formation, given that the epoxy groups blocked the p-orbital contributions near the Fermi level.

Hydroxyl-functionalized GO (GO-4) also exhibited semiconducting behavior, which was attributed to the opening of the band gap. Furthermore, combining epoxy and hydroxyl groups (GO-5) increased the band gap to approximately 2 eV, consistent with previous studies. In contrast, GO with a moderate mixture of epoxy and hydroxyl groups (GO-9) exhibited metallic-like characteristics due to the weak interactions between the functional groups and the graphene substrate. Tridimensional graphene systems, such as the zigzag and armchair configurations (GO-10 and 11), also showed band gap formation, with the armchair configuration yielding a larger band gap of 3.2 eV. Several functionalized GO models, including those with hydroxyl, epoxy, and their mixtures (GO-4, 6, 7, 10, and 11), were identified as having high photocatalytic potential, making them promising candidates for applications such as CO_2 reduction. These systems benefit from modifications in their electronic structure, which facilitate efficient charge separation. The HOMO–LUMO analysis revealed that GO-4, GO-6, and GO-7 exhibit a separated HOMO (localized on carbon atoms) and LUMO (localized on oxygen atoms), promoting effective electron–hole pair separation crucial for photocatalysis. In contrast, GO-3, GO-5 AND GO-8 with overlapping HOMO and LUMO contributions show a reduced efficiency in electron–hole separation. The charge density difference analyses further illustrated how functional groups induce charge transfer to the graphene layer, leading to band gap opening and a transition from a non-semiconducting to a semiconducting state. Depending on the functional groups used, GO systems exhibited either direct or indirect band gaps. These results highlight the potential of functionalized GO systems to tailor their electronic properties for advanced applications, particularly in photocatalysis and CO_2 reduction. Notably, these theoretical predictions were rigorously validated through experimental characterization of the synthesized GO. The UV-vis absorbance and work function measurements demonstrated remarkable alignment with the computational models.

In another study, Nasehnia et al.[430] investigated the optical properties of oxygen-functionalized GO and partially oxidized graphene using DFT. These researchers found that oxygen atoms chemically bonded to the graphene plane, forming epoxide groups, which transformed the optical characteristics of the material. By employing the random phase approximation, they derived the complex dielectric function and calculated key optical parameters across the infrared, visible, and UV spectral regions. Systematic exploration of oxygen-to-carbon (O/C) ratios ranging from 2% to 50% unveiled significant transformations in the optical properties of the materials. The absorption coefficients demonstrated a marked increase with higher O/C ratios, particularly in the UV region, indicating enhanced light absorption as the oxidation levels increased. Thus, this study highlighted that controlling the degree of oxidation allows the tailoring of the electronic density of states and band gap of GO, presenting opportunities to optimize its charge transport and light absorption for photocatalytic applications.

GO has emerged as a promising material for enhancing the photocatalytic activity under sunlight irradiation, offering innovative pathways for designing materials aimed at diverse environmental applications. As highlighted in the preceding sections, the integration of GO with metal oxides such as TiO_2 and ZnO significantly improves their photocatalytic efficiency. This synergistic combination enhances the charge separation, extends the light absorption into the visible spectrum, and ultimately increases the overall productivity in photocatalytic processes.

Gillespie et al.[431] developed models of TiO_2 rutile (110)/rGO interfaces incorporating various oxygen functional groups characteristic of rGO. Using hybrid density functional
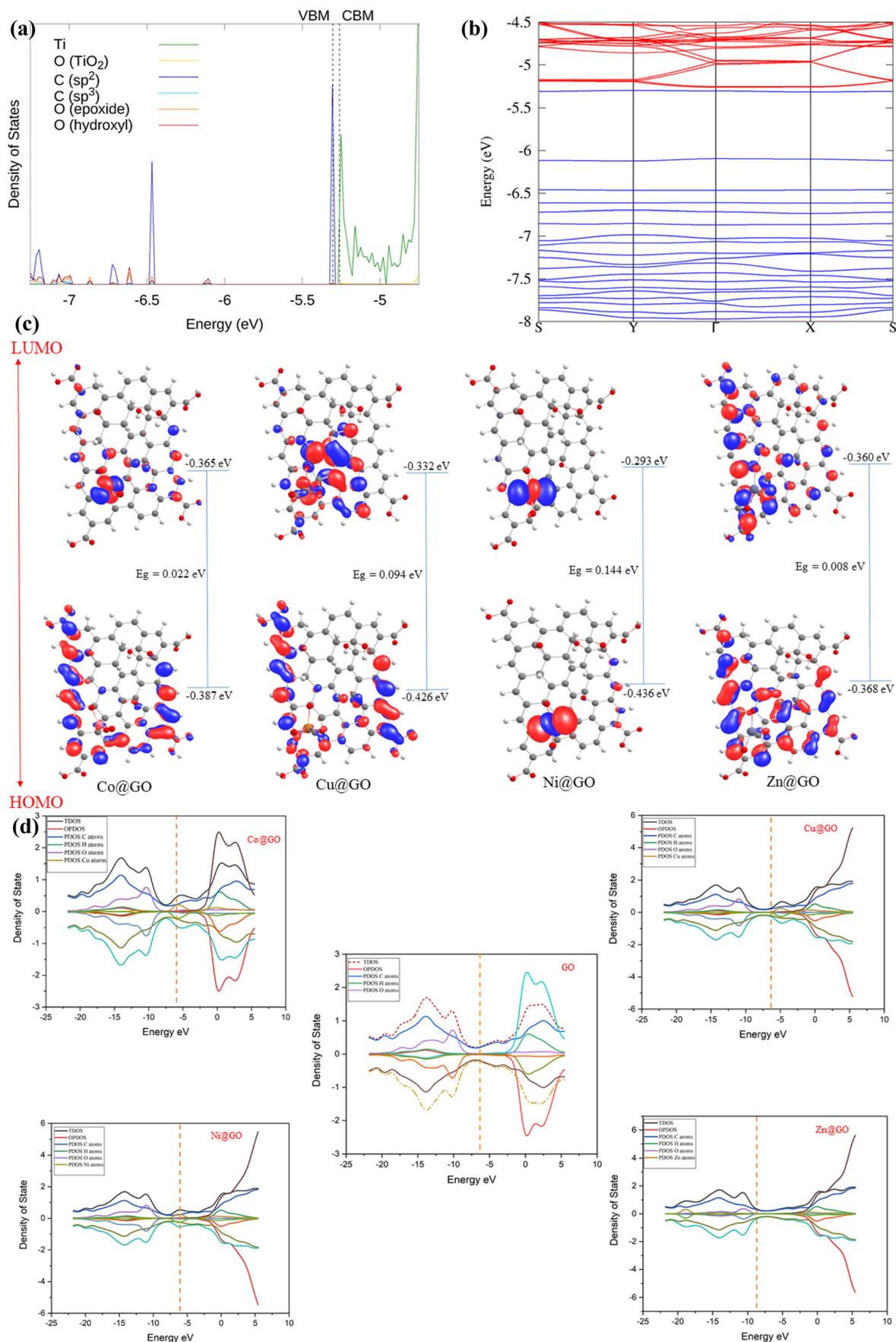
1746 | Catal. Sci. Technol., 2025, **15**, 1702–1770

This journal is © The Royal Society of Chemistry 2025

Fig. 20 (a) DOS spectrum of GO/rutile (110) TiO$_2$. (b) Band structure of GO/rutile (110) TiO$_2$.[431] (c) Iso-surface HOMO and LUMO and (d) visualization of the density of states for CoO@GO, CuO@GO, NiO@GO and ZnO@GO.[432]

This journal is © The Royal Society of Chemistry 2025

Catal. Sci. Technol., 2025, **15**, 1702–1770 | **1747**

theory (HSE06) calculations, they investigated the impact of oxygen functional groups and interfacial cross-links, such as Ti–O–C covalent bonds and strong H-bonds, on the electronic properties of rGO and rGO-based composites. These interactions were found to play a critical role in shaping the electronic structure and potential photocatalytic efficiency of these composites. The DOS spectra and band structure, as shown in Fig. 20(a and b), indicated that GO within this composite retained an electronic structure akin to that of an isolated molecule, with discrete occupied GO levels appearing within the TiO_2 bandgap. In particular, the HOMO of GO is positioned just below the CBM of rutile (110). This alignment arises from the intrinsic electronic structures of the isolated GO and rutile components. Despite the narrow or nearly zero bandgap suggested by this alignment, the composite exhibited semiconducting rather than metallic behavior. Its HOMO consists predominantly of π orbitals from sp^2 carbon atoms, while its corresponding π^* orbital is approximately 2.1 eV higher in energy, embedded deep within the TiO_2 CB. Interestingly, the GO/rutile (110) composite lacked cross-links or strong interfacial interactions, such as Ti–O–C covalent bonds. Without this strong coupling, mixed TiO_2/GO electronic states are not formed, reducing the likelihood of charge transfer excitations. Although visible-light excitation of GO may theoretically inject electrons into the rutile (110) CB as a subsequent step, the weak interactions between GO and rutile (110) will likely result in slow charge transfer rates. Consequently, this specific interfacial binding arrangement is unlikely to facilitate enhanced light absorption, efficient charge separation, or improved photocatalytic activity compared to pure TiO_2.

Further, to investigate the electronic properties of rGO/TiO_2 composites, various interfacial binding configurations were compared including the hydrogen-bonded 12H-rGO/rutile (110) structure, the cross-linked hydrogen-bonded 12H-rGO/rutile (110) structure, and the covalently bonded 12C-RGO/rutile (110) structure. This study revealed that the formation of cross-links, such as Ti–O–C and Ti–O–H⋯O–C bonds between rGO and TiO_2, is a crucial factor for achieving strong interfacial binding in the composite. Additionally, hydrogen bonding was identified as a significant component of the interfacial interactions. However, it was found that higher concentrations of oxygen functional groups do not necessarily facilitate the formation of interfacial hydrogen bonds. In fact, in systems with very high oxygen functional group concentrations, such as GO/rutile (110), these groups tend to engage in non-interfacial hydrogen bonding within the GO itself, rather than participating in interfacial interactions. The binding energy trends further support that some oxygen functional groups, such as epoxide oxygen, which do not participate in interfacial binding, slightly weaken the overall interaction at the interface. Analysis of the electron density difference in the 12H-rGO/rutile (110) composite confirmed that the weakening effect of non-binding epoxide groups is due to their tendency to withdraw electron density from the hydroxyl groups involved in the cross-linking, as well as the

associated sp^3 carbon atoms. Importantly, it was demonstrated that covalent bonding, through Ti–O–C and Ti–O–H⋯O–C interactions, leads to the formation of a new unoccupied band primarily localized on rGO, situated below the CB of TiO_2. This rGO-based lowest unoccupied band, consistently observed in strongly bound rGO/TiO_2 composites, plays a critical role in enhancing the photocatalytic efficiency. The energy profile of this band favors the trapping of photoexcited electrons, reducing the charge carrier recombination and prolonging the excited state lifetime. Furthermore, the energy of this band allows the visible-light excitation of electrons directly from the occupied rGO bands into the lowest unoccupied band. Additionally, electrons from the occupied rGO bands with significant oxygen character may be excited to the TiO_2 CB through orbital overlap with the TiO_2 terminus of the interfacial cross-link, and subsequently decay into the lowest unoccupied rGO band. The presence of higher unoccupied rGO bands also facilitates photosensitization, contributing to improved photocatalytic activity.

Recently, Mbonu et al.[432] investigated the effects of transition metal oxides CoO, CuO, NiO, and ZnO on the electronic properties, structural characteristics, and quantum capacitance of GO nanosheets using DFT computations. This study aimed to provide insights into designing GO-based supercapacitors with high energy density. To understand the stability and reactivity of the studied interactions (CoO@GO, CuO@GO, NiO@GO, and ZnO@GO), the frontier molecular orbital (FMO) theory was applied. This approach involves analyzing the HOMO, the LUMO, the energy gap, and quantum chemical descriptors. The bare GO surface exhibited HOMO and LUMO energy levels of −0.185 eV and −0.179 eV, respectively, with an energy gap of 0.138 eV. Upon interaction with the metal oxides, changes in the energy gap were observed. Specifically, the energy gap decreased slightly for CuO@GO (0.094 eV), CoO@GO (0.022 eV), and ZnO@GO (0.008 eV). However, in the case of NiO@GO, the energy gap increased to 0.144 eV. These results suggest that the NiO@GO interaction demonstrates greater stability due to its higher energy gap. To further elucidate the interactions, isosurface visualizations of the HOMO and LUMO were generated, providing detailed insights into the atomic distributions. These visualizations, as presented in Fig. 20(c), offer a clearer understanding of the electronic properties and structural changes induced by metal oxide doping.

To analyze the distribution of all available quantum states per unit energy in a molecule, the DOS function was utilized. Fig. 20(d) highlights the DOS properties of the investigated systems, including the total density of states displayed at the top of the plots and the partial density of states representing the individual components of pristine and doped graphene oxides. The DOS plots reveal a symmetrical pattern in the alpha and beta spin orbitals for both pristine and doped graphene oxides, regardless of their magnetic properties. The dopant metal oxides CuO, CoO, NiO, and ZnO emerge as key contributors to the energy states near the Fermi level. Among them, CuO and CoO show the most pronounced changes,

1748 | Catal. Sci. Technol., 2025, 15, 1702–1770

This journal is © The Royal Society of Chemistry 2025

characterized by strong peaks close to the Fermi level due to the high-energy states of Cu and Co. Moreover, all the transition-metal-doped graphene systems exhibit a significant accumulation of density of states around the Fermi level. This accumulation plays a crucial role in the observed enhancement of quantum capacitance, which is directly correlated with the electron density near the Fermi energy level. An investigation into the quantum capacitance revealed a slight increase in the quantum capacitance of the studied graphene oxide. The doped systems followed the order of ZnO@GO > NiO@GO > CoO@GO > CuO@GO. This indicates that ZnO doping achieved the highest quantum capacitance, demonstrating its superior contribution to the enhancement of energy storage properties in the graphene oxide system.

In conclusion, DFT serves as a powerful and versatile theoretical framework that provides profound insights into the electronic structures and properties of materials, particularly metal oxides such as TiO_2. Through first-principles calculations, DFT enables the exploration of novel modifications, such as doping, heterojunction formation, and cocatalyst loading, to enhance the photocatalytic performance. By bridging computational and experimental approaches, DFT not only elucidates the fundamental mechanisms driving catalytic activity but also guides the design of advanced materials for energy conversion and environmental applications, paving the way for transformative advancements in photocatalysis research. Additionally, the integration of machine learning with DFT has opened new dimensions in analysing complex interactions and predictive modelling, further extending its applicability.

8. Reusability and stability of photocatalyst

The stability of a photocatalyst is essential for ensuring its long-term efficiency and practical application in the environmental and energy sectors. A reliable photocatalyst preserves its structural integrity, chemical composition, and photocatalytic activity over multiple cycles, with minimal degradation. This sustained performance is influenced by factors such as resistance to photo-corrosion, durability under harsh conditions, and interactions with the environment. However, deactivation or poisoning of catalysts can occur due to the blockage of their active sites by intermediates, scavengers in complex solutions, or leaching of active materials, which weakens the catalyst structure.[58,433] These compounds often adhere irreversibly to the catalyst surface, hindering its photocatalytic reactions. Factors such as photo-corrosion or the leaching of active components can cause irreversible damage, leading to catalyst decay over time.[434] Many studies have observed a gradual decline in photocatalytic performance and initial reaction rates as the number of reuse cycles increases. This decrease in activity is mainly attributed to the mass loss of the catalyst, the

accumulation of reaction intermediates on its surface, and the presence of inorganic ions or carbonaceous species.[435,436]

The stability of a photocatalyst is its ability to maintain its structure, shape, and chemical properties, ensuring it remains effective over time.[437] This stability is largely influenced by factors such as its synthesis methods, calcination temperature, and surface defects.[438] Reusability refers to the ability of a photocatalyst to be used multiple times. However, the gradual loss of effectiveness with each reuse is a significant challenge in environmental applications. Stability and reusability are closely related, impacting both the cost and efficiency of photocatalytic processes.[436] Key factors such as crystallite nature, surface morphology, and functional groups play a role in the stability of a catalyst, which can be further enhanced through techniques such as heterojunction formation, metal deposition, and doping.[439]

Samriti et al.[440] investigated the reusability and long-term stability of TiO_2 NRs (nanorods) and tantalum-doped TiO_2 NRs as photocatalysts by conducting the photocatalytic degradation of MB under natural sunlight. Impressively, the photocatalysts maintained a high efficiency of 76.48% even after five consecutive cycles, demonstrating exceptional durability with negligible performance loss over the span of a year. The stability of the TiO_2 and Ta-doped TiO_2 NRs was further confirmed through repeated PL measurements, where no significant changes were observed in the PL spectra of the TiO_2 NRs after a year, as shown in Fig. 21(a). These findings highlight the remarkable preservation of their optical properties, showcasing their long-term stability and reusability. To further evaluate the robustness of Ta-TiO_2 NRs, FTIR spectroscopy was performed after five cycles of photocatalytic reactions. The results, as depicted in Fig. 21(b), showed no noticeable shifts in the FTIR peak positions of the 5% Ta-doped TiO_2 nanorods, before and after the reactions. These observations confirm the outstanding stability of the material, even after multiple cycles of use.[440] Similarly, in the recent study by Thakur et al.,[439] the reusability of GO as a standalone photocatalyst for the degradation of organic pollutants under natural sunlight was explored. Although previous researchers utilized chemical desorption methods such as treating MB-loaded GO with desorbing agents such as ethanol, acetic acid, and alkaline solutions to facilitate reuse, these methods often involve additional chemicals and generate waste.[441,442] Instead, Thakur and colleagues[439] adopted a more sustainable approach, using sunlight to remove MB from the surface of GO. This sunlight-mediated photocatalysis leverages the natural energy of sunlight to drive chemical reactions, offering a greener, energy-efficient alternative for MB removal. Initially, MB was adsorbed onto the surface of GO through a standard adsorption process, followed by the separation of MB-loaded GO from the solution via centrifugation and filtration. Subsequently, the resulting powder, with MB attached to the GO surface, was exposed to sunlight for photocatalytic degradation. To confirm the

This journal is © The Royal Society of Chemistry 2025

Catal. Sci. Technol., 2025, **15**, 1702–1770 | **1749**

removal of MB from the GO surface, FTIR spectroscopy was performed, as illustrated in Fig. 21(c), where the disappearance of the characteristic peaks of MB in the FTIR spectra after sunlight exposure confirmed its successful degradation *via* photocatalysis. This method showcases the potential of GO for sustainable, reusable photocatalysis without the need for harmful desorbing agents.

Investigating the long-term stability and reusability of prepared GO/TiO$_2$ photocatalysts is essential for assessing their practical applications. The stability of GO/TiO$_2$ photocatalysts can be evaluated over multiple consecutive cycles using consistent photocatalytic tests. For example, Sharma *et al.*[256] investigated the reusability of GO/TiO$_2$ for the photodegradation of CV dye under visible light, finding only a slight decrease in efficiency after three cycles. Similarly, Adly *et al.*[258] studied the stability of GO/TiO$_2$ in the photodegradation of RhB and AG-25 dyes, reporting a minor reduction in activity from 100% to 91% and 96.2% to 88% after four runs, as shown in Fig. 21(d and e), respectively. Similarly, Kumaran *et al.*[267] reported that even after five cycles, a GO/TiO$_2$ photocatalyst demonstrated high photodegradation efficiency of Orange ME2RL, with only a slight reduction in its performance, decreasing from 99.6% in the first cycle to 98% by the fifth cycle. Zhang *et al.*[276] investigated the reusability of rGO/TiO$_2$ nanocomposites over 10 consecutive cycles, targeting both *E. coli* disinfection and the photodegradation of MO. After 10 cycles, the rGO/TiO$_2$ composites retained approximately

87.4% of their bactericidal efficiency against *E. coli* under visible light and about 88.1% of their photocatalytic efficiency for MO decomposition under UV light. To address the observed decline in performance, they suggested that the calcination method can significantly enhance the stability of rGO/TiO$_2$ composites, thereby improving their long-term effectiveness.

Photocatalyst leaching is a critical factor affecting its stability and reusability, which refers to the release of its active components, such as metal ions, into the reaction medium during photocatalysis. This phenomenon is often triggered by chemical instability, harsh operating conditions, or inadequate bonding of the active species. Leaching not only compromises the efficiency and longevity of the photocatalyst but also raises environmental concerns due to the potential release of harmful substances.[443] There have been limited studies focusing on the leaching behavior of GO/TiO$_2$ nanocomposites. One notable example is the work by Fausey *et al.*,[444] who investigated GO/TiO$_2$ nanocomposite-based fibers (GO/TiO$_2$-fibers) and reduced graphene oxide-TiO$_2$ fibers (rGO/TiO$_2$-fibers) for efficient arsenic removal. Their findings demonstrated that rGO/TiO$_2$-fibers exhibited superior arsenic removal efficiency due to the enhanced conductivity of rGO compared to GO. The improved conductivity facilitated better electron transfer away from the VB of TiO$_2$, suppressing electron–hole recombination and boosting its photocatalytic performance. To evaluate the reusability of these fibers and the associated TiO$_2$ leaching,
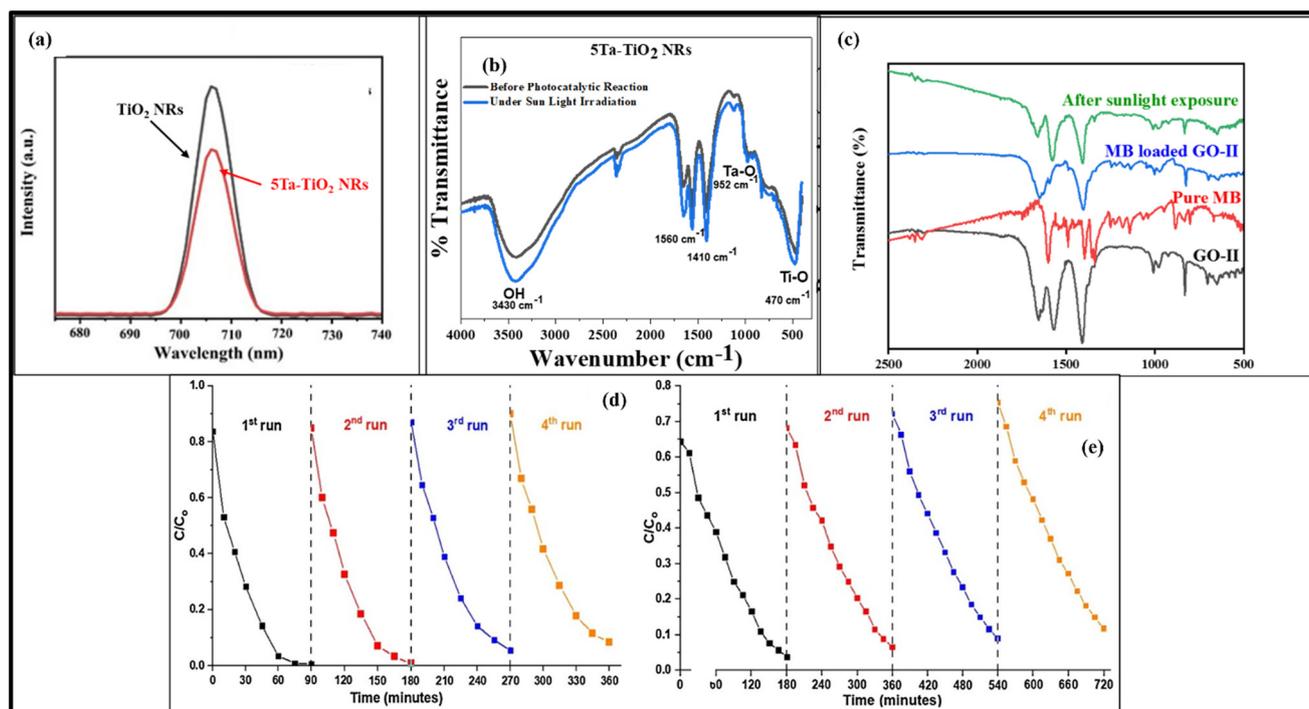

Fig. 21 (a) PL spectra of TiO$_2$ NRs and Ta-TiO$_2$ NRs after one year. (b) FTIR spectra of Ta-TiO$_2$ NRs before and after photocatalytic experiments. Reproduced with permission from ref. 440 Copyright (2023), Springer Nature. (c) FTIR spectra of GO, pure MB, MB loaded GO and GO after exposure to sunlight. Reprinted (adapted) with permission from ref. 439 Copyright (2024), the American Chemical Society. Reusability of GO/TiO$_2$ against (d) RhB and (e) AG-25. Reproduced with permission from ref. 258 Copyright (2018), Elsevier.

the mass of arsenic (As(III)) oxidized per gram of TiO_2 was measured over six cycles. Additionally, the amount of titanium leached by each nanocomposite in each cycle was assessed. Both GO/TiO_2 and rGO/TiO_2 fibers demonstrated reusability, with the rGO/TiO_2-fibers consistently achieving higher As(III) oxidation per mass of TiO_2 throughout the cycles. However, the rGO/TiO_2-fibers showed a larger relative decline in performance over time. Over six cycles, the As(III) oxidation levels by the GO/TiO_2-fibers decreased from 47 mg g^{-1} TiO_2 to 40 mg g^{-1} TiO_2, a 15% performance drop. In comparison, the rGO/TiO_2-fibers dropped from 129 mg g^{-1} TiO_2 to 97 mg g^{-1} TiO_2, reflecting a 23% decline. This greater decrease in performance for the rGO/TiO_2-fibers can be attributed to their higher adsorption of As(v) per mass of TiO_2 compared to the GO/TiO_2-fibers. Despite the performance drop, rGO/TiO_2-fibers maintained significantly higher oxidation levels than GO/TiO_2-fibers, highlighting their potential as efficient and reusable photocatalysts. In the study by Corredor *et al.*,[445] a 2% rGO/TiO_2 composite photocatalyst supported on Nafion membranes was investigated for hydrogen production. The composite was immobilized on Nafion membranes using three straightforward methods that preserved the photocatalyst structure including solvent-casting (SC), spraying (SP), and dip-coating (DP). The SC method embedded the photocatalyst within the membrane matrix, ensuring its stability, while the SP and DP methods positioned the photocatalyst on the membrane surface, reducing their mass transfer limitations and enhancing their accessibility. The leaching of the photocatalyst from the membranes was evaluated by analyzing the turbidity of the solution before and after the photocatalytic process. A linear relationship between turbidity and the composite concentration in the suspension was established for the range of 0 to 10% photocatalyst (w/w). Using this correlation, the amount of photocatalyst leached from the membrane was quantified. The results revealed that the SC and SP membranes exhibited the lowest levels of photocatalyst leaching, while the DP membranes showed significantly higher leaching, over ten times greater than the other methods. The SC membranes demonstrated exceptionally low leaching percentages because the photocatalyst was embedded within the membrane matrix, providing enhanced stability. In contrast, the high leaching percentage of the DP membranes was attributed to the weak deposition of the photocatalyst on the membrane surface. Although SP membranes also relied on surface deposition, their leaching was minimal and comparable to the SC membranes, likely due to the stronger attachment of the photocatalyst to the surface in the SP method. Based on these findings, the SP membrane emerged as the most effective method for immobilizing the composite on Nafion membranes, balancing high hydrogen production rates with minimal photocatalyst leaching.

In summary, the stability and reusability of photocatalysts are crucial for their practical application in environmental and energy sectors. Although maintaining structural integrity

and photocatalytic activity over multiple cycles is essential, challenges such as catalyst deactivation and material loss over time remain significant hurdles. Studies on GO/TiO_2 photocatalysts show promising results, with only slight reductions in efficiency over several cycles. However, further optimization, such as improved synthesis methods, can enhance their long-term stability, ensuring a more consistent and cost-effective performance in real-world applications.

9. Life cycle assessment

Life cycle assessment (LCA) is a crucial tool for evaluating the environmental impacts associated with photocatalysts across their entire lifecycle, from raw material extraction to production, utilization, and end-of-life management. Photocatalysts, such as TiO_2, GO, and their composites, have shown significant potential in applications such as water treatment, air purification, and energy conversion. However, their environmental footprint must be carefully assessed to ensure sustainability.[446] The production phase of photocatalysts often involves energy-intensive processes and the use of hazardous chemicals, contributing to resource depletion and emissions. During the utilization phase, the efficiency of photocatalytic processes depends on factors such as the operating conditions, energy requirements, and feedstock quality. For example, solar-driven photocatalysis has gained attention for its ability to reduce energy consumption and enhance sustainability. End-of-life management remains a critical consideration, given that the disposal or recycling of photocatalysts can introduce environmental risks, including nanoparticle release and toxicity. Incorporating these aspects into LCA allows a more holistic understanding of the environmental trade-offs and guides the development of eco-friendly materials and processes.[447]

By identifying the most impactful lifecycle stages, LCA helps optimize the design and use of photocatalysts, promoting their commercialization in an environmentally responsible manner. This approach is vital for balancing technological advancements with long-term ecological sustainability.

In 2009, Hassan *et al.*[448] conducted a comprehensive LCA of TiO_2 coating technology. To achieve this, they developed a life cycle inventory (LCI) that quantified the energy usage, raw material inputs, and emissions associated with TiO_2 coatings from cradle to grave. Using this inventory, the environmental impact of TiO_2 coatings for concrete pavements was evaluated through the Building for Environmental and Economic Sustainability (BEES) model, a tool designed for assessing sustainable construction alternatives in the U.S. The LCA followed a hybrid methodology, integrating the International Organization for Standardization (ISO) 14040 standards with Input–Output Analysis (IOA). The results demonstrated that TiO_2 coatings significantly reduced the environmental impacts in key categories such as acidification, eutrophication, air pollution, and smog formation. However, the production phase of TiO_2 coatings was found to increase the global warming potential, fossil fuel depletion, water usage, ozone depletion,

This journal is © The Royal Society of Chemistry 2025

Catal. Sci. Technol., 2025, **15**, 1702–1770 | 1751

and human health risks, primarily due to its fossil energy consumption. Despite these drawbacks, the overall environmental performance of TiO_2 coatings was favorable. The life cycle assessment yielded an overall environmental performance score of −0.70, indicating that the application of TiO_2 coatings on concrete surfaces has a net positive environmental impact. This highlights the potential of TiO_2 coatings as sustainable technology for reducing environmental harm in specific contexts. In another study, Babaizadeh et al.[449] found the same conclusion as above in the case study of a nano-sized TiO_2 coating on residential windows. The TiO_2 coatings on window panes showed a positive impact in reducing acidification potential, eutrophication potential, criteria air pollutants, and smog formation potential. However, they contributed to increased environmental burdens in areas such as global warming, fossil fuel depletion, water usage, human health, and ecological toxicity. However, despite these drawbacks, their overall normalized environmental performance, particularly in air purification, remains positive. Additionally, when considering various weighting factors for environmental and economic scores, TiO_2-coated glass demonstrates a superior overall performance compared to uncoated glass in most scenarios.

In the study by Hischier et al.,[450] most scenarios showed that nano-paints and nano-coatings have lower environmental impacts compared to traditional paints, except when the lifetime of the nanomaterial is considered to be short. However, their ecotoxicity potential has emerged as the most significant environmental concern. Human toxicity potential exhibited much lower variability than ecotoxicity, which is largely attributed to the release patterns of TiO_2, while ecotoxicity considered emissions into water, and human toxicity focused on air emissions, which were 3 to 4 times less significant. In the study on self-cleaning glass by Pini et al.,[451] a mild positive effect was observed in reducing airborne pollutants during the use phase due to the nano-TiO_2 film. However, the negative impacts of nano-TiO_2 were primarily linked to particle release, which affected multiple environmental categories. In the use phase, the release of particles into the air can influence human toxicity, particularly carcinogenic effects, while in the end-of-life phase, inhaled particles can further impact human health. Nonetheless, the positive effects of emission reduction from the self-cleaning glass may outweigh the potential harm from nanoparticle release, provided that eco-design strategies are implemented effectively. In a study by Fernandes et al.,[452] the LCA of TiO_2 photocatalyst synthesis was conducted, revealing that isopropyl alcohol has the highest environmental impact among the reagents used, except in categories such as land use and mineral resource scarcity, where the titanium precursor is the main contributor. The sensitivity analysis demonstrated that changes in isopropyl alcohol usage (±30%) significantly influenced the environmental profiles of TiO_2 photocatalysts. These results underscore the importance of isopropyl alcohol in the synthesis process, suggesting that efforts to reduce or replace it can enhance the sustainability

of TiO_2 production. Furthermore, substituting isopropyl alcohol with ethanol was found to improve the sustainability, prompting recommendations for further studies to assess its impact on the photocatalytic performance of the nanomaterial.

The transition from a fossil fuel-based economy to a sustainable, green economy is one of the most pressing challenges of our time. In this context, the biological synthesis of NPs using plant extracts is being investigated as an environmentally friendly alternative to traditional methods, with the aim of minimizing environmental impacts. A recent study by Rodríguez-Rojas et al.[453] compared the environmental impacts of two TiO_2 nanoparticle synthesis methods, green chemistry (using an aqueous extract of Cymbopogon citratus) and the chloride route, two widely used techniques. The LCA, conducted using OpenLCA software, showed that chemically synthesized TiO_2 contributes to greenhouse gas emissions and respiratory issues linked to inorganic substances. In contrast, the green synthesis method was found to offer advantages, including reduced toxicity and lower greenhouse gas emissions, positioning it as a more sustainable alternative.

The methods for the production of GO differ in terms of precursor requirements, chemical processes, energy consumption, environmental impact, scalability, material properties, and production yield. Thus, selecting the most suitable method for industrial applications requires a comprehensive evaluation of these factors, alongside the desired performance characteristics for the intended application.

The well-established LCA method provides a systematic approach for these evaluations. LCA involves multiple stages to generate valuable insights into the environmental impacts across various categories. These categories include human toxicity, water contamination, resource depletion, and climate-related issues such as greenhouse gas emissions and ocean acidification. By offering a detailed comparison, LCA supports informed decision-making for the sustainable production and application of GO. Serrano-Lujan et al.[454] conducted an LCA on the production of GO and reduced rGO using the Hummers (hydrazine-reduced (hGO), and glucose-reduced rGO) and Marcano methods. These two methods are widely regarded as the most successful techniques for synthesizing high-performance GO and rGO. However, both approaches have faced criticism for generating significant toxic emissions, raising concerns about their environmental and health impacts. The modified Hummers' method (Marcano method) demonstrated better environmental performance due to its higher conductivity and reduced material needs for applications such as transparent electrodes. Among the evaluated methods, the glucose-based route (gGO) had the lowest overall environmental impact, while the Hummers' method (hGO) was criticized for generating toxic NOx emissions and hydrazine-related health risks. Despite this, the Hummers' method had slightly lower environmental impacts in some categories compared to

1752 | Catal. Sci. Technol., 2025, 15, 1702–1770

This journal is © The Royal Society of Chemistry 2025

Marcano's method, though the higher performance of the latter in electronic applications justifies its use.

Finally, Pesqueira et al.[455] conducted a comparative LCA of solar heterogeneous photocatalysis for treating secondary urban wastewater, using GO/TiO_2 and commercially available TiO_2–P25 as photocatalysts. Their study evaluated the environmental impact of the GO/TiO_2 treatment process across various impact categories and compared it with the solar/TiO_2 process. The results indicated that the GO/TiO_2 process has higher potential environmental impacts than the TiO_2 process under the current conditions. This is primarily due to the significant environmental burdens associated with the synthesis of GO/TiO_2, particularly the use of ammonium hexafluorotitanate. The production of this compound involves the use of HF during the synthesis of NH_4F, which substantially contributes to its environmental footprint, together with the use of boric acid.

In contrast, TiO_2–P25, already produced and utilized on an industrial scale (though not specifically for full-scale wastewater treatment), benefits from optimized manufacturing processes. The production of TiO_2–P25 is guided by the European Commission's reference document on best available techniques, making it a more environmentally efficient option. Alternatively, GO/TiO_2 has not yet reached industrial-scale production, and its current synthesis method, particularly via liquid phase deposition, is not recommended compared to TiO_2 alone due to its high associated environmental impacts. Interestingly, this study found that the environmental impacts of GO synthesis itself are negligible in comparison. A significant reduction in the environmental burden of the GO/TiO_2 composite could be achieved if TiO_2 is incorporated via mechanical mixing rather than liquid phase deposition. However, this approach may lead to lower photocatalytic activity, requiring further research to optimize its performance, while minimizing environmental impacts.

In conclusion, LCA of photocatalysts highlights the critical need to balance technological advancements with environmental sustainability. Although TiO_2-based materials, including composites with GO, offer immense potential for applications in water treatment, air purification, and energy conversion, their environmental impacts vary significantly depending on their synthesis methods, materials used, and operational parameters. Studies emphasize the importance of optimizing production processes, minimizing hazardous chemical use, and exploring alternative synthesis routes to reduce the environmental burdens. Moreover, the end-of-life management of photocatalysts must be carefully addressed to mitigate the risks associated with nanoparticle release and toxicity.

By integrating LCA insights, researchers and industries can make informed decisions to enhance the eco-efficiency of photocatalyst production and utilization. Future efforts should prioritize sustainable practices, such as green synthesis methods and renewable energy integration, to ensure that the benefits of these advanced materials are achieved without compromising environmental health.

10. Toxicity of nanomaterials

Nanotechnology, as defined by The US National Nanotechnology Initiative (NNI), involves the manipulation and control of materials and structures at the nanoscale, typically between 1 and 100 nm, unlocking unique phenomena that pave the way for groundbreaking applications.[456] Recent scientific advancements highlight the immense potential of nanotechnology, particularly due to the enhanced biological efficiency of nanomaterials a result of their high surface-to-volume ratio, which is rarely seen in bulk materials. However, amid the excitement, the issue of nanotoxicity remains critically underexplored. The burgeoning field of 'nanotoxicology', a branch of nanomedicine, focuses on understanding the toxicological impacts of engineered nanomaterials on humans, animals, and the environment. These materials can induce toxicity through mechanisms such as the generation of ROS, depletion of glutathione, lipid peroxidation, oxidative DNA stress, mutagenesis, promotion of apoptotic signals, and chromosomal aberrations.[457–459]

As the use of nanomaterials expands across industries including cosmetics, medicine, food, and agriculture, their potential benefits are vast, but also the likelihood of increased human exposure in workplaces and daily life.[460] Interestingly, in certain contexts, the toxicity of nanomaterials is advantageous, particularly in their antimicrobial action. This is achieved through mechanisms such as membrane destabilization, cytoplasm leakage, organelle damage, and the generation of ROS, which can lead to protein or nucleic acid damage and the modulation of signal transduction pathways. Therefore, it is crucial to investigate nanotoxicity from multiple angles, given that the toxic effects of engineered nanomaterials are closely tied to their physicochemical properties.[457]

Nanomaterials are widely researched for their potential in water purification and treatment, particularly due to their photocatalytic properties.[45,439] However, the use of these materials in these applications also raises concerns about their potential presence in the treated water. When employed as photocatalysts in wastewater treatment, there is a risk that residual NPs may remain in the water after treatment, posing potential health and environmental risks. The unintended presence of leftover nano-photocatalysts and nano-adsorbents in the environment during the wastewater treatment process has highlighted their toxic effects on various living organisms.[461] If these NPs are lipophilic, they can persist in the food chain and enter the digestive system through food or water. Numerous studies in the literature have explored the uptake of NPs in the intestines, with many indicating that nanosized particles can pass through the intestinal tract and be quickly eliminated from the body.[462] However, a significant study by Bettini et al.[463] focused on the uptake effects of food-grade TiO_2 NPs, which are used as a white pigment in Europe (E171). This research was particularly important because the daily oral intake of these

This journal is © The Royal Society of Chemistry 2025

Catal. Sci. Technol., 2025, **15**, 1702–1770 | **1753**

TiO$_2$ NPs has been linked to an increased risk of carcinogenesis and chronic intestinal inflammation. The findings underscore the need for further investigation into the long-term effects of nanoparticle exposure, especially when these materials are used in consumer products and potentially ingested regularly. Furthermore, the interactions between NPs and biological systems, including proteins, enzymes, and DNA, can greatly influence their toxicity. The components and physicochemical properties of these nanomaterials can disrupt the development of organisms, interfering with normal physiological processes and potentially causing severe abnormalities that may be fatal for embryos and growing animals. As a result, the removal of these NP photocatalysts from treated water has become a critical issue due to their hazardous effects on both humans and aquatic life.[456]

As we transition to exploring the toxicity of GO/TiO$_2$ nanocomposites, it is crucial to understand how the individual toxicity GO and TiO$_2$ may further influence the safety profile of GO/TiO$_2$. The following section will delve into the toxicological impacts of TiO$_2$, GO and GO/TiO$_2$ nanocomposites, examining their interactions with biological systems and potential environmental consequences.

10.1. Toxic effect of TiO$_2$

As previously mentioned, TiO$_2$ stands out as the most widely used semiconductor photocatalyst for water treatment due to its remarkable and beneficial properties. Beyond water treatment, TiO$_2$ has been extensively use in various commercial and industrial applications, including the paint industry, paper production, cosmetics, textiles, and surface coatings, owing to its anti-corrosive nature and exceptional stability. On a larger scale, TiO$_2$ NPs are also employed in products such as toothpaste, food colorants, and nutritional supplements.[43] However, this widespread use of nano-TiO$_2$ raises concerns given that it can potentially become a significant environmental pollutant.

TiO$_2$ enters the environment either directly through production losses and product use or indirectly *via* sewage sludge and wastewater treatment plant effluent. Aquatic ecosystems, including rivers, lakes, estuaries, and coastal areas, are particularly vulnerable, receiving a substantial portion (approximately 20–35%) of this environmental load.[464] Recent estimates indicate that the nano-TiO$_2$ concentrations in coastal waters can reach up to 16.8 µg L^{-1} in European waters and as high as 103 µg L^{-1} in San Francisco Bay, with even greater concentrations found in sediments.[465] During summer, levels may soar to over 900 µg L^{-1} in surface waters near popular beaches.[466]

Although TiO$_2$ is generally regarded as having minimal toxicity, growing concerns have emerged regarding its potential carcinogenic effects in humans, as highlighted by the International Agency for Research on Cancer (IARC).[467] Numerous studies have highlighted the hazardous effects of TiO$_2$ NPs, particularly their ability to cross the blood–brain

barrier or enter the brain through the nasal-to-brain axonal route, leading to neurotoxicity.[468] Once these NPs reach the central nervous system, they can initiate a chain of events that may result in neurodegenerative diseases and psychiatric disorders. These events include inflammation, immune responses, swelling, cell necrosis, and cellular damage.[469] The negative biological effects of TiO$_2$ NPs are largely attributed to oxidative stress, which has been shown to chronically increase the production of ROS and other oxidative byproducts.[470–472] Among the various harmful effects of TiO$_2$ NPs, oxidative stress stands out as the primary mechanism driving their biological toxicity. This stress is induced by TiO$_2$ NPs both in the presence and absence of UV radiation. Tang *et al.*[473] systematically investigated the effects of TiO$_2$ NPs on adult zebrafish and their embryos, revealing that prolonged exposure made the gill and liver tissues particularly susceptible to oxidative damage. Alternatively, Gnatyshyna *et al.*[474] studied the impact of TiO$_2$ on the freshwater bivalve *Unio tumidus* and found that TiO$_2$ exhibited an antioxidant effect, reducing ROS production and phenoloxidase (PhO) activity, while doubling the concentration of reduced glutathione (GSH) in the digestive gland. In human studies, Gurr *et al.*[475] reported that a combination of anatase and rutile TiO$_2$ NPs induced oxidative damage in human bronchial epithelial (BEAS-2B) cells. Petković *et al.*[476] further compared the genotoxic and cytotoxic effects of pre-irradiated and non-irradiated anatase TiO$_2$ particles. Their findings revealed that while non-irradiated TiO$_2$ NPs only had a minor impact on DNA strand breakage and no significant effect on cell survival, pre-irradiation led to significant DNA damage and reduced cell viability, highlighting the potential risks associated with these NPs.

The neurotoxicity of nano-TiO$_2$ in bivalves has not been extensively explored, but recent research on the blood clam *Tegillarca granosa* suggests a potential toxic mechanism at play. In the study by Guan *et al.*,[477] they found that exposure to waterborne nano-TiO$_2$ at concentrations of 0.1, 1, and 10 mg L^{-1} led to increased levels of neurotransmitters, including dopamine, acetylcholine, and γ-aminobutyric acid. Additionally, it decreased the activity of acetylcholine esterase and suppressed the expression of genes involved in neurotransmitter modulation and receptor activity. Jovanović *et al.*[478] studied the immunotoxicity of TiO$_2$ and found that nano-TiO$_2$ anatase, at doses of 2 ng g^{-1} and 10 mg g^{-1} body weight, caused significant immunotoxic effects in the fathead minnow (*Pimephales promelas*), particularly by reducing the bactericidal function of neutrophils. In another study, Jovanović *et al.*[479] revealed that exposure to nano-TiO$_2$ anatase at a concentration of 0.1 mg L^{-1} in *Pimephales promelas* led to a negative shift in immune gene expression and neutrophil function, suggesting the potential disruption of the innate immune responses of the fish. Exposure to nano-TiO$_2$ has also been shown to adversely affect the metabolism and energy balance of bivalves. High levels of waterborne nano-TiO$_2$ (2.5 and 10 mg L^{-1}) significantly

1754 | *Catal. Sci. Technol.*, 2025, **15**, 1702–1770

This journal is © The Royal Society of Chemistry 2025

suppressed the filtration activity, food absorption efficiency, and aerobic scope for growth in the mussel *Mytilus coruscus*.[480] Similarly, exposure to nano-TiO$_2$ at concentrations of 50 and 100 μg L^{-1} reduced the filtration activity of the Mediterranean clam *Ruditapes decussatus*.[471]

According to a bibliometric analysis by Luo *et al.*[481] on the toxic effects of TiO$_2$, the investigation into the organismal-level effects of nano-TiO$_2$ emerged as a key area of scientific exploration during 2011–2013, as shown in Fig. 22(a). Their analysis revealed that studies on the molecular and cellular effects of nano-TiO$_2$ continued to dominate this field, reflecting growing awareness of the potential off-target effects of nano-TiO$_2$ in aquatic environments and an increased focus on its ecotoxicological impacts, alongside ongoing research

Fig. 22 Bibliometric map of the studies on (a) toxic effects of nano-TiO$_2$ and (b) molecular biology studies on the effects of nano-TiO$_2$. Reproduced with permission from ref. 481 Copyright (2020), John Wiley and Sons.

This journal is © The Royal Society of Chemistry 2025

Catal. Sci. Technol., 2025, **15**, 1702–1770 | **1755**

in biomedical models. In another aspect of their analysis, Luo et al.[481] identified that within the molecular biology subfield of nano-TiO$_2$ research, the impacts of "nano-anatase" on the "photosystem" became a prominent topic since 2010, as shown in Fig. 22(b). By 2012, research had shifted towards understanding the mechanisms by which nano-TiO$_2$ affects cells. Since 2013, "inflammation", "oxidative stress", and "genotoxicity" have emerged as significant research topics in nano-TiO$_2$-related molecular biology studies.

In conclusion, although TiO$_2$ has long been valued for its diverse applications in water treatment and various industries due to its stability and anti-corrosive properties, its widespread use, particularly in nanoparticle form, raises significant environmental and health concerns. The infiltration of nano-TiO$_2$ into aquatic ecosystems poses potential risks, as highlighted by increasing concentrations in coastal waters and sediments. The growing body of research underscores the harmful biological effects of nano-TiO$_2$, including oxidative stress, neurotoxicity, and immunotoxicity, which can lead to severe ecological and health impacts. The focus of scientific exploration has increasingly shifted towards understanding these mechanisms at the molecular, cellular, and organismal levels, reflecting the urgent need to address the ecotoxicological implications of nano-TiO$_2$ in our environment.

10.2. Toxicity of GO

GO-based materials are widely used in various applications, leading to an increase in the release of non-biodegradable GO into the environment.[482] Although GO is generally considered less toxic compared to many other nanomaterials, it is important to note that its potential toxicity can vary depending on factors such as the type of carbon material, its size, surface functionalization, and exposure conditions. However, these nanocatalysts can cause secondary pollution in the environment, increasing the risk of toxicity to aquatic animals and humans, primarily through the generation of ROS and oxidative stress. Due to their negatively charged surface, carbon-based nano-photocatalysts have a strong tendency to interact with cellular membranes, organelles, nucleic acids (DNA and RNA), and proteins, which can lead to potential toxicity.[483–485] The toxicity of graphene oxide (GO) in cells is influenced by several factors, including its dose, lateral size, and surface charge.[486,487] The effect of GO on different organs is shown in Fig. 23(a). Research on the cytotoxicity of GO has yielded mixed results; while, some studies report no adverse effects on cellular behavior, others indicate potential for cellular damage. On the positive side, GO has been shown to significantly enhance cell growth by improving mammalian cell attachment and proliferation.[488,489] It has also been found to boost cell adhesion and proliferation with excellent biocompatibility. These beneficial interactions are largely attributed to the chemical structure of GO, which features abundant oxygen-containing functional groups that support cell adhesion and

growth.[489] Furthermore, GO has been identified as an effective provider of essential signals and soluble factors that promote cell adhesion and growth.[490]

Conversely, several studies highlight the potential toxic effects of GO. For example, Wang et al.[492] reported severe chronic toxicity in Kunming mice when exposed to GO concentrations of around 15 mg kg^{-1}. In the study by Bangeppagari et al.,[493] it was found that low concentrations of GO had no impact on zebrafish embryonic development. However, at higher concentrations, GO led to significant embryonic mortality. Higher doses resulted in increased heartbeat, apoptosis, delayed hatching, cardiotoxicity, cardiovascular defects, and reduced hemoglobin production. Additionally, research by Souza et al.[494] demonstrated that GO induces both acute and chronic toxicity in the freshwater cladoceran Ceriodaphnia dubia. Chronic exposure to GO reduced the number of neonates and feeding rates, while increasing ROS generation. The accumulation of GO on the Ceriodaphnia dubia body after exposure was mainly found in its digestive tract. The mechanism of GO toxicity is shown in Fig. 23(b).

Chang et al.[495] found that smaller GO nanosheets caused more severe oxidative stress and greater cytotoxicity in A549 cells compared to larger GO sheets. Additionally, the uptake of GO by cells is size-dependent.[496] A recent study investigated the effects of GO size on Leydig (TM3) and Sertoli (TM4) cells using two nanosheet sizes (100 nm and 20 nm) prepared via a modified Hummer's method. The 20 nm GO nanosheets led to greater cell viability loss, decreased cell proliferation, extensive leakage of lactate dehydrogenase (LDH), and increased ROS generation compared to the 100 nm GO. Both sizes of GO reduced the mitochondrial membrane potential (MMP) in TM3 and TM4 cells and induced oxidative DNA damage, as evidenced by elevated levels of 8-oxo-dG, a marker of ROS-induced DNA damage. Moreover, both GO sizes upregulated genes associated with DNA damage and apoptosis. This study revealed that the 20 nm GO was more toxic than the 100 nm GO, with reduced MMP and increased apoptosis being the primary indicators of toxicity. The size-dependent toxicity of GO was particularly evident in male germ cells, especially in TM3 cells.[497]

Another critical factor affecting cytotoxicity is the surface charge of GO. Research indicates that the surface charge of GO influences its cell internalization and absorption.[498] The interaction between GO and cell membranes can lead to morphological changes and cell lysis, including hemolysis of red blood cells. This is attributed to the strong electrostatic interactions between the negatively charged oxygen groups on the surface of GO and the positively charged phosphatidylcholine on the outer membrane of red blood cells. Pelin et al.[499] investigated the cytotoxicity of GO samples with varying oxidation levels using HaCaT keratinocytes, an in vitro model for skin toxicity. Their study revealed that after a 72 h exposure to few-layer graphene (FLG), the less-oxidized GO exhibited lower cytotoxic effects, causing less damage to mitochondrial and plasma
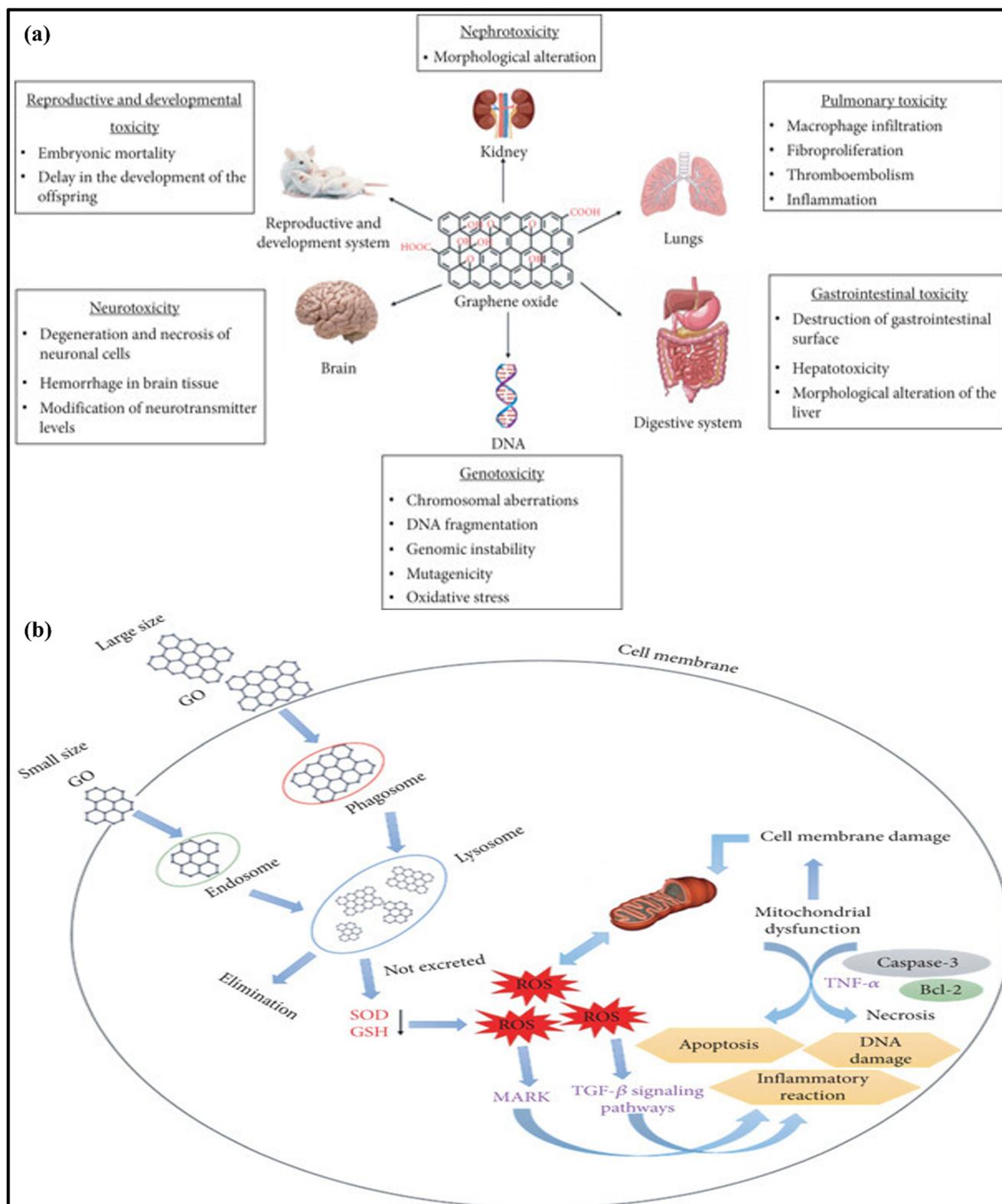
1756 | Catal. Sci. Technol., 2025, 15, 1702–1770

This journal is © The Royal Society of Chemistry 2025

Fig. 23   (a) Effect of GO on organs. (b) Mechanism of GO toxicity.[491]

membranes. In contrast, GO with the highest oxidation level demonstrated the greatest cytotoxicity, leading to more significant harm to these cellular structures. The findings suggest that higher concentrations and prolonged exposure to GO can impair mitochondrial function and damage the plasma membrane, highlighting its potential cytotoxic impact

This journal is © The Royal Society of Chemistry 2025

Catal. Sci. Technol., 2025, 15, 1702–1770 | 1757

on the skin. Yang et al.[500] demonstrated that both monolayer and multilayer GO nanosheets promoted ROS generation in dendritic cells. However, monolayer GO had a lesser impact on cell viability compared to multilayer GO. Despite this, both types of GO induced immunotoxicity and caused cell disruption. Gene expression profiling revealed that both forms of GO led to significant changes in the transcriptome, with monolayer GO resulting in more extensive alterations in gene expression compared to multilayer GO.

In summary, graphene oxide (GO) exhibits a complex toxicity profile influenced by factors such as oxidation level, size, surface charge, and exposure conditions. Although GO demonstrates potential benefits, such as enhanced cell growth and improved biocompatibility, it also poses significant risks, including oxidative stress, cellular damage, and environmental toxicity. The variable effects observed across different studies underscore the importance of carefully assessing the toxicity of GO in various contexts.

10.3. Toxicity of GO/TiO$_2$

Given the detailed discussion of the multifunctional applications of GO/TiO$_2$ in the preceding sections, it is essential to address its associated toxicity concerns to ensure safe applicability. Both TiO$_2$ and GO have exhibited toxicity at the individual level, and numerous studies have explored the potential toxicity of their combined nanocomposite, GO/TiO$_2$. Recently, Guo et al.[501] investigated the toxicity of GO/TiO$_2$ on the giant river prawn, Macrobrachium rosenbergii, across different concentrations. They examined the effects of GO/TiO$_2$ composite exposure on the activities of digestive and antioxidant-related enzymes, as well as the expression of growth and immune-related genes at the transcriptomic level. The results indicated that the survival rate and growth performance of the prawns were not adversely affected by the GO/TiO$_2$ composite at either exposure level. However, the exposure did impact the activities of digestive and antioxidant enzymes in the juvenile prawns. Additionally, the expression levels of genes related to growth and immunity were significantly altered by the GO/TiO$_2$ composite. Specifically, after exposure to 0.1 mg L^{-1} of the composite, the mRNA expression level of MSTN was significantly increased, while the levels of EcR, raptor, and CaBP significantly decreased. These findings suggest that the presence of GO/TiO$_2$ composites in the aquatic environment can disrupt the physiology of M. rosenbergii by altering enzyme activity and gene expression.[501]

Similarly, Prakash et al.[502] explored the toxicity of rGO/TiO$_2$ nanocomposites synthesized with varying TiO$_2$ concentrations using a zebrafish embryo model. Key metrics such as zebrafish body length, heartbeat count, and survival percentage were meticulously measured in controlled experiments. The results revealed that the rGO/TiO$_2$ nanocomposite exhibited very low toxicity to zebrafish embryos at a lower concentration of 30 μg mL^{-1}. However, its toxicity increased with higher concentrations reaching up to 1.0 mg mL^{-1}. The heartbeat of zebrafish embryos was monitored every 30 s for 48 h post-fertilization (hpf) and for larvae at 96 hpf. A noticeable decrease in heartbeat was observed at higher concentrations (0.125–1 mg mL^{-1}) across all the rGO/TiO$_2$ nanocomposites. Additionally, the hatching percentage of embryos and larvae, measured at 72 hpf, significantly declined at concentrations between 0.125 and 1 mg mL^{-1}. This reduction was attributed to the presence of Ti ions in the rGO/TiO$_2$ nanocomposite, which interfered with enzymatic activity crucial for the hatching process. The survival percentage of zebrafish embryos and larvae also decreased with an increase in concentration, given that higher levels of the rGO/TiO$_2$ nanocomposite generated ROS, leading to teratogenicity and cardiotoxicity. Overall, this study demonstrated that the toxicity of rGO/TiO$_2$ is concentration dependent.[502] Similarly, Al-Kandari et al.[503] examined the environmental impacts of two types of rGO/TiO$_2$ semiconductor photocatalysts, thermally reduced (T-GO/TiO$_2$) and hydrogen-reduced (H-GO/TiO$_2$). Their study focused on assessing their acute toxicity, cardiotoxicity, neurobehavioral toxicity, hematopoietic toxicity, and effect on the hatching rates in zebrafish embryos. The results revealed that T-GO/TiO$_2$ was significantly more toxic than H-GO/TiO$_2$, inducing severe toxicity across all parameters tested. Notably, the embryos treated with T-GO/TiO$_2$ exhibited a drastic reduction in hatching rates at concentrations of 600 mg L^{-1} and above, while those treated with H-GO/TiO$_2$ experienced a more gradual and less severe delay in hatching. A dose-dependent increase in spontaneous tail coiling was observed in the T-GO/TiO$_2$-treated embryos at 24 h post-fertilization (hpf). According to the Fish and Wildlife Service Acute Toxicity Rating Scale, T-GO/TiO$_2$ is classified as "practically not toxic", while H-GO/TiO$_2$ is considered "relatively harmless".

However, both nanocomposites should be used with caution at concentrations higher than the No Observed Effect Concentration (NOEC) of 400 mg L^{-1}. Particularly, T-GO/TiO$_2$ significantly caused pericardial and yolk sac edema, decreased hatching rates, impaired locomotion, and reduced hematopoietic activity, along with affecting the heart rate. These teratogenic effects were notably less severe in the H-GO/TiO-treated embryos, suggesting that H-GO/TiO photocatalysts may be more environmentally friendly than their thermally reduced counterparts. Jin et al.[329] investigated the distribution and cytotoxicity of GO/TiO$_2$ nanocomposites in A549 cells. Their results showed that GO could penetrate A549 cells, localizing in both the cytoplasm and nucleus without causing any observable cell damage. However, after the GO/TiO$_2$ composite entered the cells, the TiO$_2$ NPs and GO were found to separate. This study also revealed that the GO/TiO$_2$ composite induced cytotoxicity comparable to that of TiO$_2$ NPs, likely due to oxidative stress.

The rising use of photocatalysts in water treatment has brought their toxicity to the forefront, demanding urgent scrutiny. Although these materials are hailed for their ability to degrade organic pollutants, remove heavy metals, eliminate pathogens, and combat microplastic contamination, their potential risks to human health and the

1758 | Catal. Sci. Technol., 2025, 15, 1702–1770

This journal is © The Royal Society of Chemistry 2025

environment must not be underestimated. Nano-photocatalysts, in particular, can trigger oxidative stress, cellular dysfunction, and other toxic effects, which vary depending on their composition and interaction with biological systems. Understanding these toxicological impacts is essential for the safe deployment of photocatalysts in environmental remediation. Although TiO_2 and GO each have well-known toxicological profiles, their combination in GO/TiO_2 nanocomposites presents new and potentially heightened risks, especially in aquatic environments and at higher concentrations. This underscores the need for thorough assessment and regulation to ensure that the benefits of these materials are not overshadowed by their hazards. Delving into the complex mechanisms of toxicity and identifying the conditions that heighten these risks will be vital for the safe and sustainable use of photocatalysts in both environmental and biomedical applications.

11. Challenges and prospects

Currently, a diverse array of nanocomposites derived from GO and its derivatives with metal oxides are under development for applications in the field of photocatalysis. Research in this area remains active and expansive, aimed at overcoming technological and economic hurdles for practical viability. There are notable concerns surrounding existing systems that require resolution.

• Active research and critical factors affecting photocatalytic efficacy

The photocatalytic efficacy of graphene-based TiO_2 composites in the photodegradation of organic dyes predominantly hinges on several factors. These include the presence of potent oxidizing agents and adsorbed pollutants, which affect the electron–hole recombination rates, electron mean free paths, and the specific surface area of the photocatalyst, respectively. Thus, researchers are actively investigating methods to improve these factors, thereby enhancing the degradability of photocatalysts.

• Challenges in enhancing chemisorption and unclear mechanism in enhanced photocatalysis

Achieving enhanced chemisorption capabilities in graphene-based TiO_2 nanocomposites necessitates careful consideration of the chemical interactions between graphene and pollutants. Furthermore, the design and fabrication of high-performance photocatalytic composites based on graphene-based titania nanocomposites must address additional challenges. Despite the significant progress in developing GO/TiO_2 hybrids, the underlying mechanism for their enhanced photocatalytic behavior remains partially unclear. Thus, further studies, integrating both theoretical and experimental approaches, are needed to fully understand the exceptional electronic and semiconducting properties of graphene-assisted photocatalytic mechanisms in these hybrids.

• Limited industrial-scale application

Only a few pilot plant trials using GO/TiO_2 photocatalysts, primarily for wastewater purification and post-treatment, have been reported. Recently, in 2020, Luna-Sanguino et al.[297] demonstrated that even at very low concentrations of rGO/TiO_2, complete removal of pesticides was achieved in less than 25 min. This study highlighted the efficiency of nanocomposites in pilot-plant scale solar processes for mitigating refractory and bio-recalcitrant contaminants in effluents, showcasing a sustainable and efficient approach. Despite the advanced developments and findings in photocatalysts, the industrial-scale application of GO/TiO_2 remains limited. One significant issue is the potential agglomeration of GO–TiO_2, which reduces the overall surface area and consequently lowers the rate of photodegradation, making it less effective for industrial use. Thus, to address these drawbacks, more research is needed to minimize their agglomeration and enhance their photocatalytic performance in pollutant removal, while also reducing costs.

• Environmental and regeneration concerns

Additionally, although GO-based nanocomposites offer numerous benefits, they present challenges in terms of regeneration after use and can potentially release secondary pollutants into the environment. Therefore, future research should focus on developing green synthesis approaches or magnetic ternary GO-based nanocomposites to mitigate environmental pollution and reduce costs. Addressing the instability of GO-based nanocomposites is crucial to prevent potential environmental threats.

• Formation and evaluation of toxic by-products

During the photocatalytic treatment of wastewater, there is a risk of forming even more toxic by-products when the degradation of organic pollutants is incomplete, leading to the generation of intermediate compounds that can be more harmful than the original contaminants. These intermediates, including aldehydes, ketones, and carboxylic acids, may exhibit higher toxicity levels. Studies have shown that conventional chemical analysis often fails to fully assess the toxicity of these by-products or their potential synergistic effects. The formation of these by-products is influenced by factors such as the type of photocatalyst, operational conditions, and the nature of the pollutants.

To assess toxicity, various bioassays have been applied, including tests with bacteria, invertebrates, microalgae, plants, and mammalian cells. Although photocatalytic treatment typically reduces wastewater toxicity, some studies have reported a significant increase in toxicity during the treatment of municipal and industrial wastewater. This increase may result from factors such as the dissolution of the photocatalyst, the generation of more toxic by-products, and synergistic effects from multiple contaminants. Additionally, the use of chemical agents such as hydrogen peroxide (H_2O_2) in combined photocatalytic processes can contribute to toxicity if residual

This journal is © The Royal Society of Chemistry 2025

Catal. Sci. Technol., 2025, 15, 1702–1770 | 1759

concentrations remain post-treatment. Granular activated carbon (GAC) filtration is commonly used to remove residual H_2O_2, ensuring the safe discharge or reuse of treated wastewater. It is crucial to evaluate the toxicity of wastewater before and after GAC filtration, especially without prior H_2O_2 removal. Addressing the formation of toxic by-products requires a deep understanding of photocatalytic degradation pathways and strategies to ensure complete pollutant mineralization. Therefore, ongoing toxicity assessments throughout the photocatalytic treatment process are essential to enhance the efficacy and safety of photocatalytic wastewater treatment.

12. Summary and conclusion

TiO_2, known for its high stability, commercial availability, and cost-effectiveness, is particularly suitable for environmental remediation in water treatment and air pollution control together with sustainable energy production. However, TiO_2 exhibits drawbacks including low chemical adsorption, high electron–hole recombination rates, and poor activity under visible light. These limitations can be mitigated by incorporating nanomaterials such as GO into TiO_2 matrices. The integration of graphene effectively reduces the electron–hole recombination rate and enhances chemisorption due to its superior electron storage capacity, high electron mobility, large specific surface area, and zero bandgap. Consequently, this enhancement improves the adsorption and photodegradation rates of various contaminants when exposed to visible radiation.

GO-based composites show significant promise as highly efficient photocatalysts for environmental and energy applications. Among them, GO/TiO_2 nanocomposites stand out as a compelling frontier in advanced materials. In recent years, GO/TiO_2 nanocomposites have been intensively studied for their applications across various fields. Continuous advancements in the synthesis, fabrication, and modification of GO/TiO_2 have introduced novel properties and applications. This review highlighted the photocatalytic characteristics of TiO_2 and GO, both as standalone materials and as cocatalysts, and provided several examples focusing on the recent progress in the design, synthesis, and applications of GO/TiO_2 nanocomposites as photocatalysts. In the field of organic pollutant degradation, GO/TiO_2 nanocomposites have demonstrated superior photocatalytic activity, which is attributed to the synergistic effects between GO excellent electron transfer properties and strong oxidation capability of TiO_2 under UV light. This makes GO/TiO_2 effective for degrading a wide range of organic pollutants in water and air, thereby offering a sustainable solution to environmental contamination. Moreover, in CO_2 conversion and hydrogen production, these nanocomposites exhibit significant potential. Although TiO_2 traditionally absorbs UV light, limiting its efficiency to only a fraction of the solar spectrum, the incorporation of GO extends its photoresponse into the visible range. This expands the photocatalytic efficiency of nanocomposites, enabling the reduction of CO_2 to valuable hydrocarbons and facilitating hydrogen evolution from water under sunlight.

The stability and reusability of photocatalysts, including GO/TiO_2 nanocomposites, are crucial for their effective and sustainable application in the environmental and energy sectors. Although studies show that GO/TiO_2 maintains substantial photocatalytic activity over multiple cycles with only minor efficiency reductions, challenges such as catalyst deactivation and material loss still persist. Advances in synthesis methods and stabilization techniques are necessary to enhance its long-term performance. Regarding toxicity, both GO and TiO_2 individually pose certain risks, including oxidative stress and potential carcinogenicity. The combined GO/TiO_2 nanocomposites exhibit a complex toxicity profile that varies with concentration and environmental conditions. Research highlights the need for further investigation into the toxicological impacts of these nanocomposites to ensure their safe use in real-world applications, particularly in the aquatic environment. Optimizing their synthesis and mitigating their potential hazards are essential for maximizing the benefits of these photocatalysts, while minimizing their environmental and health risks.

In essence, GO/TiO_2 nanocomposites not only underscore their potential as versatile materials for environmental remediation and sustainable energy generation but also highlight the ongoing research efforts aimed at harnessing their full capabilities for a cleaner and greener future. Continued interdisciplinary research and collaborative efforts are crucial to overcoming the current challenges and unlocking the full potential of these advanced nanomaterials in addressing global environmental and energy challenges.

Data availability

No primary research results, software or code have been included and no new data were generated or analysed as part of this review.

Conflicts of interest

There are no conflicts to declare.

Acknowledgements

References

1 M. A. Abdel-Fatah, *Ain Shams Eng. J.*, 2018, **9**, 3077–3092.

2 E. Guivarch, S. Trevin, C. Lahitte and M. Oturan, *Environ. Chem. Lett.*, 2003, **1**, 38–44.

3 M. Inoue, F. Okada, A. Sakurai and M. Sakakibara, *Ultrason. Sonochem.*, 2006, **13**, 313–320.

4 Z. Ouyang, S. Li, M. Zhao, Q. Wangmu, R. Ding, C. Xiao and X. Guo, *J. Hazard. Mater.*, 2022, **424**, 127461.

5 C. Sánchez, *Biotechnol. Adv.*, 2020, **40**, 107501.

6 N. A. Sacco, F. M. Zoppas, A. Devard, M. González Muñoz, G. García and F. Marchesini, *Microplastics*, 2023, **2**, 278–303.

7 A. Kudo and Y. Miseki, *Chem. Soc. Rev.*, 2009, **38**, 253–278.

8 Q. Xiang, B. Cheng and J. Yu, *Angew. Chem., Int. Ed.*, 2015, **54**, 11350–11366.

9 D. Sajwan, A. Semwal, J. Rawat, H. Sharma and C. Dwivedi, *Mater. Today: Proc.*, 2023, **73**, 180–188.

10 M. Sharma, D. Sajwan, A. Gouda, A. Sharma and V. Krishnan, *Photochem. Photobiol.*, 2024, **100**, 830–896.

11 S. Thakur, A. Ojha, S. K. Kansal, N. K. Gupta, H. C. Swart, J. Cho, A. Kuznetsov, S. Sun and J. Prakash, *Adv. Powder Mater.*, 2024, 100233.

12 Samriti, S. Thakur, A. Ojha, R. Gupta, M. Bechelany, A. Y. Kuznetsov, H. C. Swart and J. Prakash, *Phys. Status Solidi A*, 2024, 2400169.

13 P. Ganguly, S. Panneri, U. Hareesh, A. Breen and S. Pillai, *Nanoscale Mater. Water Purif.*, 2019, 653–688.

14 V. Kumaravel, J. Bartlett and S. Pillai, *ACS Energy Lett.*, 2020, **5**, 486–519.

15 X. Li, J. Yu, J. Low, Y. Fang, J. Xiao and X. Chen, *J. Mater. Chem. A*, 2015, **3**, 2485–2534.

16 Y. Zhu, Q. Lin, Y. Zhong, H. A. Tahini, Z. Shao and H. Wang, *Energy Environ. Sci.*, 2020, **13**, 3361–3392.

17 V. Stanić and S. B. Tanasković, *Nanotoxicity*, 2020, **25**, 241–274.

18 H. Li, Y. Zhou, W. Tu, J. Ye and Z. Zou, *Adv. Funct. Mater.*, 2015, **25**, 998–1013.

19 J. Prakash, S. Sun, H. C. Swart and R. Gupta, *Appl. Mater. Today*, 2018, **11**, 82–135.

20 A. Semwal, D. Sajwan, J. Rawat, L. Gambhir, H. Sharma and C. Dwivedi, *Environ. Sci. Pollut. Res.*, 2023, **30**, 45827–45839.

21 H. Liu, X. Dong, X. Wang, C. Sun, J. Li and Z. Zhu, *Chem. Eng. J.*, 2013, **230**, 279–285.

22 Q. Guo, C. Zhou, Z. Ma and X. Yang, *Adv. Mater.*, 2019, **31**, 1901997.

23 J. Prakash, *Photochem*, 2022, **2**, 651–671.

24 S. Madhusanka, R. Sandaruwan, M. Athar, M. Zaib, H. Arachchige, B. Dassanayake, M. Yoshio and N. Gunawardhana, *Int. J. Electrochem. Sci.*, 2020, **15**, 2792–2805.

25 B. Tang, H. Chen, H. Peng, Z. Wang and W. Huang, *Nanomaterials*, 2018, **8**, 105.

26 X. Sun, S. Ji, M. Wang, J. Dou, Z. Yang, H. Qiu, S. Kou, Y. Ji and H. Wang, *J. Alloys Compd.*, 2020, **819**, 153033.

27 B. P. Singh, L. Tyagi, S. Vikal, S. Tyagi, D. Tyagi, M. Rani, K. Sharma, G. Shukla, U. Shanker and Y. Gautam, *Inorg. Chem. Commun.*, 2024, **166**, 112618.

28 Y. Zhang, K. Li, M. Zang, Y. Cheng and H. Qi, *Chemosphere*, 2023, **341**, 140038.

29 N. T. Padmanabhan, N. Thomas, J. Louis, D. T. Mathew, P. Ganguly, H. John and S. Pillai, *Chemosphere*, 2021, **271**, 129506.

30 V. Dutta, P. Singh, P. Shandilya, S. Sharma, P. Raizada, A. K. Saini, V. K. Gupta, A. Hosseini-Bandegharaei, S. Agarwal and A. Rahmani-Sani, *J. Environ. Chem. Eng.*, 2019, **7**, 103132.

31 P. Kuang, M. Sayed, J. Fan, B. Cheng and J. Yu, *Adv. Energy Mater.*, 2020, **10**, 1903802.

32 J. Campos-Delgado and M. Mendoza, *Materials*, 2023, **17**, 135.

33 E. Kong, J. Chau, C. Lai, C. Khe, G. Sharma, A. Kumar, S. Siengchin and M. Sanjay, *Nanomaterials*, 2022, **12**, 3536.

34 K. Govindan, A. Suresh, T. Sakthivel, K. Murugesan, R. Mohan, V. Gunasekaran and A. Jang, *Chemosphere*, 2019, **237**, 124479.

35 I. S. Sandhu, M. Chitkara, S. Rana, G. Dhillon, A. Taneja and S. Kumar, *Opt. Quantum Electron.*, 2020, **52**, 359.

36 P. Pizarro, C. Guillard, N. Perol and J. Herrmann, *Catal. Today*, 2005, **101**, 211–218.

37 A. Fujishima and K. Honda, *Nature*, 1972, **238**, 37–38.

38 K. Hashimoto, H. Irie and A. Fujishima, *Jpn. J. Appl. Phys.*, 2005, **44**, 8269.

39 P. M. Gore, M. Naebe, X. Wang and B. Kandasubramanian, *J. Hazard. Mater.*, 2022, **426**, 127822.

40 A. J. Haider, R. Anbari, G. R. Kadhim and C. Salame, *Energy Procedia*, 2017, **119**, 332–345.

41 H. Dharma, J. Jaafar, N. Widiastuti, H. Matsuyama, S. Rajabsadeh, M. Othman, M. A. Rahman, N. Jafri, N. S. Suhaimin and A. Nasir, *Membranes*, 2022, **12**, 345.

42 D. Boykobilov, S. Thakur, A. Samiev, A. Nasimov, K. Turaev, S. Nurmanov, J. Prakash and O. Ruzimuradov, *Inorg. Chem. Commun.*, 2024, **170**, 113419.

43 T. Gupta, J. Cho and J. Prakash, *Mater. Today Chem.*, 2021, **20**, 100428.

44 N. Singh, J. Prakash and R. Gupta, *Mol. Syst. Des. Eng.*, 2017, **2**, 422–439.

45 D. Sajwan, A. Semwal, J. Rawat, H. Sharma and C. Dwivedi, *Mater. Today: Proc.*, 2023, **73**, 180–188.

46 S. M. George and B. Kandasubramanian, *Ceram. Int.*, 2020, **46**, 8522–8535.

47 N. Prakash and B. Kandasubramanian, *J. Alloys Compd.*, 2021, **862**, 158547.

48 S. Kato and F. Mashio, *Nippon Kagaku Kaishi*, 1964, **67**, 1136–1140.

49 I. S. McLintock and M. Ritchie, *Trans. Faraday Soc.*, 1965, **61**, 1007–1016.

50 R. Singh, P. Kumari, P. D. Chavan, S. Datta and S. Dutta, *Opt. Mater.*, 2017, **73**, 377–383.

51 D. Ljubas, G. Smoljanić and H. Juretić, *J. Environ. Manage.*, 2015, **161**, 83–91.

52 A. Houas, H. Lachheb, M. Ksibi, E. Elaloui, C. Guillard and J. Herrmann, *Appl. Catal., B*, 2001, **31**, 145–157.

53 R. Dariani, A. Esmaeili, A. Mortezaali and S. Dehghanpour, *Optik*, 2016, **127**, 7143–7154.

54 J. Ge, Z. Zhang, Z. Ouyang, M. Shang, P. Liu, H. Li and X. Guo, *Environ. Res.*, 2022, **209**, 112729.

55 G. Yq, J. Li, S. Li, J. Xia and S. Wei, *Phys. Rev. Lett.*, 2009, **102**, 036402.

This journal is © The Royal Society of Chemistry 2025

Catal. Sci. Technol., 2025, **15**, 1702–1770 | **1761**

56 J. Gao, Q. Shen, R. Guan, J. Xue, X. Liu, H. Jia, Q. Li and Y. Wu, *J. CO2 Util.*, 2020, **35**, 205–215.

57 A. Achilleos, E. Hapeshi, N. P. Xekoukoulotakis, D. Mantzavinos and D. Fatta-Kassinos, *Chem. Eng. J.*, 2010, **161**, 53–59.

58 S. Carbonaro, M. N. Sugihara and T. Strathmann, *Appl. Catal., B*, 2013, **129**, 1–12.

59 D. Dimitrakopoulou, I. Rethemiotaki, Z. Frontistis, N. P. Xekoukoulotakis, D. Venieri and D. Mantzavinos, *J. Environ. Manage.*, 2012, **98**, 168–174.

60 X. Van Doorslaer, P. M. Heynderickx, K. Demeestere, K. Debevere, H. Van Langenhove and J. Dewulf, *Appl. Catal., B*, 2012, **111**, 150–156.

61 C. Dai, X. Zhou, Y. Zhang, Y. Duan, Z. Qiang and T. Zhang, *Environ. Technol.*, 2012, **33**, 1101–1109.

62 S. Wu, H. Hu, Y. Lin, J. Zhang and Y. Hu, *Chem. Eng. J.*, 2020, **382**, 122842.

63 M. R. Eskandarian, H. Choi, M. Fazli and M. Rasoulifard, *Chem. Eng. J.*, 2016, **300**, 414–422.

64 D. Mukherjee, A. K. Ray and S. Barghi, *Processes*, 2016, **4**, 13.

65 P. Vanraes, H. Ghodbane, D. Davister, N. Wardenier, A. Nikiforov, Y. P. Verheust, S. W. Van Hulle, O. Hamdaoui, J. Vandamme and J. Van Durme, *Water Res.*, 2017, **116**, 1–12.

66 M. E. Shuman-Goodier and C. Propper, *Sci. Total Environ.*, 2016, **565**, 758–766.

67 J. F. Budarz, E. M. Cooper, C. Gardner, E. Hodzic, P. Ferguson, C. K. Gunsch and M. Wiesner, *J. Hazard. Mater.*, 2019, **372**, 61–68.

68 M. Cruz, C. Gomez, C. J. Duran-Valle, L. M. Pastrana-Martínez, J. L. Faria, A. M. Silva, M. Faraldos and A. Bahamonde, *Appl. Surf. Sci.*, 2017, **416**, 1013–1021.

69 N. Vela, M. Calín, M. J. Yáñez-Gascón, I. Garrido, G. Pérez-Lucas, J. Fenoll and S. Navarro, *J. Photochem. Photobiol., A*, 2018, **353**, 271–278.

70 R. R. Kalantary, Y. Dadban Shahamat, M. Farzadkia, A. Esrafili and H. Asgharnia, *Desalin. Water Treat.*, 2015, **55**, 555–563.

71 T. Matsunaga, R. Tomoda, T. Nakajima, N. Nakamura and T. Komine, *Appl. Environ. Microbiol.*, 1988, **54**, 1330–1333.

72 U. Joost, K. Juganson, M. Visnapuu, M. Mortimer, A. Kahru, E. Nõmmiste, U. Joost, V. Kisand and A. Ivask, *J. Photochem. Photobiol., B*, 2015, **142**, 178–185.

73 R. Coyle, G. Hardiman and K. O'Driscoll, *Case Stud. Chem. Environ. Eng.*, 2020, **2**, 100010.

74 Z. Ma, Q. Jia, C. Tao and B. Han, *Sep. Purif. Technol.*, 2020, **238**, 116402.

75 A. D. Proctor and B. Bartlett, *J. Phys. Chem. C*, 2020, **124**, 17957–17963.

76 L. P. Domínguez-Jaimes, E. I. Cedillo-González, E. Luévano-Hipólito, J. D. Acuña-Bedoya and J. Hernández-López, *J. Hazard. Mater.*, 2021, **413**, 125452.

77 P. Kaewkam, A. Kanchanapaetnukul, J. Khamyan, N. Phadmanee, K. Lin, K. Kobwittaya and S. Sirivithayapakorn, *J. Environ. Chem. Eng.*, 2022, **10**, 108131.

78 J. Lee, R. Busquets, I. Choi, S. Lee, J. Kim and L. Campos, *Water*, 2020, **12**, 3551.

79 I. Nabi, K. Li, H. Cheng, T. Wang, Y. Liu, S. Ajmal, Y. Yang, Y. Feng and L. Zhang, *iScience*, 2020, **23**(7), 101326.

80 J. Yu, Y. Hai and B. Cheng, *J. Phys. Chem. C*, 2011, **115**, 4953–4958.

81 P. Hartmann, D.-K. Lee, B. M. Smarsly and J. Janek, *ACS Nano*, 2010, **4**, 3147–3154.

82 C. Huang, R. Guo, W. Pan, J. Tang, W. Zhou, X. Liu, H. Qin and P. Jia, *Appl. Surf. Sci.*, 2019, **464**, 534–543.

83 M. Kitano, M. Matsuoka, M. Ueshima and M. Anpo, *Appl. Catal., A*, 2007, **325**, 1–14.

84 T. Di, J. Zhang, B. Cheng, J. Yu and J. Xu, *Sci. China: Chem.*, 2018, **61**, 344–350.

85 J. Matos, B. Llano, R. Montaña, P. S. Poon and M. C. Hidalgo, *Environ. Sci. Pollut. Res.*, 2018, **25**, 18894–18913.

86 Y. Ren, Y. Dong, Y. Feng and J. Xu, *Catalysts*, 2018, **8**, 590.

87 A. Balakrishnan, G. J. Gaware and M. Chinthala, *Chemosphere*, 2023, **310**, 136853.

88 Y. Wang, Q. Wang, X. Zhan, F. Wang, M. Safdar and J. He, *Nanoscale*, 2013, **5**, 8326–8339.

89 B. Roul, M. Kumar, M. K. Rajpalke, T. N. Bhat and S. Krupanidhi, *J. Phys. D: Appl. Phys.*, 2015, **48**, 423001.

90 P. Suyana, P. Ganguly, B. N. Nair, A. P. Mohamed, K. Warrier and U. Hareesh, *Environ. Sci.: Nano*, 2017, **4**, 212–221.

91 X. Zhang, Z. Lai, C. Tan and H. Zhang, *Angew. Chem., Int. Ed.*, 2016, **55**, 8816–8838.

92 A. Thomas, A. Fischer, F. Goettmann, M. Antonietti, J. Müller, R. Schlögl and J. Carlsson, *J. Mater. Chem.*, 2008, **18**, 4893–4908.

93 T. Hisatomi, J. Kubota and K. Domen, *Chem. Soc. Rev.*, 2014, **43**, 7520–7535.

94 F. Bonaccorso, L. Colombo, G. Yu, M. Stoller, V. Tozzini, A. C. Ferrari, R. S. Ruoff and V. Pellegrini, *Science*, 2015, **347**, 1246501.

95 G. A. Muller, J. B. Cook, H. Kim, S. H. Tolbert and B. Dunn, *Nano Lett.*, 2015, **15**, 1911–1917.

96 K. Ramesh, B. Gnanavel and M. Shkir, *Diamond Relat. Mater.*, 2021, **118**, 108514.

97 K. S. Novoselov, A. K. Geim, S. Morozov, D. Jiang, Y. Zhang, S. V. Dubonos, I. V. Grigorieva and A. Firsov, *Science*, 2004, **306**, 666–669.

98 C. Lee, X. Wei, J. W. Kysar and J. Hone, *Science*, 2008, **321**, 385–388.

99 Z. Chen, S. Sun and J. Prakash, *Mol. Syst. Des. Eng.*, 2022, **7**, 213–238.

100 I. Riyal, A. Badoni, S. S. Kalura, K. Mishra, H. Sharma, L. Gambhir and C. Dwivedi, *Environ. Sci. Pollut. Res.*, 2023, **30**, 19269–19277.

101 A. Badoni and J. Prakash, *Micro Nano Eng.*, 2024, **22**, 100239.

102 J. Zhao, L. Liu and F. Li, *Graphene oxide: physics and applications*, Springer, 2015, vol. 1, p. 161.

103 Y. Lin, Y. Ksari, J. Prakash, L. Giovanelli, J. Valmalette and J. Themlin, *Carbon*, 2014, **73**, 216–224.

104 A. Ojha, S. Thakur and J. Prakash, *Environ. Adv.*, 2023, **13**, 100402.

1762 | *Catal. Sci. Technol.*, 2025, **15**, 1702–1770

This journal is © The Royal Society of Chemistry 2025

105 H. A. Becerril, J. Mao, Z. Liu, R. M. Stoltenberg, Z. Bao and Y. Chen, *ACS Nano*, 2008, **2**, 463–470.

106 D. Chen, H. Feng and J. Li, *Chem. Rev.*, 2012, **112**, 6027–6053.

107 D. W. Boukhvalov and M. I. Katsnelson, *J. Am. Chem. Soc.*, 2008, **130**, 10697–10701.

108 Abid, P. Sehrawat, S. Islam, P. Mishra and S. Ahmad, *Sci. Rep.*, 2018, **8**, 3537.

109 T. Yeh, F. Chan, C. Hsieh and H. Teng, *J. Phys. Chem. C*, 2011, **115**, 22587–22597.

110 T. Yeh, J. Cihlář, C. Chang, C. Cheng and H. Teng, *Mater. Today*, 2013, **16**, 78–84.

111 S. Bao, Z. Hua, X. Wang, Y. Zhou, C. Zhang, W. Tu, Z. Zou and M. Xiao, *Opt. Express*, 2012, **20**, 28801–28807.

112 Z. Chen, S. Sun and J. Prakash, *Mol. Syst. Des. Eng.*, 2022, **7**, 213–238.

113 X. Li, J. Yu, S. Wageh, A. A. Al-Ghamdi and J. Xie, *Small*, 2016, **12**, 6640–6696.

114 C. Berger, Z. Song, X. Li, X. Wu, N. Brown, C. Naud, D. Mayou, T. Li, J. Hass and A. Marchenkov, *Science*, 2006, **312**, 1191–1196.

115 J. Ito, J. Nakamura and A. Natori, *J. Appl. Phys.*, 2008, **103**, 113712.

116 T. Yeh, J. Cihlář, C. Chang, C. Cheng and H. Teng, *Mater. Today*, 2013, **16**, 78–84.

117 M. Burghard, H. Klauk and K. Kern, *Adv. Mater.*, 2009, **21**, 2586–2600.

118 T. Yeh, F. Chan, C. Hsieh and H. Teng, *J. Phys. Chem. C*, 2011, **115**, 22587–22597.

119 T. F. Yeh, J. M. Syu, C. Cheng, T. H. Chang and H. Teng, *Adv. Funct. Mater.*, 2010, **20**, 2255–2262.

120 T. F. Yeh, C. Teng, S. Chen and H. Teng, *Adv. Mater.*, 2014, **26**, 3297–3303.

121 J. Prakash, *Photochem*, 2022, **2**, 651–671.

122 N. Zhang, M. Yang, S. Liu, Y. Sun and Y. Xu, *Chem. Rev.*, 2015, **115**, 10307–10377.

123 P. Shandilya, D. Mittal, M. Soni, P. Raizada, A. Hosseini-Bandegharaei, A. K. Saini and P. Singh, *J. Cleaner Prod.*, 2018, **203**, 386–399.

124 A. Khan, P. Singh, P. Raizada, A. Khan, A. M. Asiri and M. Alotaibi, *Chemosphere*, 2023, **316**, 137839.

125 X. Li, J. Yu, S. Wageh, A. Al-Ghamdi and J. Xie, *Small*, 2016, **12**, 6640–6696.

126 K. Lu, Y. Li, Z. Tang and Y. Xu, *ACS Mater. Au*, 2021, **1**, 37–54.

127 V. Georgakilas, J. N. Tiwari, K. Kemp, J. Perman, A. Bourlinos, K. S. Kim and R. Zboril, *Chem. Rev.*, 2016, **116**, 5464–5519.

128 H. Zhang, X. Lv, Y. Li, Y. Wang and J. Li, *ACS Nano*, 2010, **4**, 380–386.

129 Z. Chen, S. Sun and J. Prakash, *Mol. Syst. Des. Eng.*, 2022, **7**, 213–238.

130 Y. Shen, S. Yang, P. Zhou, Q. Sun, P. Wang, L. Wan, J. Li, L. Chen, X. Wang and S. Ding, *Carbon*, 2013, **62**, 157–164.

131 K. Krishnamoorthy, R. Mohan and S. Kim, *Appl. Phys. Lett.*, 2011, **98**, 244101.

132 V. Siong, X. Tai, K. Lee, J. Juan and C. Lai, *RSC Adv.*, 2020, **10**, 37905–37915.

133 A. L. James, M. Lenka, N. Pandey, A. Ojha, A. Kumar, R. Saraswat, P. Thareja, V. Krishnan and K. Jasuja, *Nanoscale*, 2020, **12**, 17121–17131.

134 M. Alsagri, A. Laref, B. U. Haq, H. AlQahtani, F. T. Nya, M. Monir, S. Chowdhury, E. Alghamdi, H. Huang and J. Yang, *J. Mol. Struct.*, 2024, **1299**, 137102.

135 S. Thakur, A. Bi, S. Mahmood, S. Sharma, O. Ruzimuradov, R. Gupta, J. Cho and J. Prakash, *Chemosphere*, 2024, **352**, 141483.

136 W. Yu, L. Sisi, Y. Haiyan and L. Jie, *RSC Adv.*, 2020, **10**, 15328–15345.

137 S. Kumar and A. Kumar, *Opt. Mater.*, 2016, **62**, 320–327.

138 H. Hsu, I. Shown, H. Wei, Y. Chang, H. Du, Y. Lin, C. Tseng, C. Wang, L. Chen and Y. Lin, *Nanoscale*, 2013, **5**, 262–268.

139 M. Singh, S. Kaushal, P. Singh and J. Sharma, *J. Photochem. Photobiol., A*, 2018, **364**, 130–139.

140 M. Shabil Sha, H. Anwar, F. N. Musthafa, H. Al-Lohedan, S. Alfarwati, J. R. Rajabathar, J. Khalid Alahmad, J. Cabibihan, M. Karnan and K. Kumar Sadasivuni, *Sci. Rep.*, 2024, **14**, 3608.

141 H. Wang, Y. Zou, W. Wang, Y. Zhang, G. Mailhot, J. Li, F. Wu and L. Luo, *Chemosphere*, 2023, **315**, 137781.

142 M. Singh, N. K. Bajaj, A. Bhardwaj, P. Singh, P. Kumar and J. Sharma, *Adv. Compos. Hybrid Mater.*, 2018, **1**, 759–765.

143 A. M. Abd-Elnaiem, R. F. Abd El-Baki, F. Alsaaq, S. Orzechowska and D. Hamad, *J. Inorg. Organomet. Polym. Mater.*, 2022, **32**, 1191–1205.

144 V. L. E. Siong, K. M. Lee, J. C. Juan, C. W. Lai, X. H. Tai and C. Khe, *RSC Adv.*, 2019, **9**, 37686–37695.

145 C. Wong, C. W. Lai, K. M. Lee and S. Abd Hamid, *Materials*, 2015, **8**, 7118–7128.

146 F. Khurshid, M. Jeyavelan and S. Nagarajan, *Synth. Met.*, 2021, **278**, 116832.

147 T. Nguyen-Phan, V. H. Pham, E. W. Shin, H. Pham, S. Kim, J. Chung, E. J. Kim and S. Hur, *Chem. Eng. J.*, 2011, **170**, 226–232.

148 N. A. Al-Rawashdeh, O. Allabadi and M. Aljarrah, *ACS Omega*, 2020, **5**, 28046–28055.

149 Z.-R. Tang, Y. Zhang, N. Zhang and Y. Xu, *Nanoscale*, 2015, **7**, 7030–7034.

150 X. H. Tai, C. W. Lai, T. Yang, C. Chen, A. H. Abdullah, K. M. Lee and J. Juan, *J. Environ. Chem. Eng.*, 2022, **10**, 108047.

151 Y. Kuang, J. Shang and T. Zhu, *ACS Appl. Mater. Interfaces*, 2019, **12**, 3580–3591.

152 L. Tian, X. Xian, X. Cui, H. Tang and X. Yang, *Appl. Surf. Sci.*, 2018, **430**, 301–308.

153 A. Badoni and J. Prakash, *Micro Nano Eng.*, 2024, **22**, 100239.

154 Samriti, A. Upadhyay, R. Gupta, O. Ruzimuradov and J. Prakash, *Handbook of Green and Sustainable Nanotechnology: Fundamentals, Developments and Applications*, 2023, pp. 1–30.

155 J. Prakash, Z. Chen, S. Saini, G. Zhang and S. Sun, *Front. Energy*, 2024, **18**, 187–205.

This journal is © The Royal Society of Chemistry 2025

Catal. Sci. Technol., 2025, **15**, 1702–1770 | **1763**

156 J. Prakash, S. Sun, H. C. Swart and R. Gupta, *Appl. Mater. Today*, 2018, **11**, 82–135.

157 J. Prakash, P. Kumar, R. Harris, C. Swart, J. Neethling, A. Vuuren and H. Swart, *Nanotechnology*, 2016, **27**, 355707.

158 N. Singh, J. Prakash and R. K. Gupta, *Mol. Syst. Des. Eng.*, 2017, **2**, 422–439.

159 J. Prakash, A. Kumar, H. Dai, B. C. Janegitz, V. Krishnan, H. C. Swart and S. Sun, *Mater. Today Sustain.*, 2021, **13**, 100066.

160 D. Mathivanan, K. S. Devi, G. Sathiyan, A. Tyagi, V. da Silva, B. Janegitz, J. Prakash and R. K. Gupta, *Sens. Actuators, A*, 2021, **328**, 112769.

161 W. Iqbal, B. Tian, M. Anpo and J. Zhang, *Res. Chem. Intermed.*, 2017, **43**, 5187–5201.

162 H. N. Tien, N. T. Khoa, S. H. Hahn, J. Chung, E. Shin and S. Hur, *Chem. Eng. J.*, 2013, **229**, 126–133.

163 S. A. Al-Zahrani, A. M. Khedr, A. M. Alturki and W. El-Yazeed, *J. Mol. Liq.*, 2024, **395**, 123956.

164 N. Elumalai, S. Prabhu, M. Selvaraj, A. Silambarasan, M. Navaneethan, S. Harish, P. Ramu and R. Ramesh, *Chemosphere*, 2022, **291**, 132782.

165 D. Wang, X. Li, J. Chen and X. Tao, *Chem. Eng. J.*, 2012, **198**, 547–554.

166 B. Li, T. Liu, Y. Wang and Z. Wang, *J. Colloid Interface Sci.*, 2012, **377**, 114–121.

167 N. Yusoff, N. Huang, M. Muhamad, S. Kumar, H. Lim and I. Harrison, *Mater. Lett.*, 2013, **93**, 393–396.

168 J. Ahmad and K. Majid, *New J. Chem.*, 2018, **42**, 3246–3259.

169 H. Seema, K. C. Kemp, V. Chandra and K. Kim, *Nanotechnology*, 2012, **23**, 355705.

170 B. Chai, J. Li, Q. Xu and K. Dai, *Mater. Lett.*, 2014, **120**, 177–181.

171 L. M. Pastrana-Martinez, S. Morales-Torres, V. Likodimos, P. Falaras, J. L. Figueiredo, J. L. Faria and A. Silva, *Appl. Catal., B*, 2014, **158**, 329–340.

172 R. Atchudan, T. Edison, S. Perumal, D. Karthikeyan and Y. R. Lee, *J. Photochem. Photobiol., B*, 2016, **162**, 500–510.

173 V. Deepthi, A. Sebastian and B. Vidhya, *J. Sol-Gel Sci. Technol.*, 2023, **105**, 673–682.

174 S. A. Al-Zahrani, A. M. Khedr, A. M. Alturki and W. El-Yazeed, *J. Mol. Liq.*, 2024, **395**, 123956.

175 N. Verma, T. S. Chundawat, H. Chandra and D. Vaya, *ChemistrySelect*, 2024, **9**, e202303022.

176 M. A. Sayem, M. A. H. Suvo, I. M. Syed and M. Bhuiyan, *Results Phys.*, 2024, **58**, 107471.

177 A. S. Alshammari, M. M. Alabdi, A. Abd Alfatah and M. Mohamed, *Mater. Sci. Eng., B*, 2024, **302**, 117202.

178 M. Sharma, H. Sondhi, R. Krishna, S. K. Srivastava, P. Rajput, S. Nigam and M. Joshi, *Environ. Sci. Pollut. Res.*, 2020, **27**, 32076–32087.

179 S. Sehar, F. Sher, S. Zhang, U. Khalid, J. Sulejmanović and E. Lima, *J. Mol. Liq.*, 2020, **313**, 113494.

180 K. Ganesan, V. K. Jothi, A. Natarajan, A. Rajaram, S. Ravichandran and S. Ramalingam, *Arabian J. Chem.*, 2020, **13**, 6802–6814.

181 S. Sagadevan, J. A. Lett, G. K. Weldegebrieal, S. Garg, W. Oh, N. Hamizi and M. Johan, *Catalysts*, 2021, **11**, 1008.

182 B. Ahmed, A. K. Ojha, A. Singh, F. Hirsch, I. Fischer, D. Patrice and A. Materny, *J. Hazard. Mater.*, 2018, **347**, 266–278.

183 N. Kodarkar, M. Deosarkar and B. Bhanvase, *Chem. Eng. Process.*, 2021, **163**, 108367.

184 T. Mollaei, A. Rouhollahi, M. Hadi and F. Rasouli, *Thin Solid Films*, 2024, **798**, 140350.

185 O. Quiroz-Cardoso, S. Oros-Ruiz, A. Solís-Gómez, R. López and R. Gómez, *Fuel*, 2019, **237**, 227–235.

186 J. Zhang, J. Yu, M. Jaroniec and J. Gong, *Nano Lett.*, 2012, **12**, 4584–4589.

187 C. Prasad, Q. Liu, H. Tang, G. Yuvaraja, J. Long, A. Rammohan and G. Zyryanov, *J. Mol. Liq.*, 2020, **297**, 111826.

188 M. N. Hossain, J. Wen and A. Chen, *Sci. Rep.*, 2017, **7**, 3184.

189 J. Yu, J. Jin, B. Cheng and M. Jaroniec, *J. Mater. Chem. A*, 2014, **2**, 3407–3416.

190 R. Giovannetti, E. Rommozzi, M. Zannotti and C. D'Amato, *Catalysts*, 2017, **7**, 305.

191 L. M. Pastrana-Martínez, S. Morales-Torres, V. Likodimos, J. L. Figueiredo, J. L. Faria, P. Falaras and A. Silva, *Appl. Catal., B*, 2012, **123**, 241–256.

192 R. Raliya, C. Avery, S. Chakrabarti and P. Biswas, *Appl. Nanosci.*, 2017, **7**, 253–259.

193 A. Morawski, E. Kusiak-Nejman, A. Wanag, J. Kapica-Kozar, R. Wróbel, B. Ohtani, M. Aksienionek and L. Lipińska, *Catal. Today*, 2017, **280**, 108–113.

194 P. Gao, A. Li, D. Sun and W. Ng, *J. Hazard. Mater.*, 2014, **279**, 96–104.

195 T. Sreeprasad and V. Berry, *Small*, 2013, **9**, 341–350.

196 H. Bai, C. Li and G. Shi, *Adv. Mater.*, 2011, **23**, 1089–1115.

197 X. Huang, X. Qi, F. Boey and H. Zhang, *Chem. Soc. Rev.*, 2012, **41**, 666–686.

198 C. Qu, S. Wang, L. Ding, M. Zhang, D. Wang and J. Giesy, *Chemosphere*, 2018, **205**, 244–252.

199 L. P. Lingamdinne, J. R. Koduru and R. Karri, *J. Environ. Manage.*, 2019, **231**, 622–634.

200 M. Ruidíaz-Martínez, M. A. Álvarez, M. V. López-Ramón, G. Cruz-Quesada, J. Rivera-Utrilla and M. Sánchez-Polo, *Catalysts*, 2020, **10**, 520.

201 V. Manikandan, A. Palai, S. Mohanty and S. Nayak, *J. Alloys Compd.*, 2019, **793**, 400–409.

202 J. Shen, B. Yan, M. Shi, H. Ma, N. Li and M. Ye, *J. Mater. Chem.*, 2011, **21**, 3415–3421.

203 M. Nawaz, W. Miran, J. Jang and D. Lee, *Appl. Catal., B*, 2017, **203**, 85–95.

204 M. Najafi, A. Kermanpur, M. R. Rahimipour and A. Najafizadeh, *J. Alloys Compd.*, 2017, **722**, 272–277.

205 V. Manikandan, A. Palai, S. Mohanty and S. Nayak, *J. Alloys Compd.*, 2019, **793**, 400–409.

206 S. Jiang, R. Wang, M. Pang, H. Wang, S. Zeng, X. Yue, L. Ni, S. Qiu and Z. Zhang, *Chem. Eng. J.*, 2015, **280**, 614–622.

207 H. R. Pant, S. P. Adhikari, B. Pant, M. K. Joshi, H. Kim, C. H. Park and C. Kim, *J. Colloid Interface Sci.*, 2015, **457**, 174–179.

1764 | *Catal. Sci. Technol.*, 2025, **15**, 1702–1770

This journal is © The Royal Society of Chemistry 2025

208 V. Kumar, R. Madan and D. Mohan, *J. Mater. Sci.: Mater. Electron.*, 2022, **33**, 7655–7667.

209 S. A. Khan, Z. Arshad, S. Shahid, I. Arshad, K. Rizwan, M. Sher and U. Fatima, *Composites, Part B*, 2019, **175**, 107120.

210 A. Tayel, A. R. Ramadan and O. El Seoud, *Catalysts*, 2018, **8**, 491.

211 R. Yuan, H. Wen, L. Zeng, X. Li, X. Liu and C. Zhang, *Nanomaterials*, 2021, **11**, 694.

212 D. Raj and S. K. Maiti, *Environ. Monit. Assess.*, 2019, **191**, 566.

213 I. Ayala, E. Mejía-Ospino, C. Gonzalez-Arias, R. Cabanzo-Hernández and E. V. Niño, *J. Phys.: Conf. Ser.*, 2024, **2726**, 012003.

214 T. Li, T. Wang, G. Qu, D. Liang and S. Hu, *Environ. Sci. Pollut. Res.*, 2017, **24**, 12416–12425.

215 H. M. Yadav and J. Kim, *J. Alloys Compd.*, 2016, **688**, 123–129.

216 O. Ajala, J. Tijani, M. Bankole and A. Abdulkareem, *Environ. Nanotechnol., Monit. Manage.*, 2022, **18**, 100673.

217 M. Hamadanian, M. Rostami and V. Jabbari, *J. Mater. Sci.: Mater. Electron.*, 2017, **28**, 15637–15646.

218 V. Štengl, S. Bakardjieva, T. M. Grygar, J. Bludská and M. Kormunda, *Chem. Cent. J.*, 2013, **7**, 1–12.

219 A. Velasco-Hernández, R. Esparza-Muñoz, F. de Moure-Flores, J. Santos-Cruz and S. Mayén-Hernández, *Mater. Sci. Semicond. Process.*, 2020, **114**, 105082.

220 X. Ma, Y. Liu, H. Liu, L. Zhang, B. Xu and F. Xiao, *Sol. Energy Mater. Sol. Cells*, 2018, **188**, 73–80.

221 M. Ge, S. Li, J. Huang, K. Zhang, S. Al-Deyab and Y. Lai, *J. Mater. Chem. A*, 2015, **3**, 3491–3499.

222 C. P. Athanasekou, S. Morales-Torres, V. Likodimos, G. E. Romanos, L. M. Pastrana-Martinez, P. Falaras, D. Dionysiou, J. Faria, J. Figueiredo and A. Silva, *Appl. Catal., B*, 2014, **158**, 361–372.

223 S. Rajoria, M. Vashishtha and V. K. Sangal, *Environ. Sci. Pollut. Res.*, 2023, **30**, 71226–71251.

224 T. J. Al-Musawi, P. Rajiv, N. Mengelizadeh, I. A. Mohammed and D. Balarak, *J. Environ. Manage.*, 2021, **292**, 112777.

225 K. Wenderich and G. Mul, *Chem. Rev.*, 2016, **116**, 14587–14619.

226 A. Nasir, A. Mazare, X. Zhou, S. Qin, N. Denisov, L. Zdrazil, Š. Kment, R. Zboril, T. Yasin and P. Schmuki, *ChemPhotoChem*, 2022, **6**, e202100274.

227 V. Madurai Ramakrishnan, M. N. S. Pitchaiya, A. Pugazhendhi and D. Velauthapillai, *Int. J. Energy Res.*, 2021, **45**, 17220–17232.

228 H. Afzal, S. Mitu and M. Al-Harthi, *Surf. Interfaces*, 2018, **13**, 65–78.

229 H. Rasuli, R. Rasuli, M. Alizadeh and G. BoonTong, *Results Phys.*, 2020, **18**, 103200.

230 S. Setiawan, A. Hardiansyah, C. Kartikowati, A. Arif, S. Priatmoko and O. Arutanti, *IOP Conf. Ser.:Mater. Sci. Eng.*, 2021, **1143**, 012055.

231 F. C. Romeiro, S. C. Silva, E. Nossol and R. Lima, *New J. Chem.*, 2020, **44**, 6825–6832.

232 M. Gijare, S. Chaudhari, S. Ekar and A. Garje, *Adv. Nat. Sci.: Nanosci. Nanotechnol.*, 2021, **12**, 035015.

233 H. Wang, H. Gao, M. Chen, X. Xu, X. Wang, C. Pan and J. Gao, *Appl. Surf. Sci.*, 2016, **360**, 840–848.

234 Y. Yang, E. Liu, J. Fan, X. Hu, W. Hou, F. Wu and Y. Ma, *Russ. J. Phys. Chem. A*, 2014, **88**, 478–483.

235 J. Schneider, M. Matsuoka, M. Takeuchi, J. Zhang, Y. Horiuchi, M. Anpo and D. Bahnemann, *Chem. Rev.*, 2014, **114**, 9919–9986.

236 J. Zhang, P. Zhou, J. Liu and J. Yu, *Phys. Chem. Chem. Phys.*, 2014, **16**, 20382–20386.

237 G. Moon, D. Kim, H. Kim, A. D. Bokare and W. Choi, *Environ. Sci. Technol. Lett.*, 2014, **1**, 185–190.

238 E. Kusiak-Nejman and A. Morawski, *Appl. Catal., B*, 2019, **253**, 179–186.

239 M. Yang and Y. Xu, *J. Phys. Chem. C*, 2013, **117**, 21724–21734.

240 H. Zhang, X. Lv, Y. Li, Y. Wang and J. Li, *ACS Nano*, 2010, **4**, 380–386.

241 Y. T. Liang, B. K. Vijayan, O. Lyandres, K. A. Gray and M. Hersam, *J. Phys. Chem. Lett.*, 2012, **3**, 1760–1765.

242 G. Hu and B. Tang, *Mater. Chem. Phys.*, 2013, **138**, 608–614.

243 Y. Ni, W. Wang, W. Huang, C. Lu and Z. Xu, *J. Colloid Interface Sci.*, 2014, **428**, 162–169.

244 E. Kusiak-Nejman, A. Wanag, J. Kapica-Kozar, Ł. Kowalczyk, M. Zgrzebnicki, B. Tryba, J. Przepiórski and A. Morawski, *Catal. Today*, 2020, **357**, 630–637.

245 D. Zhao, G. Sheng, C. Chen and X. Wang, *Appl. Catal., B*, 2012, **111**, 303–308.

246 Y. Nosaka and A. Nosaka, *Chem. Rev.*, 2017, **117**, 11302–11336.

247 A. G. Rincón, C. Pulgarin, N. Adler and P. Peringer, *J. Photochem. Photobiol., A*, 2001, **139**, 233–241.

248 Y. Zhu, S. Murali, W. Cai, X. Li, J. W. Suk, J. R. Potts and R. Ruoff, *Adv. Mater.*, 2010, **22**, 3906–3924.

249 S. J. Rowley-Neale, E. P. Randviir, A. Dena and C. Banks, *Appl. Mater. Today*, 2018, **10**, 218–226.

250 A. RoyChowdhury, R. Datta and D. Sarkar, *Green Chem.*, 2018, 359–373.

251 Y. M. Hunge, A. A. Yadav, A. G. Dhodamani, N. Suzuki, C. Terashima, A. Fujishima and V. L. Mathe, *Ultrason. Sonochem.*, 2020, **61**, 104849.

252 S. Sheshmani and M. Nayebi, *Polym. Compos.*, 2019, **40**, 210–216.

253 K. Stepić, R. Ljupković, J. Ickovski and A. Zarubica, *Advanced Technologies*, 2021, **10**, 51–60.

254 A. Das, M. K. Adak, N. Mahata and B. Biswas, *J. Mol. Liq.*, 2021, **338**, 116479.

255 R. Atchudan, T. Edison, S. Perumal, D. Karthikeyan and Y. Lee, *J. Photochem. Photobiol., A*, 2017, **333**, 92–104.

256 M. Sharma, K. Behl, S. Nigam and M. Joshi, *Vacuum*, 2018, **156**, 434–439.

257 H. Garrafa-Gálvez, C. Alvarado-Beltrán, J. L. Almaral-Sánchez, A. Hurtado-Macías, A. M. Garzon-Fontecha, P. A. Luque and A. Castro-Beltrán, *Chem. Phys.*, 2019, **521**, 35–43.

258 M. Adly, S. M. El-Dafrawy and S. El-Hakam, *J. Mater. Res. Technol.*, 2019, **8**, 5610–5622.

This journal is © The Royal Society of Chemistry 2025

Catal. Sci. Technol., 2025, **15**, 1702–1770 | **1765**

259 Y. J. R. a. Liu, *RSC Adv.*, 2014, **4**, 36040–36045.

260 S. Preetha, S. Ramamoorthy, R. Pillai, B. Narasimhamurthy and I. Lekshmi, *Mater. Today: Proc.*, 2022, **62**, 5605–5612.

261 T. A. Kurniawan, Z. Mengting, D. Fu, S. Yeap, M. Othman, R. Avtar and T. Ouyang, *J. Environ. Manage.*, 2020, **270**, 110871.

262 T. Al-Musawi, P. Rajiv, N. Mengelizadeh, I. A. Mohammed and D. Balarak, *J. Environ. Manage.*, 2021, **292**, 112777.

263 Y. Liang, H. Wang, H. Sanchez Casalongue, Z. Chen and H. Dai, *Nano Res.*, 2010, **3**, 701–705.

264 T. Lavanya, M. Dutta, S. Ramaprabhu and K. Satheesh, *J. Environ. Chem. Eng.*, 2017, **5**, 494–503.

265 C. Lin, Y. Gao, J. Zhang, D. Xue, H. Fang, J. Tian, C. Zhou, C. Zhang, Y. Li and H. Li, *J. Mater. Res.*, 2020, **35**, 1307–1315.

266 A. S. Ahmed, T. Ahamad, N. Ahmad and M. Khan, *Mater. Chem.*, 2019, **238**, 121906.

267 V. Kumaran, P. Sudhagar, A. K. Konga and G. Ponniah, *Pol. J. Environ. Stud.*, 2020, **29**, 1683–1690.

268 V. Keerthana, *Iran. J. Sci. Technol. Trans. A: Sci.*, 2022, **46**, 1149–1161.

269 M. Kocijan, L. Ćurković, I. Bdikin, G. Otero-Irurueta, M. J. Hortigüela, G. Gonçalves, T. Radošević, D. Vengust and M. Podlogar, *Appl. Sci.*, 2021, **12**, 385.

270 S. H. Alwan, K. H. Salem and H. Alshamsi, *Mater. Today Commun.*, 2022, **33**, 104558.

271 M. Kocijan, L. Ćurković, D. Ljubas, K. Mužina, I. Bačić, T. Radošević, M. Podlogar, I. Bdikin, G. Otero-Irurueta and M. Hortigüela, *Appl. Sci.*, 2021, **11**, 3966.

272 S. Preetha, R. Pillai, S. Ramamoorthy, A. Mayeen, K. Archana, N. Kalarikkal, B. Narasimhamurthy and I. Lekshmi, *Surf. Interfaces*, 2022, **30**, 101812.

273 D. John, A. Rajalakshmi, R. M. Lopez and V. Achari, *SN Appl. Sci.*, 2020, **2**, 840.

274 Q. Zhou, Y. Zhong, X. Chen, X. Huang and Y. Wu, *Mater. Res. Bull.*, 2014, **51**, 244–250.

275 L. M. Pastrana-Martínez, S. Morales-Torres, V. Likodimos, J. L. Figueiredo, J. Faria, P. Falaras and A. Silva, *Appl. Catal., B*, 2012, **123**, 241–256.

276 Y. Zhang, X. Hou, T. Sun and X. Zhao, *Ceram. Int.*, 2017, **43**, 1150–1159.

277 Á. Tolosana-Moranchel, A. Manassero, M. L. Satuf, O. M. Alfano, J. Casas and A. Bahamonde, *Appl. Catal., B*, 2019, **246**, 1–11.

278 J. Leal, S. Cruz, B. Almeida, V. Esteves, P. Marques and E. Santos, *Environ. Sci.: Water Res. Technol.*, 2020, **6**, 1018–1027.

279 I. Appavoo, J. Hu, Y. Huang, S. Li and S. Ong, *Water Res.*, 2014, **57**, 270–279.

280 N. F. Moreira, C. Narciso-da-Rocha, M. I. Polo-Lopez, L. Pastrana-Martínez, J. Faria, C. M. Manaia, P. Fernández-Ibáñez, O. Nunes and A. Silva, *Water Res.*, 2018, **135**, 195–206.

281 M. Cruz, C. Gomez, C. J. Duran-Valle, L. M. Pastrana-Martínez, J. L. Faria, A. M. Silva, M. Faraldos and A. Bahamonde, *Appl. Surf. Sci.*, 2017, **416**, 1013–1021.

282 M. J. Sampaio, C. G. Silva, A. M. Silva, L. M. Pastrana-Martínez, C. Han, S. Morales-Torres, J. L. Figueiredo, D. Dionysiou and J. Faria, *Appl. Catal., B*, 2015, **170**, 74–82.

283 P. Karaolia, I. Michael-Kordatou, E. Hapeshi, C. Drosou, Y. Bertakis, D. Christofilos, G. S. Armatas, L. Sygellou, T. Schwartz and N. Xekoukoulotakis, *Appl. Catal., B*, 2018, **224**, 810–824.

284 H. Wang, M. Zhang, X. He, T. Du, Y. Wang, Y. Li and T. Hao, *Water Res.*, 2019, **160**, 197–205.

285 M. López-Ramón, M. Ruidíaz-Martínez, M. Álvarez, G. Cruz-Quesada, J. Rivera-Utrilla and M. J. W. Sánchez-Polo, *Water*, 2019, **19**, 22–24.

286 Z. Gholamvande, A. Morrissey, K. Nolan and J. Tobin, 2012.

287 P. Calza, C. Hadjicostas, V. Sakkas, M. Sarro, C. Minero, C. Medana and T. Albanis, *Appl. Catal., B*, 2016, **183**, 96–106.

288 X. Tai, C. Lai, T. Yang, M. Johan, K. M. Lee, C. Chen and J. Juan, *J. Environ. Chem. Eng.*, 2022, **10**, 107304.

289 Z. Zhou, J. Gao, G. Zhang, Y. Dong, Z. Wang, J. Li and J. Lyu, *Ceram. Int.*, 2020, **46**, 5887–5893.

290 W. Lin, X. Xie, X. Wang, Y. Wang, D. Segets and J. Sun, *Chem. Eng. J.*, 2018, **349**, 708–718.

291 G. Wang, W. Guo, D. Xu, D. Liu and M. Qin, *Symmetry*, 2020, **12**, 1420.

292 N. L. M. Tri, K. Jitae, D. Van Thuan, P. T. Huong and T. Al Tahtamouni, *Mater. Res. Express*, 2019, **6**, 105509.

293 W. Chen, J. Chen, J. Zhang, R. Luo, H. Yang, G. Wang and R. Wang, *Mater. Res. Express*, 2019, **6**, 105503.

294 M. Roso, C. Boaretti, M. G. Pelizzo, A. Lauria, M. Modesti and A. Lorenzetti, *Ind. Eng. Chem. Res.*, 2017, **56**, 9980–9992.

295 C. Zhu, G. Li, Z. Lian, Z. Wan, R. Huang, S. Zhang and Q. Zhong, *Sep. Purif. Technol.*, 2021, **276**, 119362.

296 A. Trapalis, N. Todorova, T. Giannakopoulou, N. Boukos, T. Speliotis, D. Dimotikali and J. Yu, *Appl. Catal., B*, 2016, **180**, 637–647.

297 G. Luna-Sanguino, A. Ruíz-Delgado, A. Tolosana-Moranchel, L. Pascual, S. Malato, A. Bahamonde and M. Faraldos, *Sci. Total Environ.*, 2020, **737**, 140286.

298 M. Maiti, M. Sarkar and D. Liu, *Catal. Sci. Technol.*, 2020, **10**, 2797–2809.

299 P. Nian, L. Peng, J. Feng, X. Han, B. Cui, S. Lu, J. Zhang, Q. Liu and A. Zhang, *Sep. Purif. Technol.*, 2019, **211**, 832–842.

300 Y. Lin, C. Huang, Y.-H. Wang and J. Wu, *Top. Catal.*, 2020, **63**, 1240–1250.

301 H. Fan, G. Yi, Z. Zhang, X. Zhang, P. Li, C. Zhang, L. Chen, Y. Zhang and Q. Sun, *Opt. Mater.*, 2021, **120**, 111482.

302 H. Kaur, R. Dahake, P. R. Maddigapu, G. Hippargi, G. R. Pophali and A. Bansiwal, *J. Mater. Sci.: Mater. Electron.*, 2020, **31**, 6045–6058.

303 S. Liu, T. Jiang, M. Fan, G. Tan, S. Cui and X. Shen, *J. Alloys Compd.*, 2021, **861**, 158598.

304 J. H. Seinfeld and S. N. Pandis, *Atmospheric chemistry and physics: from air pollution to climate change*, John Wiley & Sons, 2016.

305 R. Pérez-Padilla, A. Schilmann and H. Riojas-Rodriguez, *Int. J. Tuberc. Lung. Dis.*, 2010, **14**, 1079–1086.

1766 | *Catal. Sci. Technol.*, 2025, **15**, 1702–1770

This journal is © The Royal Society of Chemistry 2025

306 F. Sánchez-Soberón, J. Rovira, J. Sierra, M. Mari, J. Domingo and M. Schuhmacher, *Environ. Res.*, 2019, **175**, 287–296.

307 J. Ângelo, L. Andrade, L. Madeira and A. Mendes, *J. Environ. Manage.*, 2013, **129**, 522–539.

308 C. Guerreiro, *Air quality in Europe: 2013 report*, 2013.

309 A. H. Goldstein and I. E. Galbally, *Environ. Sci. Technol.*, 2007, **41**, 1514–1521.

310 F. Mushtak, J. Prakash and S. Katoch, *Micro Nano Eng.*, 2024, **22**, 100237.

311 D. Sajwan, A. Sharma, M. Sharma and V. Krishnan, *ACS Catal.*, 2024, **14**, 4865–4926.

312 I. Uogintė, S. Pleskytė, M. Skapas, S. Stanionytė and G. Lujanienė, *Int. J. Environ. Sci. Technol.*, 2023, **20**, 9693–9706.

313 L. S Dinoop, J. T Sunil, C. Rajesh and K. Arun, *Polym. Degrad. Stab.*, 2021, **184**, 109476.

314 I. Nabi, F. Ahmad and L. Zhang, *J. Environ. Chem. Eng.*, 2021, **9**, 105964.

315 Y. Shi, Z. Yu, Z. Li, X. Zhao and Y. Yuan, *Polymers*, 2021, **13**, 2158.

316 R. Verma, S. Singh, M. Dalai, M. Saravanan, V. Agrawal and A. K. Srivastava, *Mater. Des.*, 2017, **133**, 10–18.

317 C. Wang, P. W. Horby, F. G. Hayden and G. Gao, *Lancet*, 2020, **395**, 470–473.

318 M. Santosham, A. Chandran, S. Fitzwater, C. Fischer-Walker, A. H. Baqui and R. Black, *Lancet*, 2010, **376**, 63–67.

319 W. Kim, W. Zhu, G. L. Hendricks, D. Van Tyne, A. D. Steele, C. Keohane, N. Fricke, A. Conery, S. Shen and W. Pan, *Nature*, 2018, **556**, 103–107.

320 E. D. Brown and G. Wright, *Nature*, 2016, **529**, 336–343.

321 T. Matsunaga, R. Tomoda, T. Nakajima and H. Wake, *FEMS Microbiol. Lett.*, 1985, **29**, 211–214.

322 P. Fernandez-Ibanez, M. Polo-López, S. Malato, S. Wadhwa, J. Hamilton, P. Dunlop, R. D'sa, E. Magee, K. O'shea and D. Dionysiou, *Chem. Eng. J.*, 2015, **261**, 36–44.

323 A. Wanag, P. Rokicka, E. Kusiak-Nejman, J. Kapica-Kozar, R. Wrobel, A. Markowska-Szczupak and A. W. Morawski, *Ecotoxicol. Environ. Saf.*, 2018, **147**, 788–793.

324 B. R. Cruz-Ortiz, J. W. Hamilton, C. Pablos, L. Díaz-Jiménez, D. A. Cortés-Hernández, P. K. Sharma, M. Castro-Alférez, P. Fernández-Ibañez, P. S. Dunlop and J. Byrne, *Chem. Eng. J.*, 2017, **316**, 179–186.

325 J. Prakash, K. S. K. Venkataprasanna, D. Prema, S. M. Sahabudeen, S. Debashree Banita and G. D. Venkatasubbu, *Toxicol. Mech. Methods*, 2020, **30**, 508–525.

326 M. Chai, M. An, X. Zhang and P. Chu, *Rare Met.*, 2022, **41**, 540–545.

327 N. Mammari, E. Lamouroux, A. Boudier and R. Duval, *Microorganisms*, 2022, **10**, 437.

328 X. Zhou, M. Zhou, S. Ye, Y. Xu, S. Zhou, Q. Cai, G. Xie, L. Huang, L. Zheng and Y. Li, *Int. Biodeterior. Biodegrad.*, 2021, **162**, 105260.

329 C. Jin, F. Wang, Y. Tang, X. Zhang, J. Wang and Y. Yang, *Biol. Trace Elem. Res.*, 2014, **159**, 393–398.

330 Y. Chang, X. Ou, G. Zeng, J. Gong, C. Deng, Y. Jiang, J. Liang, G. Yuan, H. Liu and X. He, *Appl. Surf. Sci.*, 2015, **343**, 1–10.

331 A. Raja, K. Selvakumar, P. Rajasekaran, M. Arunpandian, S. Ashokkumar, K. Kaviyarasu, S. A. Bahadur and M. Swaminathan, *Colloids Surf., A*, 2019, **564**, 23–30.

332 O. Akhavan and E. Ghaderi, *J. Phys. Chem. C*, 2009, **113**, 20214–20220.

333 G. Wang, W. Feng, X. Zeng, Z. Wang, C. Feng, D. T. McCarthy, A. Deletic and X. Zhang, *Water Res.*, 2016, **94**, 363–370.

334 M. Meinshausen, N. Meinshausen, W. Hare, S. C. Raper, K. Frieler, R. Knutti, D. Frame and M. Allen, *Nature*, 2009, **458**, 1158–1162.

335 Y. Rambabu, U. Kumar, N. Singhal, M. Kaushal, M. Jaiswal, S. Jain and S. Roy, *Appl. Surf. Sci.*, 2019, **485**, 48–55.

336 S. Solomon, G.-K. Plattner, R. Knutti and P. Friedlingstein, *Proc. Natl. Acad. Sci. U. S. A.*, 2009, **106**, 1704–1709.

337 W. H. Schlesinger, J. F. Reynolds, G. L. Cunningham, L. Huenneke, W. Jarrell, R. Virginia and W. Whitford, *Science*, 1990, **247**, 1043–1048.

338 L. Kimfung, D. Martin and T. Junwang, *Chin. J. Catal.*, 2011, **32**, 879–890.

339 L. Tan, W. Ong, S. Chai, B. Goh and A. Mohamed, *Appl. Catal., B*, 2015, **179**, 160–170.

340 A. Razzaq, C. Grimes and S. In, *Carbon*, 2016, **98**, 537–544.

341 J. O. Olowoyo, M. Kumar, B. Singh, V. Oninla, J. Babalola, H. Valdés, A. Vorontsov and U. Kumar, *Carbon*, 2019, **147**, 385–397.

342 L. Tan, W. Ong, S. Chai and A. Mohamed, *Chem. Eng. J.*, 2017, **308**, 248–255.

343 A. Velasco-Hernández, R. Esparza-Muñoz, F. de Moure-Flores, J. Santos-Cruz and S. Mayén-Hernández, *Mater. Sci. Semicond. Process.*, 2020, **114**, 105082.

344 N. Shehzad, M. Tahir, K. Johari, T. Murugesan and M. Hussain, *J. Environ. Chem. Eng.*, 2018, **6**, 6947–6957.

345 J. Liu, Y. Niu, X. He, J. Qi and X. Li, *J. Nanomater.*, 2016, **1**, 6012896.

346 H. M. Moustafa, M. S. Mahmoud and M. Nassar, *Inorg. Chem. Commun.*, 2022, **141**, 109546.

347 N. Singh, S. Jana, G. P. Singh and R. Dey, *Adv. Compos. Hybrid Mater.*, 2020, **3**, 127–140.

348 B. Hernández-Majalca, M. Meléndez-Zaragoza, J. Salinas-Gutiérrez, A. López-Ortiz and V. Collins-Martínez, *Int. J. Hydrogen Energy*, 2019, **44**, 12381–12389.

349 J. Serafin, E. Kusiak-Nejman, A. Wanag, A. W. Morawski and J. Llorca, *J. Photochem. Photobiol., A*, 2021, **418**, 113406.

350 L. Wang, Y. Li and Y. Liu, *Micro Nano Lett.*, 2017, **12**, 494–496.

351 D. Chen, L. Zou, S. Li and F. Zheng, *Sci. Rep.*, 2016, **6**, 20335.

352 P. K. Dubey, P. Tripathi, R. Tiwari, A. Sinha and O. Srivastava, *Int. J. Hydrogen Energy*, 2014, **39**, 16282–16292.

353 P. Zeng, Q. Zhang, X. Zhang and T. Peng, *J. Alloys Compd.*, 2012, **516**, 85–90.

354 P. Gao and D. Sun, *Chem. – Asian J.*, 2013, **8**, 2779–2786.

355 M. Ni, M. K. Leung, D. Y. Leung and K. Sumathy, *Renewable Sustainable Energy Rev.*, 2007, **11**, 401–425.

This journal is © The Royal Society of Chemistry 2025

Catal. Sci. Technol., 2025, **15**, 1702–1770 | **1767**

356 H. M. Moustafa, V. K. Velisoju, H. O. Mohamed, M. Obaid, P. D. Kolubah, X. Yao, N. Ghaffour and P. Castaño, *Fuel*, 2023, **338**, 127232.

357 G. Nabi, Q. Ain, M. B. Tahir, K. Nadeem Riaz, T. Iqbal, M. Rafique, S. Hussain, W. Raza, I. Aslam and M. Rizwan, *Int. J. Environ. Anal. Chem.*, 2022, **102**, 434–442.

358 M. B. Tahir, S. Farman, M. Rafique, M. Shakil, M. I. Khan, M. Ijaz, I. Mubeen, M. Ashraf and K. Nadeem Riaz, *Int. J. Environ. Anal. Chem.*, 2021, **101**, 1448–1460.

359 M. B. Tahir, S. Hajra, N. Khalid, M. Rizwan and G. Watto, *J. Inorg. Organomet. Polym. Mater.*, 2018, **28**, 1–8.

360 A. Galińska and J. Walendziewski, *Energy Fuels*, 2005, **19**, 1143–1147.

361 X. Cao, G. Tian, Y. Chen, J. Zhou, W. Zhou, C. Tian and H. Fu, *J. Mater. Chem. A*, 2014, **2**, 4366–4374.

362 N. T. Padmanabhan, N. Thomas, J. Louis, D. T. Mathew, P. Ganguly, H. John and S. C. Pillai, *Chemosphere*, 2021, **271**, 129506.

363 Y. Kumar, A. Sudhaik, K. Sharma, P. Raizada, A. Khan, V. Nguyen, T. Ahamad, P. Singh and A. M. Asiri, *J. Photochem. Photobiol., A*, 2023, **435**, 114326.

364 V. Dutta, A. Sudhaik, A. Khan, T. Ahamad, P. Raizada, S. Thakur, A. Asiri and P. Singh, *Mater. Res. Bull.*, 2023, **164**, 112238.

365 A. Kumar, P. Choudhary, A. Kumar, P. H. Camargo and V. Krishnan, *Small*, 2022, **18**, 2101638.

366 O. Mohammadi, M. Golestanzadeh and M. Abdouss, *New J. Chem.*, 2017, **41**, 11471–11497.

367 Y. Tian and T. Tatsuma, *J. Am. Chem. Soc.*, 2005, **127**, 7632–7637.

368 E. Kowalska, O. Mahaney, R. Abe and B. Ohtani, *Phys. Chem. Chem. Phys.*, 2010, **12**, 2344–2355.

369 Y. Xiao, Y. Huang, S. Xue and J. Zhao, *Appl. Catal., B*, 2020, **265**, 118596.

370 M. K. Aulakh, R. Sharma, B. Pal and R. Prakash, *Sol. Energy*, 2020, **196**, 427–436.

371 Q. Zhang, X. Jin, Z. Xu, J. Zhang, U. F. Rendón, L. Razzari, M. Chaker and D. Ma, *J. Phys. Chem. Lett.*, 2018, **9**, 5317–5326.

372 J. Soni, A. Sethiya, N. Sahiba and S. Agarwal, *Appl. Organomet. Chem.*, 2021, **35**, e6162.

373 K. Samal, M. R. Swain and A. Pati, *ChemistrySelect*, 2023, **8**, e202302026.

374 D. Laurenti, P. Afanasiev and C. Geantet, *Appl. Catal., B*, 2011, **101**, 239–245.

375 D. Kubička, J. Horáček, M. Setnička, R. Bulánek, A. Zukal and I. Kubičková, *Appl. Catal., B*, 2014, **145**, 101–107.

376 M. Masteri-Farahani, M.-S. Hosseini and N. Forouzeshfar, *Renewable Energy*, 2020, **151**, 1092–1101.

377 R. Gupta, S. Paul and R. Gupta, *J. Mol. Catal. A: Chem.*, 2007, **266**, 50–54.

378 J. Soni, N. Sahiba, A. Sethiya, P. Teli, D. Agarwal, A. Manhas, P. Jha, D. Joshi and S. Agarwal, *Polycyclic Aromat. Compd.*, 2022, **42**, 2970–2990.

379 M. Heravi, S. Asadi, S. M. Hoseini Chopani and E. Jaderi, *Appl. Organomet. Chem.*, 2020, **34**, e5805.

380 S. Moussa, A. R. Siamaki, B. F. Gupton and M. El-Shall, *ACS Catal.*, 2012, **2**, 145–154.

381 L. Lombardi and M. Bandini, *Angew. Chem.*, 2020, **132**, 20951–20962.

382 B. Jain, A. Hashmi, S. Sanwaria, A. K. Singh, M. Susan and A. Singh, *Adv. Compos. Hybrid Mater.*, 2020, **3**, 231–242.

383 Z. Durmus, B. Kurt and A. Durmus, *ChemistrySelect*, 2019, **4**, 271–278.

384 S. Shaheen, A. Iqbal, M. Ikram, M. Imran, S. Naz, A. Ul-Hamid, A. Shahzadi, W. Nabgan, J. Haider and A. Haider, *Appl. Nanosci.*, 2022, **12**, 165–177.

385 J. Zhang, S. Shao, D. Zhou, Q. Xu and T. Wang, *J. CO2 Util.*, 2021, **50**, 101584.

386 M. T. Genç, A. Sarilmaz, S. Dogan, İ. Çekceoğlu, A. Ozen, E. Aslan, B. Okan, J. Jaafar, F. Ozel and M. Ersoz, *Int. J. Hydrogen Energy*, 2023, **48**, 30407–30419.

387 A. Yadav, Y. Hunge and S. Kang, *Surf. Interfaces*, 2021, **24**, 101075.

388 H. M. Mashhoor, M. Eftekhari, N. Rezazadeh and M. Nazarabad, *Nanotechnol. Environ. Eng.*, 2023, **8**, 75–86.

389 Y. Li, M. Ti, Z. Li, Y. Zhang, L. Wu and Y. He, *J. Mater. Sci.: Mater. Electron.*, 2021, **32**, 2268–2282.

390 G. Jeevitha, R. Abhinayaa, D. Mangalaraj and N. Ponpandian, *J. Phys. Chem. Solids*, 2018, **116**, 137–147.

391 Y. Li, K. Jiang, J. Yang, Y. Zheng, R. Hübner, Z. Ou, X. Dong, L. He, H. Wang and J. Li, *Small*, 2021, **17**, 2102159.

392 N. Wang, F. Zhang, Q. Mei, R. Wu and W. Wang, *Water, Air, Soil Pollut.*, 2020, **231**, 1–10.

393 R. Banu, N. Salvi, S. Gupta, C. Ameta, R. Ameta and P. B. Punjabi, *Arabian J. Sci. Eng.*, 2022, **47**, 1–14.

394 F. Anjum, M. Shaban, M. Ismail, S. Gul, E. M. Bakhsh, M. A. Khan, U. Sharafat, S. B. Khan and M. Khan, *ACS Omega*, 2023, **8**, 17667–17681.

395 H. Chen, W. Ji, M. Gu, Y. Li and X. Cheng, *J. Mater. Sci.: Mater. Electron.*, 2021, **32**, 27564–27575.

396 E. A. Jafari, M. Moradi, S. Hajati, M. A. Kiani and J. Espinos, *Electrochim. Acta*, 2018, **268**, 392–402.

397 P. G. Ramos, C. Luyo, L. A. Sánchez, E. D. Gomez and J. Rodriguez, *Catalysts*, 2020, **10**, 660.

398 N. Kumaresan and K. Ramamurthi, *J. Mater. Sci.: Mater. Electron.*, 2020, **31**, 3361–3374.

399 A. Jana and D. Gregory, *Chem. – Eur. J.*, 2020, **26**, 6703–6714.

400 W. M. Liu, J. Li and H. Zhang, *Optik*, 2020, **207**, 163778.

401 Y. Lin, R. Hong, H. Chen, D. Zhang and J. Xu, *J. Nanomater.*, 2020, **2020**, 1–11.

402 T. Govindaraj, C. Mahendran, V. Manikandan, J. Archana, M. Shkir and J. Chandrasekaran, *J. Alloys Compd.*, 2021, **868**, 159091.

403 M. Y. Khan, M. Ahmad, S. Sadaf, S. Iqbal, F. Nawaz and J. Iqbal, *J. Mater. Res. Technol.*, 2019, **8**, 3261–3269.

404 B. Mandal, J. Panda and B. Tudu, *AIP Conference Proceedings*, 2018, May, vol. 1953.

405 T. Kim, V. G. Parale, H.- Jung, Y. Kim, Z. Driss, D. Driss, A. Bouabidi, S. Euchy and H. Park, *Nanomaterials*, 2019, **9**, 358.

1768 | *Catal. Sci. Technol.*, 2025, **15**, 1702–1770

This journal is © The Royal Society of Chemistry 2025

406 N. Yusoff, S. V. Kumar, A. Pandikumar, N. Huang, A. Marlinda and M. An'Amt, *Ceram. Int.*, 2015, **41**, 5117–5128.

407 J. Louis, N. T. Padmanabhan, M. K. Jayaraj and H. John, *Mater. Res. Bull.*, 2024, **169**, 112542.

408 W. Hu, Y. Chen, P. Hsieh, C. Tsao, Y. Chiu, T. M. Chang, C. Chen, M. Sone and Y. Hsu, *J. Taiwan Inst. Chem. Eng.*, 2020, **112**, 337–344.

409 M. Tayebi, A. Tayyebi, Z. Masoumi and B. Lee, *Appl. Surf. Sci.*, 2020, **502**, 144189.

410 S. Chandrasekaran, J. S. Chung, E. J. Kim and S. Hur, *Chem. Eng. J.*, 2016, **290**, 465–476.

411 A. Yadav, Y. Hunge and S. Kang, *Mater. Res. Bull.*, 2021, **133**, 111026.

412 Y. Huang, C. Yan, C. Guo, Z. Lu, Y. Shi and Z. Wang, *Int. J. Hydrogen Energy*, 2017, **42**, 4007–4016.

413 L. Zhang, N. Li, H. Jiu, G. Qi and Y. Huang, *Ceram. Int.*, 2015, **41**, 6256–6262.

414 S. Liu, J. Lu, Y. Pu and H. Fan, *J. CO2 Util.*, 2019, **33**, 171–178.

415 A. Karawek, K. Kittipoom, L. Tansuthepverawongse, N. Kitjanukit, W. Neamsung, N. Lertthanaphol, P. Chanthara, S. Ratchahat, P. Phadungbut and P. Kim-Lohsoontorn, *Nanomaterials*, 2023, **13**, 320.

416 Q. Wang, K. Chen, S. Wang, Y. Li, L. Zeng, C. Ma, D. Jiang, L. Zhu and X. Xu, *J. Alloys Compd.*, 2021, **887**, 161457.

417 R. Gusain, P. Kumar, O. P. Sharma, S. L. Jain and O. Khatri, *Appl. Catal., B*, 2016, **181**, 352–362.

418 W. Kohn, A. D. Becke and R. G. Parr, *J. Phys. Chem.*, 1996, **100**, 12974–12980.

419 F. T. Geldasa, M. A. Kebede, M. W. Shura and F. G. Hone, *RSC Adv.*, 2023, **13**, 18404–18442.

420 M. Ikram, M. A. U. Haq, A. Haider, J. Haider, A. Ul-Hamid, I. Shahzadi, M. A. Bari, S. Ali, S. Goumri-Said and M. B. Kanoun, *Nanoscale Adv.*, 2022, **4**, 3996–4008.

421 Y. Pan and M. Wen, *Int. J. Hydrogen Energy*, 2018, **43**, 22055–22063.

422 P. Ganguly, S. Mathew, L. Clarizia, A. Akande, S. Hinder, A. Breen and S. C. Pillai, *Appl. Catal., B*, 2019, **253**, 401–418.

423 Tian and Liu, *J. Phys. Chem. B*, 2006, **110**, 17866–17871.

424 S. Karvinen, P. Hirva and T. A. Pakkanen, *J. Mol. Struct.: THEOCHEM*, 2003, **626**, 271–277.

425 L. Yang, P. Gao, J. Lu, W. Guo, Z. Zhuang, Q. Wang, W. Li and Z. Feng, *RSC Adv.*, 2020, **10**, 20654–20664.

426 P. Zhuang, H. Yue, H. Dong and X. Zhou, *New J. Chem.*, 2020, **44**, 5428–5437.

427 O. Allam, M. Maghsoodi, S. S. Jang and S. D. Snow, *ACS Appl. Mater. Interfaces*, 2024, **16**, 36215–36223.

428 S. D. Dabhi and P. K. Jha, *Phys. E*, 2017, **93**, 332–338.

429 C. A. Celaya, C. Delesma, P. Valadés-Pelayo, O. A. Jaramillo-Quintero, C. O. Castillo-Araiza, L. Ramos, P. Sebastian and J. Muñiz, *Fuel*, 2020, **271**, 117616.

430 F. Nasehnia, S. M. Lima, M. Seifi and E. Mehran, *Comput. Mater. Sci.*, 2016, **114**, 112–120.

431 P. N. Gillespie and N. Martsinovich, *ACS Appl. Mater. Interfaces*, 2019, **11**, 31909–31922.

432 I. J. Mbonu, E. E. Ekereke, T. E. Gber, C. Iyen, I. Hossain, G. O. Egah, E. C. Agwamba, A. S. Adeyinka and H. Louis, *Chem. Phys. Impact*, 2024, **8**, 100439.

433 P. Okoye and B. Hameed, *Renewable Sustainable Energy Rev.*, 2016, **53**, 558–574.

434 C. Zhang, K. Yu, Y. Feng, Y. Chang, T. Yang, Y. Xuan, D. Lei, L. Lou and S. Liu, *Appl. Catal., B*, 2017, **210**, 77–87.

435 N. Miranda-García, S. Suárez, M. I. Maldonado, S. Malato and B. Sánchez, *Catal. Today*, 2014, **230**, 27–34.

436 A. V. Karim, S. Krishnan and A. Shriwastav, *J. Indian Chem. Soc.*, 2022, **99**, 100480.

437 M. Hao, M. Qiu, H. Yang, B. Hu and X. Wang, *Sci. Total Environ.*, 2021, **760**, 143333.

438 W. Kongsuebchart, P. Praserthdam, J. Panpranot, A. Sirisuk, P. Supphasrirongjaroen and C. Satayaprasert, *J. Cryst. Growth*, 2006, **297**, 234–238.

439 S. Thakur, A. Badoni, Samriti, P. Sharma, A. Ojha, H. C. Swart, A. Y. Kuznetsov and J. Prakash, *Langmuir*, 2024, **40**(35), 18486–18502.

440 Samriti, K. Shukla, R. Gupta, R. K. Gupta and J. Prakash, *Environ. Sci. Pollut. Res.*, 2023, **30**, 34054–34068.

441 M. Akrami, S. Danesh and M. Eftekhari, *J. Inorg. Organomet. Polym. Mater.*, 2019, **29**, 1785–1797.

442 F. Shoushtarian, M. Moghaddam and E. Kowsari, *J. Mol. Liq.*, 2020, **312**, 113386.

443 A. Khan, A. Sudhaik, P. Raizada, A. Khan, M. A. Rub, N. Azum, M. Alotaibi, P. Singh and A. Asiri, *Catal. Commun.*, 2023, **179**, 106685.

444 C. L. Fausey, I. Zucker, E. Shaulsky, J. B. Zimmerman and M. Elimelech, *Chem. Eng. J.*, 2019, **375**, 122040.

445 J. Corredor, E. Perez-Peña, M. J. Rivero and I. Ortiz, *Membranes*, 2020, **10**, 218.

446 J. D. Bersch, I. Flores-Colen, A. B. Masuero and D. Dal Molin, *Buildings*, 2023, **13**, 186.

447 B. S. Ramadan, Y. G. Wibowo, D. Anwar and A. T. Maryani, *Global NEST J.*, 2024, **26**(7), 06216.

448 M. Hassan, *Construction Research Congress 2009: Building a Sustainable Future*, 2009, pp. 836–845.

449 H. Babaizadeh and M. Hassan, *Constr. Build. Mater.*, 2013, **40**, 314–321.

450 R. Hischier, B. Nowack, F. Gottschalk, I. Hincapie, M. Steinfeldt and C. Som, *J. Nanopart. Res.*, 2015, **17**, 1–13.

451 M. Pini, E. I. Cedillo González, P. Neri, C. Siligardi and A. M. Ferrari, *Coatings*, 2017, **7**, 8.

452 S. Fernandes, J. C. Esteves da Silva and L. Pinto da Silva, *Materials*, 2020, **13**, 1487.

453 M. d. P. Rodríguez-Rojas, V. Bustos-Terrones, M. Y. Díaz-Cárdenas, E. Vázquez-Vélez and H. Martínez, *Sustainability*, 2024, **16**, 7751.

454 L. Serrano-Lujan, S. Víctor-Román, C. Toledo, O. Sanahuja-Parejo, A. E. Mansour, J. Abad, A. Amassian, A. M. Benito, W. K. Maser and A. Urbina, *SN Appl. Sci.*, 2019, **1**, 179.

455 J. F. Pesqueira, M. F. R. Pereira and A. M. Silva, *J. Cleaner Prod.*, 2024, **444**, 140845.

456 M. El-Kady, I. Ansari, C. Arora, N. Rai, S. Soni, D. K. Verma, P. Singh and A. Mahmoud, *J. Mol. Liq.*, 2023, **370**, 121046.

This journal is © The Royal Society of Chemistry 2025

Catal. Sci. Technol., 2025, **15**, 1702–1770 | **1769**

457 A. Umapathi, M. Kumawat and H. Daima, *Environ. Chem. Lett.*, 2022, **20**, 445–468.

458 H. K. Daima, S. L. Kothari and B. S. Kumar, *Nanotoxicology: toxicity evaluation of nanomedicine applications*, CRC Press, 2021.

459 S. Mitragotri, D. G. Anderson, X. Chen, E. K. Chow, D. Ho, A. V. Kabanov, J. M. Karp, K. Kataoka, C. A. Mirkin and S. Petrosko, *ACS Nano*, 2015, **9**, 6644–6654.

460 S. C. Sahu and A. W. Hayes, *Toxicol. Res. Appl.*, 2017, **1**, 2397847317726352.

461 M. Ali, *Adv. Colloid Interface Sci.*, 2023, **314**, 102881.

462 S. Attarilar, J. Yang, M. Ebrahimi, Q. Wang, J. Liu, Y. Tang and J. Yang, *Front. Bioeng. Biotechnol.*, 2020, **8**, 822.

463 S. Bettini, E. Boutet-Robinet, C. Cartier, C. Coméra, E. Gaultier, J. Dupuy, N. Naud, S. Taché, P. Grysan and S. Reguer, *Sci. Rep.*, 2017, **7**, 40373.

464 F. Gottschalk, C. Lassen, J. Kjoelholt, F. Christensen and B. Nowack, *Int. J. Environ. Res. Public Health*, 2015, **12**, 5581–5602.

465 K. L. Garner, S. Suh and A. Keller, *Environ. Sci. Technol.*, 2017, **51**, 5541–5551.

466 W. Peijnenburg, A. Praetorius, J. Scott-Fordsmand and G. Cornelis, *Environ. Pollut.*, 2016, **218**, 1365–1369.

467 M. Skocaj, M. Filipic, J. Petkovic and S. Novak, *Radiol. Oncol.*, 2011, **45**, 227–247.

468 S. Zia, A. Islam Aqib, A. Muneer, M. Fatima, K. Atta, T. Kausar, C. Zaheer, I. Ahmad, M. Saeed and A. Shafique, *Front. Neurol.*, 2023, **17**, 1127460.

469 B. Song, J. Liu, X. Feng, L. Wei and L. Shao, *Nanoscale Res. Lett.*, 2015, **10**, 1–17.

470 C. Tay, W. Fang, M. I. Setyawati, S. Chia, K. Tan, C. Hong and D. Leong, *ACS Appl. Mater. Interfaces*, 2014, **6**, 6248–6256.

471 W. Saidani, B. Sellami, A. Khazri, A. Mezni, M. Dellali, O. Joubert, D. Sheehan and H. Beyrem, *Aquat. Toxicol.*, 2019, **208**, 71–79.

472 X. Huang, Z. Liu, Z. Xie, S. Dupont, W. Huang, F. Wu, H. Kong, L. Liu, Y. Sui and D. Lin, *Mar. Environ. Res.*, 2018, **137**, 49–59.

473 T. Tang, Z. Zhang and X. Zhu, *Int. J. Environ. Res. Public Health*, 2019, **16**, 523.

474 L. Gnatyshyna, H. Falfushynska, O. Horyn, V. Khoma, V. Martynyuk, O. Mishchuk, N. Mishchuk and O. Stoliar, *Ecotoxicology*, 2019, **28**, 923–937.

475 J. Gurr, A. S. Wang, C. Chen and K. Jan, *Toxicology*, 2005, **213**, 66–73.

476 J. Petković, B. Žegura, M. Stevanović, N. Drnovšek, D. Uskoković, S. Novak and M. Filipič, *Nanotoxicology*, 2011, **5**, 341–353.

477 X. Guan, W. Shi, S. Zha, J. Rong, W. Su and G. Liu, *Aquat. Toxicol.*, 2018, **200**, 241–246.

478 B. Jovanović, E. M. Whitley, K. Kimura, A. Crumpton and D. Palić, *Environ. Pollut.*, 2015, **203**, 153–164.

479 B. Jovanović, L. Anastasova, E. W. Rowe, Y. Zhang, A. R. Clapp and D. Palić, *Ecotoxicol. Environ. Saf.*, 2011, **74**, 675–683.

480 M. Hu, D. Lin, Y. Shang, Y. Hu, W. Lu, X. Huang, K. Ning, Y. Chen and Y. Wang, *Sci. Rep.*, 2017, 7(1), 40015.

481 Z. Luo, Z. Li, Z. Xie, I. M. Sokolova, L. Song, W. J. Peijnenburg, M. Hu and Y. Wang, *Small*, 2020, **16**, 2002019.

482 O. Y. Costa, J. M. Raaijmakers and E. Kuramae, *Front. Microbiol.*, 2018, **9**, 1636.

483 V. C. Sanchez, A. Jachak, R. H. Hurt and A. Kane, *Chem. Res. Toxicol.*, 2012, **25**, 15–34.

484 A. Ojha and P. Thareja, *Appl. Surf. Sci.*, 2018, **435**, 786–798.

485 A. Ojha, H. Ibrahim, N. Alyabyeva, R. Lazzari, M. Goldmann and P. Thareja, *Synth. Met.*, 2020, **269**, 116494.

486 M. Simsikova, *Nanomed. Res. J.*, 2017, **5**, 00109.

487 F. Emadi, A. Amini, A. Gholami and Y. Ghasemi, *Sci. Rep.*, 2017, **7**, 42258.

488 O. N. Ruiz, K. S. Fernando, B. Wang, N. A. Brown, P. G. Luo, N. D. McNamara, M. Vangsness, Y. Sun and C. Bunker, *ACS Nano*, 2011, **5**, 8100–8107.

489 G. Chen, D. Pang, S. Hwang, H. Tuan and Y. Hu, *Biomaterials*, 2012, **33**, 418–427.

490 H. H. Yoon, S. H. Bhang, T. Kim, T. Yu, T. Hyeon and B. Kim, *Adv. Funct. Mater.*, 2014, **24**, 6455–6464.

491 A. Rhazouani, H. Gamrani, M. El Achaby, K. Aziz, L. Gebrati, M. S. Uddin and F. Aziz, *BioMed Res. Int.*, 2021, **2021**, 5518999.

492 Y. Wang, J. Liu, L. Liu and D. Sun, *Nanoscale Res. Lett.*, 2011, **6**, 1–8.

493 M. Bangeppagari, S. H. Park, R. Kundapur and S. Lee, *Sci. Total Environ.*, 2019, **673**, 810–820.

494 J. P. Souza, F. P. Venturini, F. Santos and V. Zucolotto, *Chemosphere*, 2018, **190**, 218–224.

495 Y. Chang, S.-T. Yang, J.-H. Liu, E. Dong, Y. Wang, A. Cao, Y. Liu and H. Wang, *Toxicol. Lett.*, 2011, **200**, 201–210.

496 H. Yue, W. Wei, Z. Yue, B. Wang, N. Luo, Y. Gao, D. Ma, G. Ma and Z. Su, *Biomaterials*, 2012, **33**, 4013–4021.

497 S. Gurunathan, M. Kang, M. Jeyaraj and J. Kim, *Nanomaterials*, 2019, **9**, 139.

498 A. Wang, K. Pu, B. Dong, Y. Liu, L. Zhang, Z. Zhang, W. Duan and Y. Zhu, *J. Appl. Toxicol.*, 2013, **33**, 1156–1164.

499 M. Pelin, L. Fusco, V. León, C. Martín, A. Criado, S. Sosa, E. Vázquez, A. Tubaro and M. Prato, *Sci. Rep.*, 2017, **7**, 40572.

500 Z. Yang, Y. Pan, T. Chen, L. Li, W. Zou, D. Liu, D. Xue, X. Wang and G. Lin, *Front. Pharmacol.*, 2020, **11**, 1206.

501 Z. Guo, J. Zuo, J. Feng, J. Li, S. Zhang and K. Ma, *Mar. Biotechnol.*, 2023, **25**, 45–56.

502 J. Prakash, M. Venkatesan, G. Bharath, S. Anwer, P. Veluswamy, D. Prema, K. Venkataprasanna and G. Venkatasubbu, *Appl. Surf. Sci.*, 2019, **481**, 1360–1369.

503 H. Al-Kandari, N. Younes, O. Al-Jamal, Z. Zakaria, H. Najjar, F. Alserr, G. Pintus, M. Al-Asmakh, A. M. Abdullah and G. Nasrallah, *Nanomaterials*, 2019, **9**, 488.

1770 | *Catal. Sci. Technol.*, 2025, **15**, 1702–1770

This journal is © The Royal Society of Chemistry 2025